

Effect of polymer matrix structure on mechanical properties of electrospun nanofibers

Research proposal for PhD degree

Submitted by
Israel Greenfeld

November 2009

Supervisor
Prof. Eyal Zussman

Department of Mechanical Engineering,
Technion–Israel Institute of Technology, Haifa 32000, Israel
greenis@tx.technion.ac.il

Table of Contents

Abstract	1
1. Introduction	2
2. Background and literature review	4
2.1 Polymer physics – networks and dynamics	4
2.2 Electrospinning	7
2.3 Mechanical properties of solid polymers	14
2.4 Mechanical properties of nanofibers	19
2.5 Theoretical explanations for size-dependent elasticity	23
3. Motivation and research goals	26
3.1 Information gaps	26
3.2 Motivation	28
3.3 Research goal and objectives	28
4. Methodology and research program	30
4.1 Theoretical modeling and simulation	30
4.2 Nanofibers fabrication using electrospinning	32
4.3 Characterization of mechanical properties and morphology	34
4.4 Time table	35
5. Preliminary results	36
5.1 Scaling law correlating elastic moduli to fiber radius and chain length	36
5.2 Chain conformation between two boundaries	40
5.3 Random walk simulation tool	45
5.4 Single chain stretching under electrospinning shear flow	48
5.5 Network stretching under electrospinning shear flow	59
5.6 Transversal contraction due to electrospinning stretching	64
5.7 Preliminary conclusions	69
Appendix A. Polymer physics – single chain static conformations	70
Notations	77
References	82

List of Figures

Figure 2-1: Crossover between dilute and semi-dilute solutions.....	4
Figure 2-2: Four roll mill used to create extensional flows.....	6
Figure 2-3: Free energy versus relative elongation.....	6
Figure 2-4: A schematic of the electrospinning process.....	8
Figure 2-5: Range of structures that can be produced by electrospinning.....	9
Figure 2-6: Zero shear rate viscosity η_0 versus relative concentration.....	10
Figure 2-7: Variation of fiber diameter versus relative concentration.....	10
Figure 2-8: Optical microscopy measurement of the jet profile and velocity.....	11
Figure 2-9: Optical microscopy measurement of the jet profile and velocity.....	11
Figure 2-10: Simulation of solvent evaporation in nanofibers.....	13
Figure 2-11: Electrospun tubular core-shell nanofibers.....	13
Figure 2-12: Classes of polymer matrix structure.....	15
Figure 2-13: Schematic illustrations of polymer crystalline structure.....	15
Figure 2-14: Fully extended chain model.....	18
Figure 2-15: Representative stress–strain curves for electrospun Cl-PP.....	19
Figure 2-16: Representative stress–strain curves for PVA electrospun membranes... ..	19
Figure 2-17: Schematic of the three-point bending method.....	20
Figure 2-18: Young’s modulus of PS for fibers of different diameters.....	20
Figure 2-19: Schematic of the SMFM method.....	21
Figure 2-20: Relative tensile and shear moduli.....	21
Figure 2-21: The string pendulum test.....	21
Figure 2-22: Young’s modulus E of nylon 66 versus nanofiber diameter.....	21
Figure 2-23: X-rays diffraction tests of electrospun Nylon 66 nanofibers.....	22
Figure 2-24: Three-point bending tests of polypyrrole nanotubes.....	22
Figure 2-25: Three-point bending tests of Ag nanowires.....	22
Figure 2-26: Model of the molecular chain orientation.....	24
Figure 2-27: Arrangement of crystallites and oriented amorphous matrix.....	24
Figure 3-1: Diagram of research parameters.....	26
Figure 5-1: Scales in nanofibers.....	36
Figure 5-2: Arrangement of coils of gyration radius R_g within the cross-section.....	37
Figure 5-3: Scaling of relative delta moduli to fiber radius.....	39
Figure 5-4: Distribution of one-dimensional chain end position x	40
Figure 5-5: Distribution of relative chain end position x/R_g	41
Figure 5-6: First ten central statistical moments of the end-to-end chain lengths.....	42

Figure 5-7: Distribution of chain monomers (or chain elements) mass density	43
Figure 5-8: Bivariate distribution of the chain monomers mass density	44
Figure 5-9: Random walk procedure	45
Figure 5-10: Single axis random walk simulation of single ideal chains	46
Figure 5-11: Random walk simulation sample of $I = 1,000$ chains	46
Figure 5-12: Distribution of chain relative end position.....	46
Figure 5-13: Forces acting on monomers	47
Figure 5-14: One-dimensional random walk	49
Figure 5-15: Global and local coordinate systems in the electrospinning jet	50
Figure 5-16: Illustration of the effect of the jet global coordinate.....	52
Figure 5-17: Probability to step downstream.....	53
Figure 5-18: Two RW runs of a single chain in a flow field	53
Figure 5-19: RW simulation of $I = 20,000$ chains	54
Figure 5-20: RW simulation of $I = 20,000$ chains	55
Figure 5-21: Phase transition of chain lengths (coil-stretch transition).....	56
Figure 5-22: Mean-square chain values versus jet radius	58
Figure 5-23: Polymer network immersed in a solution in a shear flow	59
Figure 5-24: Procedure for RW simulation of a polymer network in a shear flow.	61
Figure 5-25: RW simulation of polymer network stretching in shear flow	63
Figure 5-26: Phase transition of subchain length (coil-stretch transition).....	63
Figure 5-27: RW simulation of polymer network stretching in shear flow	64
Figure 5-28: Radial contraction ratio CR due to axial stretching	66
Figure 5-29: Probability P_r to step radially towards the chain center.....	67
Figure 5-30: Approximate probability density function $P(\varphi_o)$ versus the orientation.	68
Figure 5-31: Mean orientation angle φ_o versus the inverse velocity gradient term	68
Figure A-1: Examples of synthetic polymers and their repeating units.....	70
Figure A-2: Bond flexibility due to variation in torsion angles.....	71
Figure A-3: Computer simulation of a polymer chain.....	72
Figure A-4: Computer simulation of coil conformation of a single ideal chain	73
Figure A-5: Distribution of three-dimensional relative end-to-end distances	76

List of Tables

Table 2-1: Typical materials and process parameters used in electrospinning.....	8
Table 4-1: Research program time table.	35

Abstract

Electrospinning is a method for the fabrication of polymer fibers of nanoscale diameters ranging from 50 to 1000 nanometers. These nanofibers exhibit unique mechanical properties, which may be valuable for future designs and applications. Specifically, below a certain crossover diameter dependent on the polymer molecular weight, the nanofiber elastic moduli begin to rise sharply. Various explanations for this phenomenon have been suggested, but further research is required to understand the physical mechanisms behind it. The proposed research seeks to explain the effect of electrospinning on the polymer matrix nanoscale structure, and to reveal the mechanism by which this nanostructure impacts the mechanical properties. This research proposal reviews and discusses the relevant scientific background and current literature in the fields of polymer physics, polymer mechanical properties, electrospinning, and nanofibers. Additional material presented includes the results of the preliminary study carried out by the author as part of this research, including analysis of available experimental data on the mechanical properties of nanofibers; modeling and simulation of the effect of nanofiber boundary (free surface) on its nanostructure; and simulation of the electrospinning stretching effects. The research proposal defines the research motivation, goals and program, and sets out the methodology and tools to be used in the research, combining theoretical, simulation, and experimental work.

1. Introduction

Structures of nanoscale size, one millionth of a millimeter (10^{-9} m, or 1 nm), reveal unique mechanical and electrical properties, since their size is of the same order of magnitude as the size of the atoms and molecules composing them. Polymers exhibit such behavior even on higher scales due to their large molecular size and flexible conformation. Polymers are very long molecules (macromolecules or chains), whose backbone is constructed from many successive carbon-to-carbon chemical bonds. When the chains are straight and aligned to each other, the polymer can theoretically achieve strength and rigidity two orders of magnitude higher than those found in ordinary commercial plastic materials, thereby indicating the ultimate potential of polymers as engineering materials. However, due to flexibility in bond rotation these macromolecules tend to coil in random conformations, with a resultant reduction in their strength and rigidity. Above a certain critical concentration, polymer chains in a solution create an entangled network, which sometimes includes bonded cross-links, affecting their structural properties.

One of the more accessible techniques used to create nanostructures is electrospinning, whereby a jet of polymer solution is drawn from a capillary and stretched by the force of a strong electrical field, producing very thin fibers – nanofibers – of diameters ranging from 50 nm to 1000 nm (1 μ m). This method has attracted considerable interest over the past fifteen years, both within the academic community and among those engaged in commercial exploitation. It found many new applications in the fields of life sciences, tissue engineering, filter media, cosmetics, military clothing, nanosensors and more.

Recent experiments at the Technion - Haifa and Stony Brook University – NY (SUNY) found that the strength and elastic properties of electrospun nanofibers are highly dependent on their diameter and polymer chain size (i.e. its molecular weight). The smaller the nanofiber diameter (especially below a certain crossover radius), and the larger the polymer chain size, the more rigid and strong the nanofiber becomes. It has been common knowledge for many years that polymer fibers of microscale size (10^{-6} m) improve their strength and elasticity when post-processed by mechanical drawing or rolling. The phenomenon is similar – in both the nano- and micro-process the random coils of the polymer macromolecules are stretched along the fiber's longitudinal axis, attaining a higher degree of alignment, thereby approaching their ultimate mechanical properties. However, in nanofibers, additional factors are

involved due to macromolecular structures that are of the same order of magnitude as the fiber's diameter.

This field of research is multidisciplinary, as is usually the case in nanoscience, encompassing polymer physics, polymer mechanical properties, electrospinning, and nanofibers. The field of polymer physics studies macromolecule conformations and properties, in both the solution state and solid state, extensively applying scaling concepts and statistical methods. The mechanical properties of polymers is a field that extends from nanoscale physics to the macroscale investigation of bulk properties. Electrospinning is emerging as a research and engineering field in its own right, involving basic research into the complex static and dynamic phenomena, and the development of measurement and fabrication techniques. Specifically, the topic of nanofibers' mechanical and other properties has been extensively researched recently. The scientific background and published results are presented in Section 2.

The physical mechanisms driving the increase in the elastic modulus of nanofibers require further research and deeper understanding. The goal of the proposed research is to explain the effect of electrospinning on the polymer matrix nanoscale structure, and to reveal the mechanism by which this nanostructure impacts the mechanical properties. It is anticipated that a better understanding of this behavior will be valuable for future designs and the applications of nanofibers. The research motivation and goals are presented in Section 3, and the planned theoretical and experimental methodology is described in Section 4.

The research topics have been investigated by the author in a preliminary study presented in this proposal. The available experimental data from the Technion and SUNY were analyzed in search of a universal scaling law correlating the nanofiber elastic modulus to the fiber diameter, polymer molecular weight and nanostructural orientation. The nanofiber boundary effect on chain conformation was modeled by solving the diffusion equation. A one-dimensional random walk simulation tool was developed and validated, allowing deeper exploration of the statistical behavior and average conformation of the macromolecules. The simulation tool was applied to the investigation of chain stretching under the extensional forces of electrospinning, and the results provided interesting insights on chain conformation and orientation. The preliminary results and conclusions are described in Section 5.

The proposed research will continue and expand the analysis and modeling of the structural effects caused by electrospinning and their impact on nanofiber elasticity, and will conduct experiments to validate them.

2. Background and literature review

This section reviews the literature relevant to this research, starting from the scientific foundation on polymer physics, through description of the electrospinning method for fabricating nanofibers, and finally a review of the recent publications on the unique mechanical properties of polymer nanofibers.

2.1 Polymer physics – networks and dynamics

The basic concepts of polymer physics are described in Appendix A, including chain flexibility, Kuhn segment, scale invariance, ideal chains, real chains, scaling laws, and chain lengths distribution, concerning the static conformations of single chains. The following paragraph expands on topics that are specifically relevant to this research.

Of specific importance to electrospinning is the distinction between the types of **polymer solutions**, as depicted in Figure 2-1. In a dilute solution, the chains do not overlap, while in a semi-dilute solution they overlap and create a viscoelastic¹ mesh, a network that is essential for fabrication of continuous fibers by electrospinning. See more on this issue in Section 2.2.

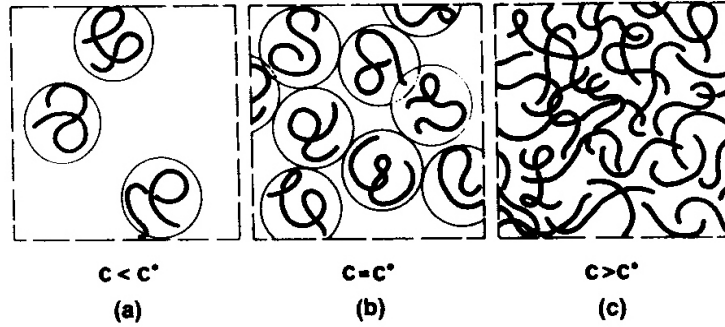


Figure 2-1: Crossover between dilute and semi-dilute solutions: (a) dilute, (b) onset of overlap (crossover concentration), and (c) semi-dilute [1].

The crossover concentration c^* and the crossover volume fraction ϕ^* may be estimated as the monomers concentration inside a single coil of radius R_c (equal to R_0 for ideal chains or R_F for real chains) [1]²

$$c^* \cong N / R_c^3 \cong \frac{N^{1-3\nu}}{a^3} \quad \text{and} \quad \phi^* = c^* / \rho \cong N^{1-3\nu}, \quad (2.1)$$

¹ A viscoelastic polymer solution exhibits both elastic behavior (resistance to static strain) and viscous behavior (resistance to strain rate) under deformation, and therefore its strain is time dependent.

² de Gennes' equation was generalized with the exponent ν .

where N is the number of monomers³ (or chain elements), a the monomer size, ν the Flory scaling exponent, and $\rho \equiv a^{-3}$ the polymer density. The exponent ν is 1/2 for ideal chains and 3/5 for real chains in good solvent. The average mesh size ξ of the network in a semi-dilute solution, or the distance between two topological links, is dependent on the coil radius R_c (mean-square end-to-end distance from Equation (A.8)) and the relative volume fraction ϕ/ϕ^*

$$\xi = R_c \left(\frac{\phi}{\phi^*} \right)^m \cong a N^\nu \left(\frac{\phi}{N^{1-3\nu}} \right)^m \cong a \phi^{\nu/(1-3\nu)} \quad \text{or} \quad (2.2)$$

$$\xi = R_c \left(\frac{\phi}{\phi^*} \right)^{\nu/(1-3\nu)} = R_c \left(\frac{c}{c^*} \right)^{\nu/(1-3\nu)},$$

where the exponent m is chosen so that R_c and ϕ^* are independent⁴ (their powers of N cancel); m has a value of -1 for ideal chains and -3/4 for real chains.

The dynamics of polymer chains in a solvent or a melt is also relevant to electrospinning. Its behavior and analysis are quite complex, especially for highly concentrated solutions. A single chain in a solvent returns to its equilibrium state within a **relaxation** time τ estimated by

$$\tau \cong \frac{\eta_s R_c^3}{k_B T}, \quad (2.3)$$

where η_s is the solution viscosity, R_c is either R_0 or R_F for ideal or real chains respectively, k_B the Boltzmann constant, and T the temperature. For $R_c \sim 50$ nm and $\eta_s \sim 1$ poise (0.1 Pa·s), τ is of order 10^{-5} s [1]. The situation is, however, more complex for a polymer network, where the individual chain cannot relax freely, but rather reptates (crawls) slowly along a corridor formed by its neighboring chains. For real chains the reptation time is of order $\sim N^3$, compared to the relaxation time order of $\sim N^{9/5}$, and it depends also on the concentration c . In the extreme case of a melt, the reptation time for a long chain of $N = 10^4$ is ~ 10 s [1].

De Gennes [1-2] describes a model for deformation of a single chain in dilute solution (good solvent) under a strong **extensional flow** with constant velocity gradient s . Such conditions were created with the four-roll mill experiment by

³ N is also referred to as the degree of polymerization of a linear chain.

⁴ Above the crossover concentration the mesh size ξ does not depend on N but only on concentration, because the chains are much longer than the mesh size.

Crowley et al. [3] illustrated in Figure 2-2, where chain elongation was detected by optical birefringence. This problem was also investigated by Feng et al., using numerical simulations of the flow of dilute polymer solutions [4-5].

For a given elongation r , the free energy F_{tot} of the chain consists of the coil elastic energy from Equation (2.13), the friction (hydrodynamic) energy $\sim \eta_s s r^3$, and the full-stretch elastic energy (at very high elongation). Using relative elongation $\lambda \equiv r/R_F$,

$$F_{tot} = F_{elastic(coil)} - F_{friction} + F_{elastic(full-stretch)}$$

$$\frac{F_{tot}}{k_B T} = \lambda^{5/2} - s\tau\lambda^3 + \frac{F(\lambda)_{elastic(full-stretch)}}{k_B T}, \quad (2.4)$$

where τ is used from Equation (2.3). When increasing the gradient s above $1/\tau$, the friction energy dominates, until the relative elongation λ approaches full stretching thereby increasing the elastic energy sharply.

The behavior of the chains under such conditions demonstrates two distinct energy equilibrium states, presented in Figure 2-3: when the gradient is smaller than a critical value s_c , the chain is slightly stretched but remains in a conformation resembling a Gaussian coil; above the critical gradient, the chain goes to an almost fully stretched state; a phase transition (also called coil-stretch transition) occurs at the critical gradient, with two energy minima separated by a huge energy barrier, corresponding to the coil shape and the stretched shape.

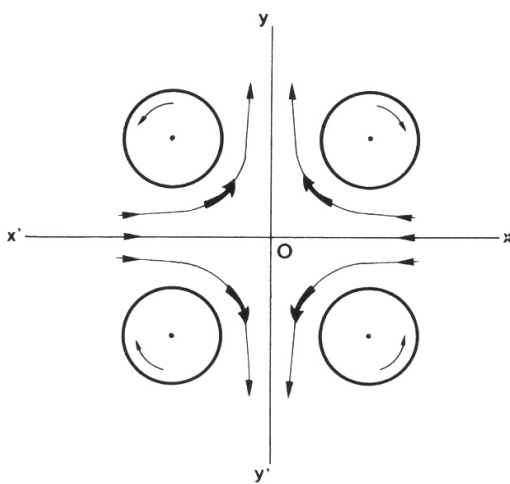


Figure 2-2: Four roll mill used to create extensional flows with constant velocity gradient along the axis of exit y [1].

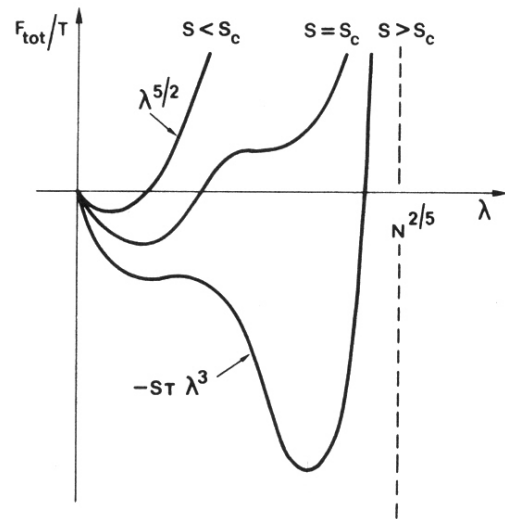


Figure 2-3: Free energy versus relative elongation $\lambda \equiv r/R_F$ for a single polymer coil in a longitudinal extensional flow [1].

It should be noted that while stretching is effective, there is a balance between the hydrodynamic stretching force and the elastic contraction force of an entropic chain; there is no relaxation whatsoever, and the relaxation time τ in the expression $s\tau$ is only used for scaling convenience.

This analysis implies that substantial chain stretching can occur with high strain-rate extensional flows of concentrated polymer solutions (i.e. network), typical to electrospinning. Moreover, as shown in Section 2.2, during electrospinning the flow velocity gradient s is not constant, but rather rises linearly along the solution jet.

2.2 Electrospinning

Electrospinning, or electrostatic spinning, is a convenient and industrially-scalable technique for fabricating polymer nanofibers, at diameters ranging typically from 50 to 1000 nm. Due to their nanoscale size and unique mechanical and electrical properties, nanofibers are applied in diverse fields such as life science, tissue engineering, filter media, cosmetics, military clothing, and nanosensors [6]. Though discovered and patented by J. F. Cooley and W. J. Morton a long time ago [US patent # 692631, 1902], and further researched and developed by G. Taylor [7] and others during the 20th century, the process gained considerable focus in the last 10-15 years due to the nanotechnology revolution, generating a surge of publications and patents on the subject. Several text books and articles by Andradý [8], Stanger [9], Huang [6], and Gogotsi [10] provide good overview of the process, the science behind it, the control of its parameters, and its applications.

The **process** consists of (Figure 2-4) a viscous polymer solution, pumped into a syringe and drawn into a capillary needle, subjected to an electrical field of typically 1-2 kV/cm that draws the solution out of the needle into a cone-shaped drop (Taylor cone), and sprays it as a jet towards the ground plate (collector). The solvent evaporates rapidly and the nanofiber is almost dry when reaching the ground plate, where it is collected by various techniques, creating a mat with ordered or arbitrarily-oriented nanofibers. Examples of typical materials and process parameters are shown in Table 2-1.

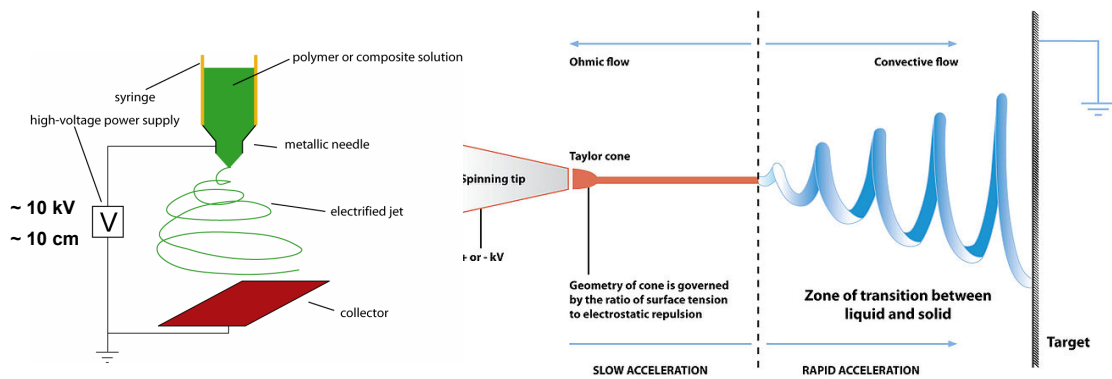


Figure 2-4: A schematic of the electrospinning process, showing the basic equipment and the creation of the jet [11-12].

Table 2-1: Typical materials and process parameters used in electrospinning. Based on [9].

Parameter	Polyethylene oxide (PEO)	Polystyrene (PS)	Polypropylene (PP)
Solvents	Water, Acetone Chloroform, Ethanol, N,N-Dimethyl-formamide Acetic acid Water, Methanol Water, Ethanol	DMF, Toluene Carbon Disulfide (CS ₂) Chloroform, THF, Methylethylketone Acetic acid	Melt at 285°C
Concentration, %	10	20	-
Molecular weight, g/mol	400,000	200,000 – 300,000	200,000
Voltage, kV	10 – 20	30	20
Distance, cm	15	15	4
Electric field, kV/cm	0.5 – 1	1	5

Some of the experimental tools and methods used for characterization of electrospun nanofibers are: in-process imaging of the jet (optical, laser or X-rays) to measure its shape and velocity; scanning electron microscope (SEM) and transmission electron microscope (TEM) electron microscopy imaging to measure the nanofiber morphology; scattering techniques, such as wide angle X-ray scattering (WAXS), small angle X-ray scattering (SAXS), and small angle neutron scattering (SANS), to measure the degree of crystallinity and orientation; atomic force microscopy (AFM) to measure shape and size and to perform tensile and bending tests; and dynamic mechanical thermal analysis (DMTA) tensile testing equipment to measure the elastic moduli, ultimate strength, viscoelastic properties, and glass transition temperature.

Tests can be performed on single nanofibers, a difficult task requiring micro-manipulation, or on dense mats of collected nanofibers.

The quality of the electrospun nanofiber strongly depends on the rheological and electrical properties of the polymer solution and on the process parameters (electrostatic field, flow rate, ambient conditions). Demir et al. [13] investigated the effects of electrical field, temperature, conductivity and viscosity of the solution on polyurethane electrospinning process, and the morphology and properties of the nanofibers obtained, and concluded that the solution viscosity, i.e. its concentration and temperature, is the dominant factor. Hsu [14] provides examples of morphologies that can be obtained by electrospinning (Figure 2-5), demonstrating how beads, and fibers with uneven diameter, can be formed at low polymer molecular weights and low solution concentrations.

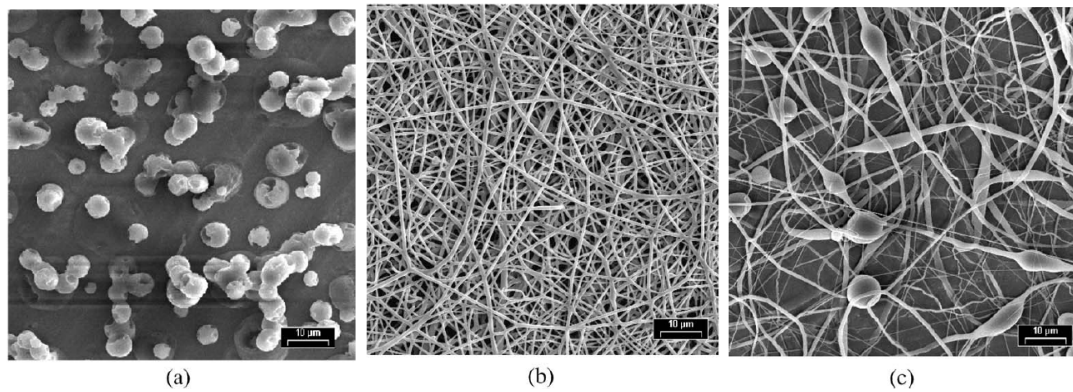


Figure 2-5: Range of structures that can be produced by electrospinning of poly(ϵ -caprolactone): (a) beads, (b) fibers, and (c) beads on string [14].

A key objective in fabricating nanofibers is to achieve a desired fiber **diameter** by proper adjustment of the process parameters. Rutledge et al. [15] developed an equation governing the nanofiber diameter d

$$d = \left[\gamma \epsilon \frac{Q_F^2}{I_E^2} \frac{2}{\pi(2 \ln \chi - 3)} \right]^{1/3}, \quad (2.5)$$

where γ is the surface tension, ϵ the dielectric constant, Q_F the volumetric flow rate, I_E the electrical current carried by the fiber, and χ the ratio of the initial jet length to the nozzle diameter.

Gupta et al. [16] observed that the dependence of the polymer solution viscosity on the solution relative concentration c/c^* exhibits three distinct concentration regions identified by Colby et al. [17] as dilute ($c/c^* < 1$), semidilute unentangled ($1 < c/c^* < 3$), and semidilute entangled ($c/c^* > 3$) (Figure 2-6), expanding the common

definitions of Figure 2-1. A semidilute entangled solution contains entangled polymer chains, ensuring the elastic behavior of the jet and continuous nanofibers. Conversely, in a semidilute unentangled solution, the polymer chains are not sufficiently entangled, resulting in beads rather than continuous nanofibers. Additionally, Gupta observed the dependence of the fiber diameter on concentration (Figure 2-7).

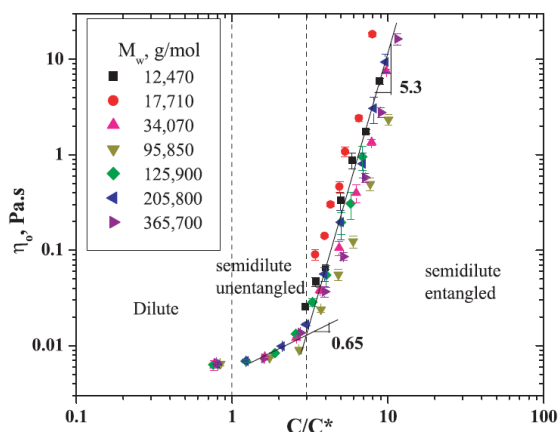


Figure 2-6: Zero shear rate viscosity η_0 versus relative concentration c/c^* , for different molecular weights M_w of polymethyl methacrylate (PMMA) [16].

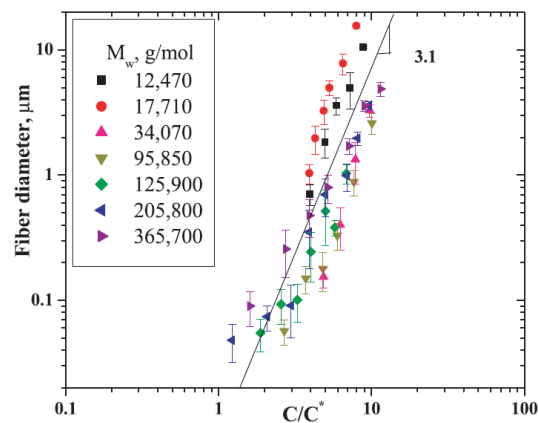


Figure 2-7: Variation of fiber diameter versus relative concentration c/c^* , for different molecular weights M_w of polymethyl methacrylate (PMMA) [16].

Based on these experiments, Gupta derived the following scaling relationships for the dependencies of the fiber diameter d on the relative concentration c/c^* and on the zero shear rate viscosity⁵ η_0

$$d \sim \left(\frac{c}{c^*}\right)^{3.1} \quad \text{and} \quad d \sim (\eta_0)^{0.72}, \quad (2.6)$$

in agreement with Demir et al. [13] who measured $d \sim c^3$, using a different type of polymer. These results suggest a universal scaling law that may be useful since the ratio c/c^* appears in many equations of polymer physics, such as Equation (2.2).

The jet undergoes substantial **stretching** during the electrospinning process. The jet velocity and diameter were measured as a function of the distance x along the jet by Han et al. [18] (Figure 2-8) and by Bellan et al. [19] (Figure 2-9), using in-process optical microscopy. The observed region started at the Taylor cone, and extended up to 5mm (Han) and 1.2 mm (Bellan), as shown on the attached photographs. The maximal measured jet velocity within the observed region was 0.8 m/s (Han) and 0.35 m/s (Bellan), while the maximal jet strain rate (velocity gradient) dv/dx can be derived from the graphs as 300 s^{-1} (Han) and 500 s^{-1} (Bellan),

⁵ Viscosity of a non-Newtonian liquid, taken at very low strain (shear) rate.

demonstrating a non-constant gradient. Han also evaluated the viscoelastic Rouse relaxation time to be in the range of 3 - 8 ms.

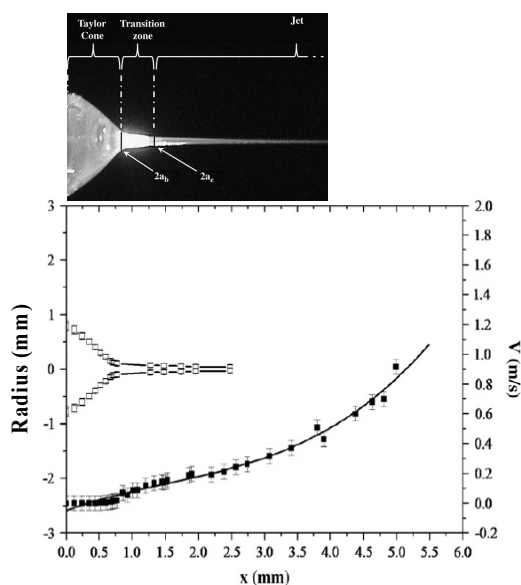


Figure 2-8: Optical microscopy measurement of the jet profile and velocity, versus the x position along the jet: polyethylene oxide (PEO), $M_w = 400,000$ g/mol, 6 wt% solution in water [18].

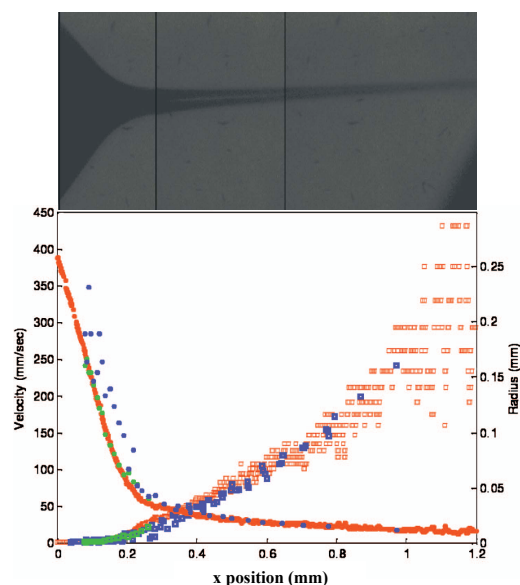


Figure 2-9: Optical microscopy measurement of the jet profile and velocity, versus the x position along the jet: polyethylene oxide, $M_w = 100,000$ g/mol, 20 wt% solution in water [19].

Reneker et al. [20-21] investigated also the region beyond the initial straight jet, using a polyethylene oxide aqueous solution, and found that electrical bending (whipping) instability (similar to Figure 2-4) causes the jet to form a sequence of smoothly curved loops, generating a considerable elongation of the fiber, with an average strain rate of 10^3 s^{-1} . The theoretical value of the strain rate was estimated as 10^5 s^{-1} , however, the measured value was much lower due to evaporation and solidification. With relaxation time for this polymer solution equaling 10^{-2} s , the scaling expression $s\tau$ from Equation (2.4) was estimated as 10^1 - 10^3 , much greater than 0.5, indicating that the polymer macromolecules were stretched significantly.

The jet hydrodynamic equations were solved by Reznik et al. [22] for Newtonian flow⁶, and the global longitudinal velocity V_x and radial velocity V_r were found as quadratic functions of the global position X along the jet and the radial position r (V_0 and X_0 are initial jet conditions)

⁶ This approach is an approximation since Newtonian flow assumes constant viscosity, while (according to Andradý) a polymer solution shows reduced viscosity (shear-thinning) at moderate shear rates, and may revert to Newtonian behavior at high shear rates.

$$V_x \approx V_0 \left(1 + \frac{X}{X_0} \right)^2 + \dots \quad (2.7)$$

$$V_r \approx -V_0 \left(1 + \frac{X}{X_0} \right) \frac{r}{X_0} + \dots,$$

exhibiting a non-constant velocity gradient, in agreement with the experiments by Han and Bellan presented above. The dots in Equation (2.7) represent terms that can be ignored, such as the variation (profile) of V_x across the fiber's cross-section. Volume conservation dictates that the jet radius r_j should have a hyperbolic shape (r_0 is an initial jet condition)

$$r_j = \frac{r_0}{1 + X/X_0}. \quad (2.8)$$

It is clear that the longitudinal velocity V_x and the radial velocity V_r cannot go to infinity and are therefore expected to saturate at some point. Similarly, the jet radius r_j cannot converge to zero and should saturate as well. Saturation can obviously occur at the onset of solidification. Thus, we shall need to introduce saturation effects into the models and simulations.

The nature of the parameters V_0 and r_0 is clear, being the jet velocity and radius at the jet starting point. The parameter X_0 has a different meaning – it designates the distance from the jet starting point back to a theoretical point where the jet velocity is zero, and it depends on the flow rate, electrical field, viscosity, and electrical conductivity [22]. The values of the initial parameters can be estimated from Han's and Bellan's measurements, by fitting Equation (2.7) to the jet velocity data and Equation (2.8) to the jet radius data. For Han's data we obtain: $V_0 = 1$ mm/s, $r_0 = 0.78$ mm, and $X_0 = 0.18$ mm. Similarly for Bellan's data: $V_0 = 0.6$ mm/s, $r_0 = 0.26$ mm, and $X_0 = 0.052$ mm. Substituting these parameters into Equation (2.7), the jet travel time through the region observed in these experiments, can be calculated by integration $t = \int dx/V_x$ as 170 ms (Han) and 80 ms (Bellan).

The substantial stretching of the polymer during electrospinning is subject to complex effects of solvent **evaporation**. Evaporation causes early solidification of the outer part of the fiber, lessening the stretching effect, followed by partial relaxation (i.e. reptation) in the inner part of the fiber that is still in solution state. The dynamics of this process is dependent upon the respective characteristic times of evaporation

and relaxation in a particular polymer solution, and on the opposite restraining effect of the polymer network. Since Equations (2.7) and (2.8) do not account for evaporation, their validity is limited to the initial jet phase.

Guenther et al. [23] analyzed and simulated the solvent evaporation process in nanofibers, and found (Figure 2-10) that above a critical evaporation rate solid skin layers are formed, while the fiber core is still in solution state, and the process is governed by the competition between solvent evaporation rate and its diffusion rate through the skin. Below the critical rate, evaporation is fairly uniform across the fiber cross-section. The process is accompanied by fiber shrinkage, and often, as a result of possible cavity in the core, by fiber buckling.

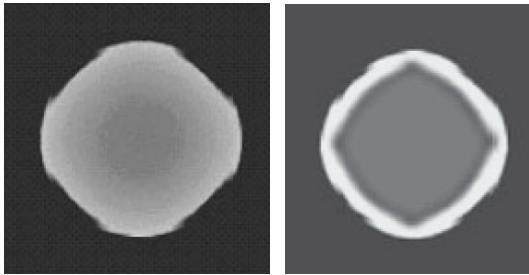


Figure 2-10: Simulation of solvent evaporation in nanofibers: (left) diffuse skin layer formation in relatively slow solvent loss, after 2.4 ms, and (right) sharp skin layer formation in rapid solvent loss, after 0.24 ms [23].

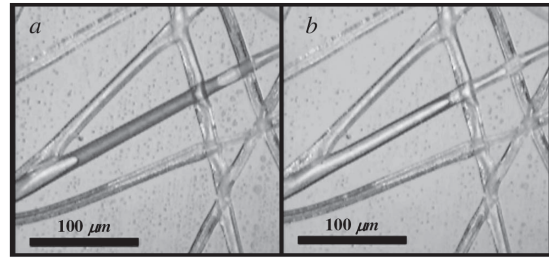


Figure 2-11: Electrospun tubular core-shell nanofibers: (a) entrapped slug bounded by two menisci, and (b) disappearance of this slug as a result of solvent evaporation [24].

Arinstein et al. [24] provide experimental and analytical assessments of the evaporation process and time, for tubular core-shell⁷ electrospun nanofibers, and argue, based on Guenther's observations, that it is similar to the process of solid-core nanofibers (Figure 2-11). An estimate for the evaporation time τ_e is given by

$$\tau_e = \frac{R_{cap} d_w}{2D_s} \approx \frac{10^{-5} \text{ m} \cdot 0.5 \times 10^{-6} \text{ m}}{2 \cdot 5 \times 10^{-13} \text{ m}^2/\text{s}} \approx 5 \text{ s}, \quad (2.9)$$

where R_{cap} is the internal core radius, D_w the skin thickness, and D_s the solvent diffusion coefficient (through the skin). This value is deemed to be a lower bound for the actual evaporation time in a solid-core fiber, but is much higher than Guenther's estimate.

⁷ Core-shell is an electrospinning method, using two polymer solutions drawn through two coaxial capillaries, obtaining a jet with two concentric layers, core and shell, whereby the outer layer (the shell) dries quickly, allowing investigation of the diffusion and evaporation of the inner layer (the core).

In summary, the conformal behavior of polymer chains throughout the electro-spinning process is a non-equilibrium state that depends upon the combined dynamic effects of stretching, evaporation and relaxation.

2.3 Mechanical properties of solid polymers

Polymer chains are essentially one-dimensional macromolecules, with strong covalent bonds along the chain's backbone structure, and side groups bonded to that structure. Lateral cohesion between chains (intermolecular interaction) is affected by entanglement and cross-linking, and by secondary bonds such as van der Waals forces, hydrogen bonds and dipolar bonds, which are of lower order of magnitude than covalent bonds. These properties determine, for a given polymer type, its nanoscale and microscale matrix structure, and consequently its mechanical properties.

The main physical and mechanical properties of interest of polymers are their specific mass, hardness, electrical conductivity, melting point, glass-transition point⁸, elasticity, ultimate strength, and color. The text books by Arridge [25], Nielsen [26] and Ward [27] provide a good overview of the scientific foundation for polymer mechanical properties; the following review is based mainly on these references. Numerous books, such as those by Mallick [28] and Daniel [29], deal with polymer-matrix composite materials⁹, and specifically with reinforced microfibers and their related design and application. Elastic theory is covered in the classic books by Landau [30] and Timoshenko [31].

Unlike metals and ceramics, which are composed of three-dimensional ordered structures of atoms, the physical and mechanical properties of polymers are the result of their chains conformation, cross-linking, crystallization and orientation. The polymer matrix structure consists of a network of entangled chains, with topological links preventing the crossing of chains (Figure 2-12a).

⁸ The glass-transition point T_g is the temperature above which the polymer's thermal expansion coefficient increases abruptly, causing transition from glassy state to rubbery state. T_g is below the melting point T_m .

⁹ A composite material consists of high strength and rigidity fibers, embedded in a polymer matrix.

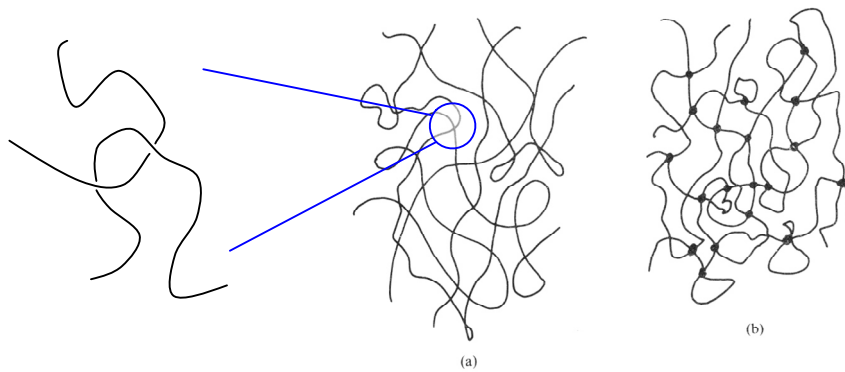


Figure 2-12: Classes of polymer matrix structure: (a) topological links (entanglement), and (b) cross-linking with chemical bonds. Adapted from [25].

Thus, the polymer solid bulk behavior can be described as sliding of chains, with little interaction between distant atoms, much like the behavior of super-cooled liquids. Additionally, in polymers such as rubber, thermosets and resins, chemical bonds create strong cross-linking between chains (Figure 2-12b).

Many polymers, such as polyethylene and nylon, tend to crystallize from a melt, forming small crystalline lamellae about 10 nm thick, which sometimes stack into ribbon-like or spherulites structures (Figure 2-13). On a higher scale, the crystallites are dispersed within regions of amorphous material, creating a structure similar to composite materials. The degree of **crystallization** (crystallinity index) is defined as the volume fraction of crystallites in the polymer, and can range from 30% to 90% in semi-crystalline polymers.

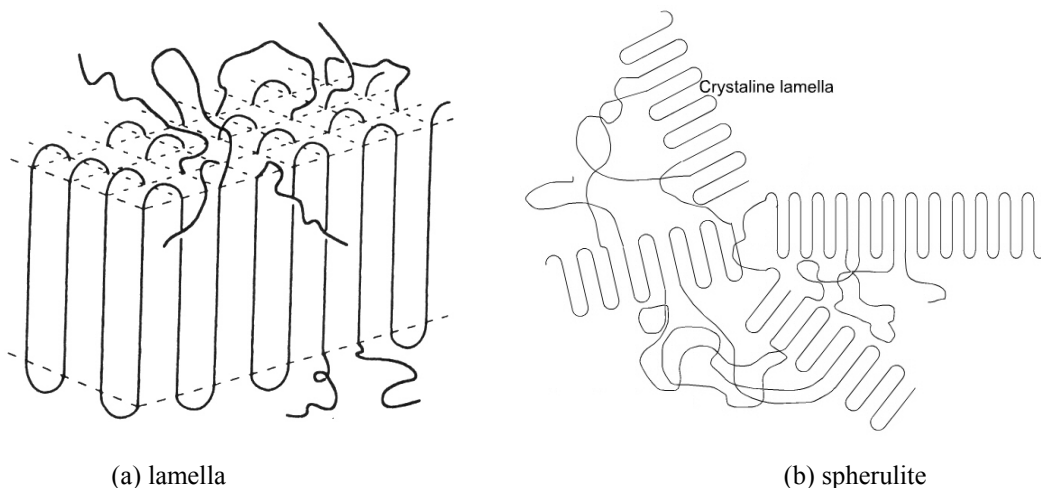


Figure 2-13: Schematic illustrations of polymer crystalline structure: (a) chain folding in a crystalline lamella; note that the chains are oriented across the lamella surface [26], and (b) spherulite semi-crystalline region [32].

When stretched, such as during electrospinning or cold drawing, the polymer matrix structure may possess a preferred **orientation** (alignment) of the amorphous

and crystalline regions. Stretching may also enhance the degree of crystallization, as it drives chains into adequate side-by-side three-dimensional position. Arinstein et al. [33] observed these phenomena in electrospun nanofibers, and measured the orientation factors of both the amorphous and crystalline regions, and the crystallinity index, using X-rays diffraction tests.

Simple analytical models predict polymer **elasticity** for two cases: the random coil, and the fully extended chain. These cases represent two extremes – the amorphous structure (in the rubbery state, above glass transition temperature T_g), and the crystalline structure, corresponding to complete disorder and complete order. These predictions are useful for determining the lower and upper bounds of polymer elasticity, and are therefore described ahead.

Random coil: The Helmholtz free energy F of an ideal chain under extension can be derived from Equation (A.5), using the Boltzmann relation for entropy $S = k_B \ln(\Omega) = const + k_B \ln[P(r)]$ ¹⁰

$$F = U - TS = const + \frac{3k_B T r^2}{2R_0^2}, \quad (2.10)$$

where $P(r)$ is the probability of the extension r , U the chain constant internal energy¹¹, k_B the Boltzmann constant, and T the temperature. The corresponding extension force f is

$$f = \frac{\partial F}{\partial r} = \left(\frac{3k_B T}{R_0^2} \right) r \quad \text{where} \quad R_0^2 = a^2 N, \quad (2.11)$$

implying a linear relationship between the force f and the end-to-end distance r [1, 34-35]. Thus, an ideal chain may be construed as an entropic spring, obeying Hooke's law for small elongations.

For large elongations, above one third of the fully extended length, more complex equations were derived (see for example Flory [25, 36]). Considering a freely-jointed chain subject to a constant elongation force f , and using the Gibbs free energy¹² G_{ibbs} , the extension r is given by [34]

¹⁰ Ω is the number of possible coil configurations for a given extension vector r , and is proportional to the probability $P(r)$. The Helmholtz rather than Gibbs free energy is used, since all possible coils correspond to a constant chain length (analogous to constant volume condition).

¹¹ The internal energy U is independent of chain conformation because an ideal chain assumes no interaction energy between distant monomers.

¹² The Gibbs free energy is used since the conditions are analogous to constant pressure.

$$r = -\frac{\partial G_{ibbs}}{\partial f} = aN \left[\coth(f_N) - \frac{1}{f_N} \right] \quad \text{where} \quad f_N = \frac{fa}{k_B T}, \quad (2.12)$$

where the function in square brackets is called the Langevin function. At small relative elongations r/aN , the function converges to Hooke's law of Equation (2.11); at large relative elongations, it deviates strongly from the linear behavior, and saturates at the maximal extension aN .

Similarly, at small elongations, the free energy F of a real chain under extension in a good solvent can be derived [1], implying a non-linear dependence of the extension force f on the end-to-end distance r

$$F \approx k_B T \left(\frac{r}{R_F} \right)^{1/(1-\nu)} \approx k_B T \left(\frac{r}{R_F} \right)^{5/2}. \quad (2.13)$$

Consider a network with N_{sc} ideal subchains per unit volume, where a subchain is a chain section between two cross-links. The network strain energy U_ε per unit volume, for a small strain $\varepsilon = r/R_0$, can be calculated with Equation (2.10) using only the elastic energy component

$$U_\varepsilon = F \cdot N_{sc} = \frac{3k_B T}{2R_0^2} \varepsilon^2 R_0^2 N_{sc} = \frac{3N_{sc} k_B T}{2} \varepsilon^2. \quad (2.14)$$

This model assumes the same average deformation energy for all N_{sc} subchains in the network, and that the network is in the rubbery state so that intermolecular motions are possible (see more details in [27]¹³). Using Hooke's law, the Young's modulus E is given by

$$E = \frac{\partial^2 U_\varepsilon}{\partial \varepsilon^2} = 3N_{sc} k_B T, \quad (2.15)$$

and the shear modulus G for an incompressible material is

$$G \equiv \frac{1}{3} E = N_{sc} k_B T = \rho R_{gas} T / M_{sc}. \quad (2.16)$$

where ρ is the material density, R_{gas} the gas constant, and M_{sc} the molecular mass of the subchain. This model is called rubber elasticity, and is applicable for temperatures above the glass transition temperature T_g . For large elongations, other more complex

¹³ The derivation of Equation (2.14) provided herein is different from the quoted reference, using a scaling approach.

rubber elasticity models exist – see reviews in [25, 27]. For typical polymers, the value of E according to this model is of order 1 MPa.

Fully extended chain: This model was developed by Treloar [37] for various crystalline polymers, using molecular mechanics methods (additional molecular mechanics models are reviewed in the book by Rappé et al. [38]). A planar extended chain with bond size l is subjected to force f at both ends (Figure 2-14). Each covalent bond has a tensile force constant k_l , and each vertex (the location of a carbon atom) has an angular force constant k_θ , both known from infrared data. The tetrahedral angle θ is the angle between the bond and the chain longitudinal axis. Intermolecular interaction forces can be ignored considering the ordered crystalline structure.

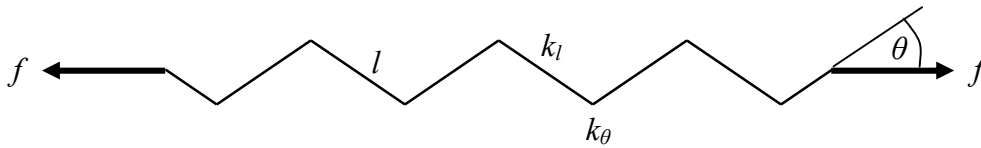


Figure 2-14: Fully extended chain model, showing a segment of a straight planar chain [37]. The vertices designate carbon atoms.

The elastic tensile modulus (Young's modulus) $E = \sigma / \varepsilon$ (σ – stress, ε - strain) was calculated from the total deflection δL_s caused by the force f , where L_s is the overall segment length, and A the chain cross-section estimated from measurements of intermolecular distances

$$E = \frac{f/A}{\delta L_s / L_s} \cong \frac{l}{A} \frac{\cos \theta}{\frac{\cos^2 \theta}{k_l} + \frac{l^2 \sin^2 \theta}{4k_\theta}}. \quad (2.17)$$

This equation holds also for a crystallite containing many such extended chains, arranged in an ordered structure. The calculated values for Young's modulus for polyethylene and nylon 66 are 182 GPa and 197 GPa, respectively, agreeing with experimental results of highly crystallized samples.

The modulus estimations obtained by these two models, for amorphous rubber elasticity and for crystallites, range from 10^6 Pa to 10^{11} Pa, an enormous gap. Amorphous polymers in the glassy state (below T_g) are more rigid ($E \sim 10^9$ Pa), because of the more restrictive nature of their intermolecular interactions. The free volume theory is one of the interpretations for these differences, stating that the intermolecular free space consists of van der Waals radii and additional volume for

vibrational motions. Up to T_g the free volume is fairly constant, while above T_g it starts growing with temperature, allowing the chains to move more freely.

The elasticity of semi-crystalline polymers has been estimated by models of aggregate crystallites, randomly oriented or with a preferred orientation, using methods similar to those used for composite material [25]. These methods can also be applied to amorphous polymers in the glassy state by assuming a certain degree of order (quasi-crystallites) in the matrix. Such methods may be useful for developing a model for nanofibers, explaining the effect of anisotropy on elasticity.

2.4 Mechanical properties of nanofibers

Substantial work has been reported on the elastic and strength properties of nanofibers, using both pure polymers and reinforced polymers [39-42]. A typical **stress-strain** behavior for CI-PP (Figure 2-15) and PVA (Figure 2-16), at various volume fractions of carbon nanotubes (CNT) filler, illustrates the elastic and plastic strain regions, and the effect of the reinforcing filler fraction.

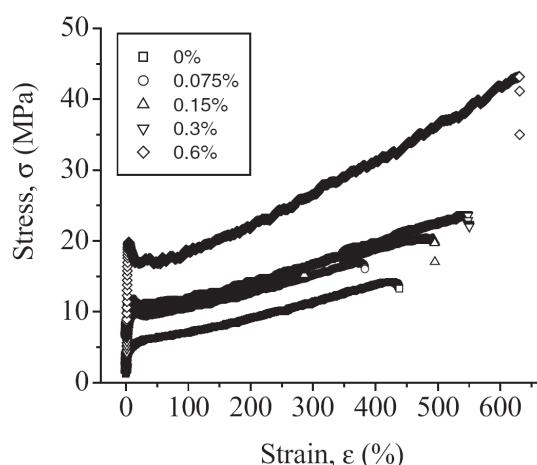


Figure 2-15: Representative stress–strain curves for electrospun CI-PP-based composites, for a range of nanotube volume fractions [41].

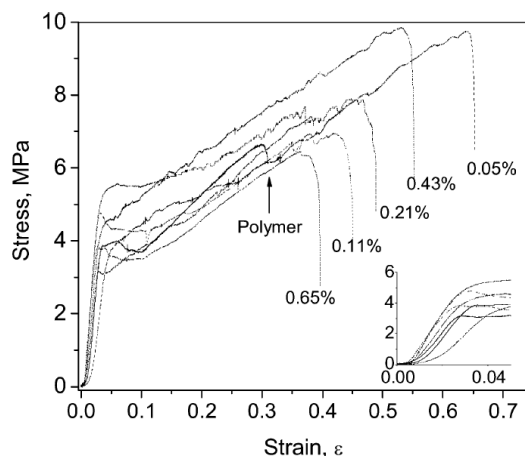


Figure 2-16: Representative stress–strain curves for PVA electrospun membranes, as a function of nanotube volume fraction [39]. Inset: the low strain region.

For bulk isotropic materials, the elastic modulus is an intrinsic property, independent of size and shape. However, there is growing evidence for size effects on the elastic properties of nanofibers and nanofilms made of different types of materials; yet, relevant data for polymer nanofibers is still limited. The following two works provide an experimental starting point for this research.

Ji et al. [43] investigated the elasticity of electrospun polystyrene (PS) nanofibers, using the three-point bending test (Figure 2-17), and observed a sharp increase in the tensile (Young's) modulus E with decreasing fiber diameter (Figure 2-18). The modulus rose from 4 GPa at a large fiber radius (i.e. bulk material), up to 40 GPa at radius of 100 nm, a factor of 10. PS, an amorphous polymer, exhibits similar behavior when in pure state or reinforced with CNT, however, the **crossover diameter** at which the modulus rises is larger for the reinforced material.

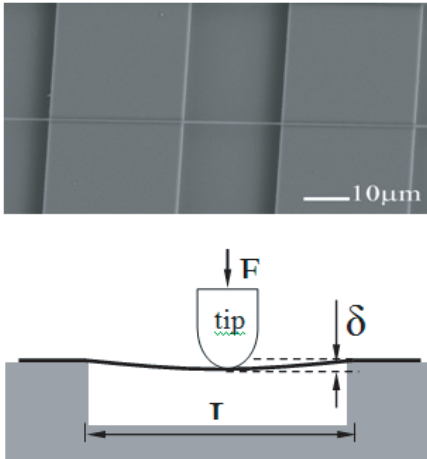


Figure 2-17: Schematic of the three-point bending method: a rounded AFM tip presses on the suspended fiber (without indentation), displacing it to a distance δ [43].

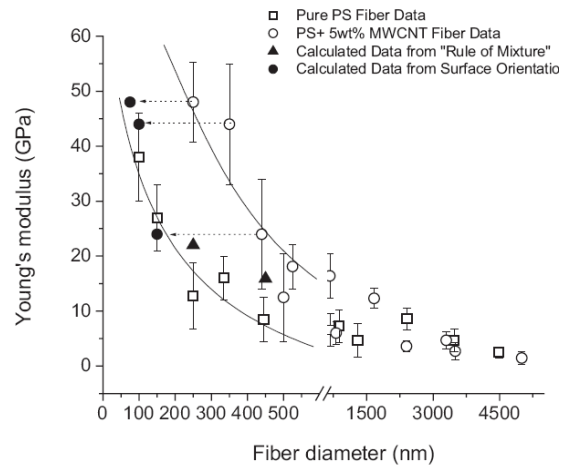


Figure 2-18: Young's modulus of PS for fibers of different diameters, with and without reinforcement [43].

Using shear modulation force microscopy (SMFM) (Figure 2-19) to measure the shear modulus G , and scaling the fiber radius by the radius of gyration R_g of various PS molecular weights, Ji et al. demonstrated a universal behavior (Figure 2-20), common to both moduli, different molecular weights, and both measurement methods, identifying the crossover of the moduli at fiber radius of $\sim 30 R_g$. These results clarify that the increase of the elastic modulus is a combined effect, dependent not only on the fiber radius but also on the size of the polymer macromolecules.

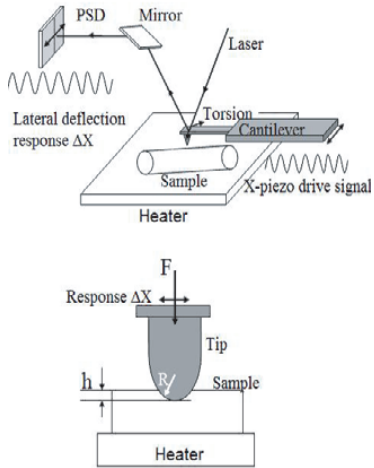


Figure 2-19: Schematic of the SMFM method: the fibers are indented by the AFM tip, and the deflection amplitude of an applied modulation is measured [43].

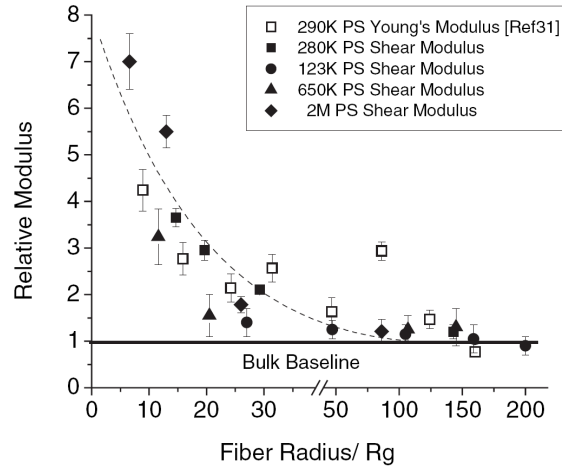


Figure 2-20: Relative tensile and shear moduli (E/E_0 and G/G_0 respectively) of fibers, versus their radius, scaled by R_g [43].

Similar phenomena was observed in tests conducted by Burman et al. [44] on nylon 66, a semi-crystalline polymer, using the single nanofiber tensile test and the free-flight pendulum test (Figure 2-21). Young's modulus rose by a factor of more than 30 at fiber diameter of 200 nm, and the crossover diameter was around 500 nm.

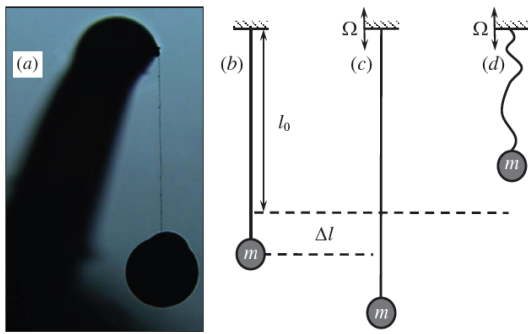


Figure 2-21: The string pendulum test: a ball is glued to a nanofiber and suspended from a cantilever beam, attached to a piezoelectric-actuated base. The pendulum's vibration consists of downward and free-flight upward motions, with a resonant frequency that allows calculation of the Young's modulus [44].

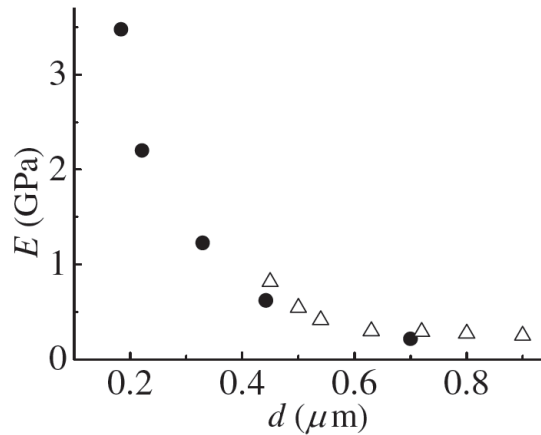


Figure 2-22: Young's modulus E of nylon 66 versus nanofiber diameter d , obtained by tensile tests (triangles) [33] and free-flight pendulum tests (circles) [44].

Arinstein et al. also measured [33] the degrees of crystallization and orientation for the same fibers used in the tensile and pendulum tests (Figure 2-23), and found that these parameters show only mild dependence on fiber radius, without visible crossover.

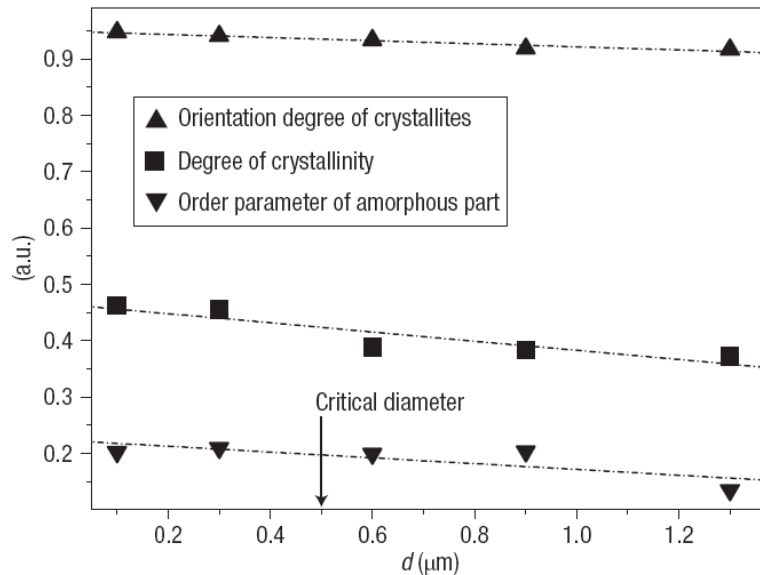


Figure 2-23: X-rays diffraction tests of electrospun Nylon 66 nanofibers: orientation degree of crystallites along the fiber axis, degree of crystallinity, and order parameter of macromolecule orientation in the amorphous part, versus fiber diameter d [33].

The effect of size on the tensile modulus was observed also on materials other than polymers, such as polypyrrole nanotubes (Figure 2-24), Ag nanowires (Figure 2-25) and Pb nanowires tested by Cuenot et al. [45-46], and Ag, Au, ZnO and Si nanowires tested by Park [47]. These experiments suggest that the dependence of the modulus on fiber diameter at nanoscale is a universal phenomenon, however the mechanism is not necessarily the same as for macromolecules.

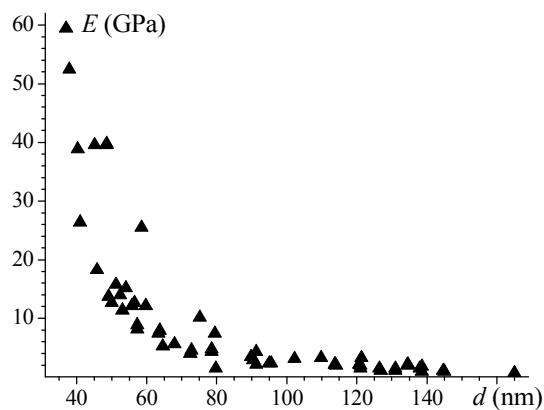


Figure 2-24: Three-point bending tests of polypyrrole nanotubes using AFM: relative Young's modulus (E/E_0) versus diameter d [46].

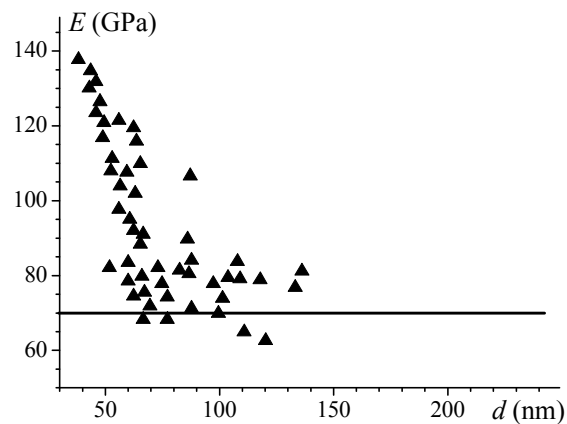


Figure 2-25: Three-point bending tests of Ag nanowires using AFM: relative Young's modulus (E/E_0) versus diameter [45].

In addition to elastic moduli, the **glass transition** temperature T_g is also affected by nanoscale sizes, as reported by Ji et al. [43] for PS nanofibers filled with CNT. Addition of 5 wt% CNT filler increases T_g by 10°C, explained by a reduction in the free volume due to adsorption of polymer chains onto the CNT, leading to further increase in the modulus. Conversely, de Gennes [48] reported that for PS films of thickness < 20 nm, smaller than R_g , the T_g was reduced, explained by more chain loops extending to the surface region of the thin film where the mobility is larger.

2.5 Theoretical explanations for size-dependent elasticity

The current literature provides three different theoretical explanations for the dependence of elasticity on nanoscale sizes:

- Surface tension – Cuenot et al. [46] and others [45-47, 49-50]
- Stretching – Ji et al. [43]
- Confinement - Arinstein et al. [33].

While surface tension only changes the apparent measured modulus, stretching and confinement cause anisotropy and change the material intrinsic modulus, as will be clarified further on.

Surface tension: Surface tension becomes a significant factor at nanoscale, since the ratio of surface area to volume is an inverse function of size. However, its effect depends on the mode of deformation and on geometry.

Under uniaxial stretching, the surface tension energy density U_{st} of a fiber is given by (assuming incompressible material)

$$U_{st} = \frac{\gamma \Delta S_f}{V_f + \Delta V_f} \approx \frac{2\pi R \gamma}{\pi R^2} \frac{\Delta L_f}{L_f} = \frac{2\gamma}{R} \varepsilon, \quad (2.18)$$

where L_f is the fiber length, S_f its surface area, V_f its volume, γ the surface tension, R the fiber radius, and ε the strain caused by surface tension; ΔL_f , ΔS_f and ΔV_f are the corresponding small changes due to surface tension. The surface tension energy is then proportional to the strain ε , unlike the elastic energy that is proportional to ε^2 (see, for example, Equation (2.14)).

The stress σ (compression) caused by surface tension is constant and does not depend on elongation, resulting in a constant compression strain ε of

$$\varepsilon = \frac{\sigma}{E} = \frac{1}{E} \frac{\partial U_{st}}{\partial \varepsilon} \approx \frac{2\gamma}{RE} = \frac{2 \cdot 0.05 \text{ N/m}}{10^{-7} \text{ m} \cdot 2 \cdot 10^9 \text{ N/m}^2} = 0.05\% \ll \varepsilon_{\max}, \quad (2.19)$$

where an estimate is given for fiber of radius of 100 nm and typical polymer properties, showing that the strain is quite negligible with respect to the maximal elastic strain ϵ_{\max} ($\sim 2\%$ for polymers in the glassy state – see for example Figure 2-16). Thus, surface tension does not adequately explain the observed increase in the elastic modulus of nanofibers under uniaxial stretching.

This, however, is not the situation in three-point bending. According to Cuenot et al. [46], the apparent Young's modulus E_{app} , calculated after taking surface tension effects into consideration, is given by

$$E_{app} = E_0 + \frac{(1-\nu)\gamma L_f^2}{5R^3}, \quad (2.20)$$

where E_0 is the material's bulk tensile modulus and ν the Poisson ratio, showing an added expression that strongly depends on the fiber radius R , as well as on the geometry and fiber clamping boundary conditions. Hence, E_{app} does not represent a change in the material intrinsic modulus, and cannot explain the effects during uniaxial stretching.

Stretching: The combination of the large shear imposed during electrospinning and the effect of surface tension orients the chains in the outermost regions of the fiber (Figure 2-26). Chain orientation starts at the surface and propagates into the bulk, fading gradually as the distance from the surface grows. The degree of orientation is determined by the number of monomers in contact with the surface, which has been shown to scale with R/R_g of the polymer [43].

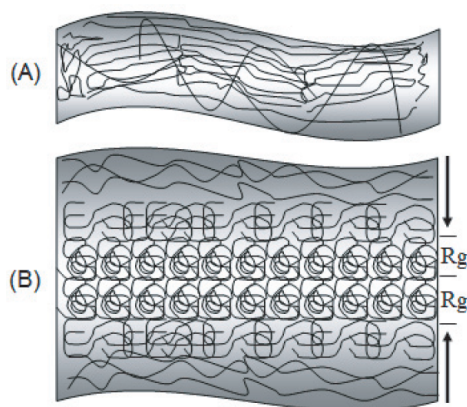


Figure 2-26: Model of the molecular chain orientation: (a) thin fiber - polymer chains orient through the entire fiber; and (b) thick fiber - polymer chain orientation starts at the surface and propagates into the bulk [43].

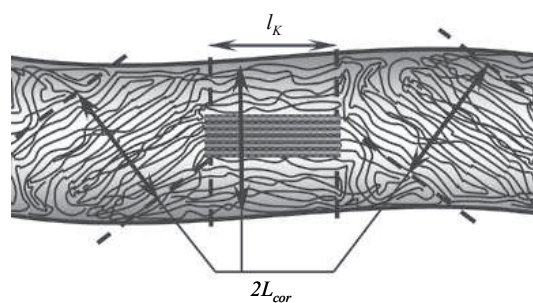


Figure 2-27: Arrangement of crystallites and oriented amorphous matrix in a polymer nanofiber. L_{cor} is the orientation correlation length within the amorphous polymer portion, and l_k is the length of the Kuhn segment [33].

Confinement: The size of regions consisting of orientation-correlated macromolecules is comparable to the nanofiber diameter, thereby resulting in confinement of the supramolecular structure (Figure 2-27). Rigid segments of the chain (i.e. Kuhn segments – refer to Appendix A and Equations (A.2) and (A.3)) are aligned to corresponding rigid segments in adjacent chains, forming a stack of many such segments, of thickness defined as the correlation length. Arinstein et al. [33] estimated the correlation length L_{cor} , based on the modified Onsager rigid rods model corresponding to the case of densely-packed rods

$$D = 2L_{cor} \sim \frac{2l}{\sqrt{1-\vartheta}} (n_k \ln \vartheta)^2 \approx 300_{\text{nm}} \quad (2.21)$$

where D is the size of the ordered region, l the bond size (0.1 nm), ϑ the free volume (8 %), and n_k the number of C-C bonds in a Kuhn segment (15 bonds). The size of the ordered region is, according to this estimation, of the same order of the fiber diameter, thereby confining the supramolecular structure, and forcing alignment in the amorphous and crystalline regions. According to Ji et al. [43], the addition of CNT filler enhances the effect of confinement due to the added CNT interface area.

3. Motivation and research goals

3.1 Information gaps

Substantial research has been performed on the macro-mechanical properties of nanofibers, including the effects of material, size, and reinforcement, but the explanations for their unique properties are mostly descriptive and qualitative, leaving several open questions. The size-dependence of the elastic properties was characterized by experiments (Section 2.4), yet the underlying physical mechanisms are conjectured with diverse explanations such as surface tension, confinement and stretching (Section 2.5), which are currently supported by very preliminary calculations and lack detailed theoretical and experimental justification.

The research problem involves several interrelated parameters, illustrated in Figure 3-1 in relation to the electrospinning process and its outcome. These parameters belong to two areas: the effect of electrospinning on the solid polymer nanostructure; and the effect of the nanostructure on the elastic properties.

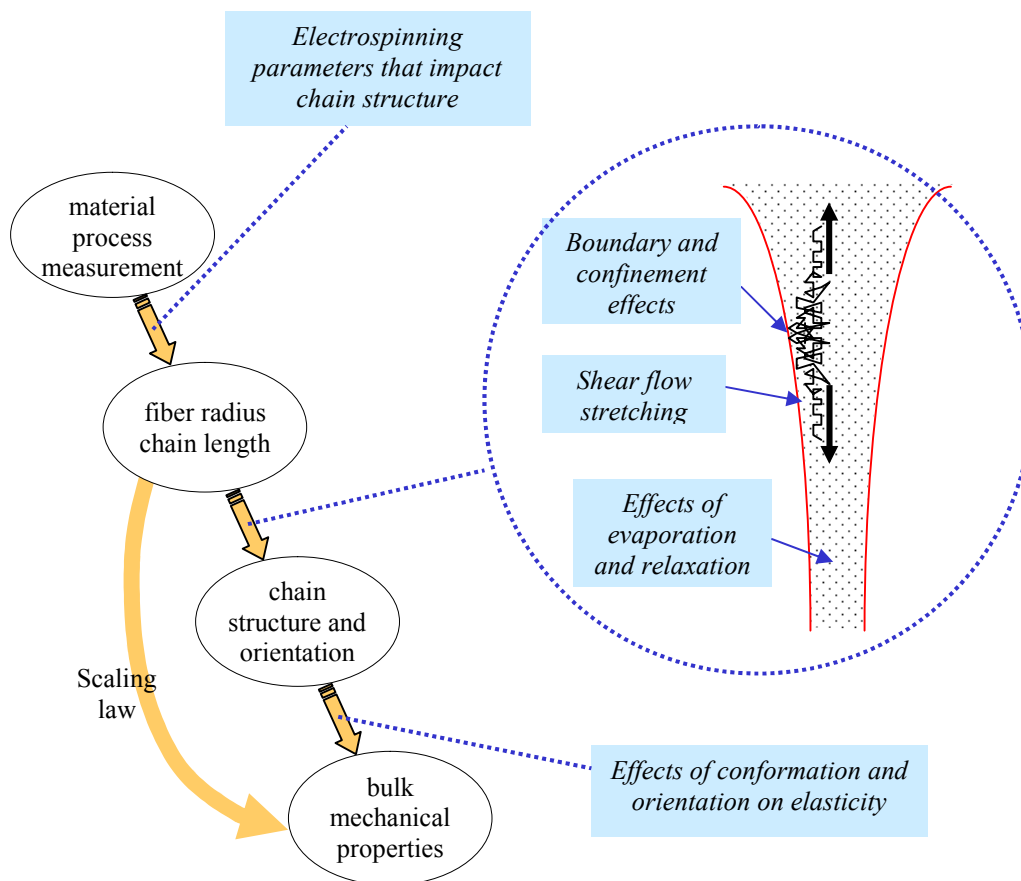


Figure 3-1: Diagram of research parameters (boxes), in relation to the electrospinning process and outcome (bubbles).

The effects and mechanisms of boundary, confinement, stretching, evaporation and relaxation have been generally investigated in polymer physics (Sections 2.1), with some application to electrospinning (Sections 2.1, 2.2 and 2.5). However, we still miss a comprehensive model that links their combined influence on the macromolecular structure generated by electrospinning, leaving the following information gaps unresolved:

- How do the jet boundary and other confinement effects influence chain conformation?
- What is the axial stretching and radial contraction mechanisms of a polymer network in a jet?
- What is the relaxation mechanism of a polymer network in a jet, considering the partial evaporation and solidification during electrospinning?
- How does the polymer molecular weight affect network stretching and relaxation, and subsequently chain conformation?
- What is the orientation of individual chain links, during and after electrospinning?

There are a few models relating the solid polymer macromolecular structure to its mechanical properties (Section 2.3), including the effects of crystallinity and glass transition. The application of such models to the macromolecular structure generated by electrospinning could help answering the following information gaps:

- What is the mechanism by which the global chain conformation and orientation affect elasticity, including interaction and ordering between chains (e.g. the correlation length)?
- What is the mechanism by which the local chain conformation (i.e. the orientation of chain links) affects elasticity?
- How does the statistical distribution of orientation angles affect elasticity?

3.2 Motivation

This research seeks to provide a deeper insight into the nanoscale mechanisms affecting the macroscale properties, to develop quantitative models explaining the phenomena, and to validate them by specially planned experiments.

The literature review (Section 2) and the preliminary results of the research (Section 5) revealed some behavioral trends, suggesting possible hypotheses. The research will attempt to validate (or reject) the following hypotheses:

- Stretching, rather than boundary and confinement effects, is the main cause of orientation (Sections 5.25.4).
- Given certain jet conditions, stretching and orientation may undergo a phase transition resulting in almost full extension of the chain (Sections 5.4 and 5.5).
- Orientation is more dominant in the fiber skin than in the fiber core, because of the more rapid solidification of the skin (Section 2.2).
- Local orientation of chain elements (and its statistical distribution), rather than global chain conformation, is the main factor affecting solid elasticity (Sections 2.3 and 5.6).
- Physically meaningful scaling law(s) can be constructed regarding the correlation between the nanofiber diameter and the mechanical properties and fabrication parameters (Section 5.1).

3.3 Research goal and objectives

The research goal is to investigate the effect of the polymer matrix structure on the mechanical properties of electrospun nanofibers. The detailed research objectives follow, grouped in relation to the polymer state during the process:

- Investigate the effects of electrospinning on the nanostructural conformation and orientation, during the **solution** state:
 - Investigate the effects of the jet boundary and confinement.
 - Investigate the effect of the network axial stretching and radial contraction.
 - Investigate the influence of the polymer molecular weight.

- Investigate the effects of solidification on the nanostructural conformation and orientation, during the **partially-solid** state:
 - Investigate the transient effects of evaporation, partial solidification and relaxation.
 - Determine the final global chain conformation and local orientation.
- Investigate the effects of the **solid** state nanostructure on the nanofiber mechanical properties, particularly elasticity:
 - Investigate the effect of the global chain conformation.
 - Investigate the effect of the local chain conformation, particularly local orientation.
 - Investigate the influence of orientation statistics.

The objectives will be achieved by combining theoretical, simulation and experimental work. Simplified models and random walk simulations will help in gaining insights and trends, and will guide the planning of the experimental work. The experiments will study the nanofibers solid elastic properties by tensile testing and, when needed, the nanofibers morphology by electron microscopy and X-ray.

Factors expected to influence the nanostructure during the polymer solution state are the rheological and electrical properties of the polymer solution; the process parameters (electrostatic field, flow rate, ambient conditions); the polymer molecular weight and the type of solvent; the boundary and confinement effects; the magnitude (i.e. gradient) of the jet shear flow; the rapid and non-uniform evaporation of the solvent; and the inherent chain relaxation elastic forces. Factors expected to influence the mechanical properties of the solid polymer are the global macromolecular conformation of chains; the global orientation of chains; the interaction between chains and the glass transition temperature; and the local orientation of chain elements.

The results of the proposed research will provide:

- Insight into the nanoscale structural features that determine the mechanical properties.
- Insight into the electrospinning variables that impact the significant structural features.

4. Methodology and research program

The research methodology and program consist of theoretical modeling and simulation of the macromolecular structure, fabrication of nanofibers by electrospinning, and characterization of the nanofibers mechanical properties and morphology.

4.1 Theoretical modeling and simulation

Experimental characterization of nanofibers morphology requires substantial effort, especially in view of the many parameters involved in electrospinning and the non-linearity of the size-dependence phenomenon. Furthermore, the correlation between the nanostructural orientation and the elastic properties is not conclusive in view of experimental results (Figure 2-23). Hence, the research will first create a theoretical foundation by using effective and flexible analytical tools, the results of which will guide the planning and execution of experiments. We plan to use two types of analysis tools: random walk simulation; and computational micromechanics modeling.

Random walk (RW) simulation of a polymer chain in solution state can be an effective tool when the theoretical solution is too complex, when visualization of the behavior of an individual chain is desired, or when applying complex boundary constraints and potential fields (e.g. a flow field).

RW simulation consists of generating a large enough sample of individual walks, each representing a possible chain conformation, and then performing statistical inference to obtain information on chain parameters. Inference may include finding the average (mean) of variables, such as the chain end-to-end distance or density of monomers, as well as other statistical metrics like the variable mode (most frequent value), its dispersion, its symmetry, and more. The preliminary research (Sections 5.3 and 5.4) has already demonstrated that, under the effects of boundary or strong extensional flow, the statistical conformation of polymer chains is not Gaussian and sometimes is even bimodal, thereby making the analytical solution unattainable or extremely difficult.

Although RW is efficient in providing the complete conformational statistic of a chain, the applicability of the method to this research requires some simplifying assumptions on chain type, dimensionality, walk type, and monomers connectivity. These issues are broadly discussed and justified in Section 5.3.

The RW simulation tool, developed and used in the preliminary research, will be used extensively to investigate the chain conformation and orientation during the solution state and the partially-solid state of the polymer. Keeping in mind its limitations, the simulation results are expected to reveal trends and tendencies in the development of the conformation as a function of key process variables such as molecular weight, flow velocity gradient, and solution viscosity.

The RW tool will be expanded to incorporate special effects, including the saturation of the jet velocity and consequently the diminishing of the flow gradient; the slipping of subchains due to the strong extensional forces (i.e. shifting of the network topological links); the connectivity of the network subchains preventing the network from relaxing freely even after the disappearance of the velocity gradient; and the transient and non-uniform effect of evaporation.

The RW tool will be further expanded to incorporate two-dimensional simultaneous axial stretching and radial contraction. Three-dimensional random walk is not needed due to the fiber's axial symmetry. It is expected that the two-dimensional tool will provide the statistics of the chain global and local orientation (see preliminary approach in Section 5.6).

Computational micromechanics methods have been used to model the elasticity of semi-crystalline polymers, assuming aggregate crystallites randomly oriented or with a preferred orientation (Section 2.3). These methods can also be applied to amorphous polymers in the glassy state by assuming a certain degree of order (quasi-crystallites) in the matrix. Such methods may be useful for developing a model explaining the effect of anisotropy on nanofibers elasticity. The focus will be on amorphous polymers since the crystallinity of some polymers, as well as reinforcement with filler material, introduce an additional level of research complexity that might obscure the basic mechanisms.

The mechanical properties will be investigated by treating the nanofiber solid microstructure as an anisotropic material. The method consists of homogenizing the structure by building the smallest possible element (i.e. a representative volume) that still retains the average anisotropic nano-mechanical properties of the polymer, and then calculating the bulk elasticity by incorporating the chain orientation statistics. The bulk properties are calculated by integrating the local properties over the whole volume of the nanofiber, assuming isostrain or isostress loading, or by solving a finite-element model (e.g. using the Abaqus software) consisting of many

representative volumes, each oriented differently in accordance with the orientation statistics.

A complete and accurate modeling of polymer mechanical properties based on the as-spun nanoscale properties is beyond the scope of this research program, requiring consideration of global chain conformation and orientation, inter-chain interactions, and local properties such as chain-element orientation. By contrast, computational micromechanics methods assume morphological uniformity (though anisotropic), and therefore can be applied reasonably in modeling the effects of local properties. Thus, the purpose of this task will be to characterize behavioral trends rather than provide a comprehensive elasticity model for electrospun nanofibers.

The random walk simulation and the computational micromechanics modeling will provide:

- Insight into the chain conformation.
- Insight into the coil-stretch transition phenomenon and the variables affecting it.
- Insight into the process parameters affecting local orientation.
- Evaluation of the dependence of elasticity on the orientation statistics.
- Explanation for the sharp rise in the elastic moduli.

4.2 Nanofibers fabrication using electrospinning

Nanofibers will be fabricated by electrospinning, whereby the materials and process parameters will be selected so that certain hypotheses and trends revealed in the analytical work could be put to test. As with the theoretical analysis, the focus in fabrication will be on amorphous polymers (e.g. PMMA or PS), thereby reducing the level of complexity and gaining insight on the basic underlying mechanisms. Two types of tests are planned: molecular weight effects; and coil-stretch transition.

Molecular weight effects were tested on PS (Section 2.4) at SUNY, showing their impact on elasticity. However, their effect on morphology was not shown. Tests at the Technion included measurement of orientation in Nylon 66, but were done for a single molecular weight. The preliminary analysis in Section 5.6 clearly demonstrates the dependence of orientation on the length of a subchain (and indirectly on the chain length). This information gap can be investigated by experiments in which the polymer molecular weight will be varied using several values, each with a narrow dispersion of the degree of polymerization.

The experiment can be conducted under conditions of constant jet velocity gradient, constant solution concentration (or viscosity), or constant fiber diameter, allowing isolation of the molecular weight factor from other factors. In order to achieve such constant conditions, the governing parameters of the electrospinning process (e.g. electrical field, flow rate, evaporation rate, and collection velocity) will be controlled accordingly. For example, by keeping the relative solution concentration c/c^* constant a (fairly) constant fiber diameter can be achieved (see Figure 2-7); by adjusting the flow rate and electrical field in a certain way one may obtain a constant velocity gradient.

The elastic modulus of these fabricated nanofibers will be tested and, if needed, their nanostructural morphology will be measured – see Section 4.3.

Coil-stretch transition depends on the flow velocity gradient (growing with the global position along the jet) and is more pronounced for longer chains (Section 5.4). It is predicted that above certain jet gradients a sharp change in chain conformation occurs, causing transition from a Gaussian-like coil to an almost fully-stretched chain. This prediction relies on rough estimates of the velocity gradient, and therefore an experiment should be carried out to validate its occurrence. The dependence on chain size (i.e. molecular weight) leads to anticipation that this experiment will reflect a phase transition by showing a sharp increase in the orientation order above a certain molecular weight. However, in view of the results in Figure 2-23 this expectation may not be substantiated.

The suggested experimental approach is to detect where along the jet an orientation phase transition occurs. This could be achieved by varying the distance of the collector from the capillary, and freezing the nanofiber in liquid nitrogen so that its nanostructure is retained. Thereafter the solvent can be drained by sublimation in low pressure, and the orientation measured and calculated as a function of the location along the jet (i.e. the collector distance). This experiment should be performed at fixed electrospinning material, solution and conditions, which should be carefully selected based on calculations.

The molecular weight and coil-stretch transition experiments will provide:

- The correlation between molecular weight and nanostructural orientation, including an anticipated crossover value.
- The influence of the fabrication conditions on the universal scaling law.
- The validation / rejection of the occurrence of an orientation phase transition in electrospinning.

4.3 Characterization of mechanical properties and morphology

Experimental characterization encompasses mechanical testing of fabricated nanofibers to determine their mechanical properties, and imaging of their molecular morphology to learn about their crystallinity and orientation.

Tensile tests will be performed on the fabricated nanofibers to determine their elastic modulus. Tests can be performed on single nanofibers, a difficult task requiring micro-manipulation, or on dense as-spun mats of well-oriented nanofibers (Section 2.4). Mats are easier to test than single nanofibers, and are therefore the preferred approach, but their properties have a larger variation due to non-uniformity in fibers diameters, misalignments of fibers, sliding between fibers, and inaccuracy in measuring the mat density.

The measurements will be conducted with as-spun nanofiber mats on a dynamic mechanical thermal analysis (DMTA) machine. The elastic tensile modulus (Young's modulus) will be measured by slow force loading. The storage and loss moduli will be measured by applying a force oscillation. In addition, the test may include measurement of the shift of the glass transition temperature with respect to bulk material, by stretching the test sample to a certain level of strain, and then raising the temperature and detecting the instance of strain relaxation.

Imaging experiments outside the optical range will be considered, depending on the benefit and amount of effort. Scanning electron microscopy (SEM) and transmission electron microscopy (TEM) imaging may be carried out on samples made of as-spun fibers, in order to measure the nanofibers diameters and to study their morphology. Scattering techniques, including the wide angle X-ray scattering (WAXS) and small angle X-ray scattering (SAXS) may be used to measure the degree of crystallinity and the orientation of the amorphous and crystalline regions.

The characterization of the mechanical properties and morphology will provide:

- The correlation between the molecular weight and the elastic modulus, including an anticipated crossover value.
- The correlation between the nanostructural orientation and the elastic modulus.
- Evaluation of the elastic modulus dependence on the fabrication conditions.

4.4 Time table

Table 4-1: Research program time table.

Completion of RW simulation of network conformation	Feb 2010
Modeling of local orientation statistics	Apr 2010
Micromechanical modeling of elastic modulus	Jul 2010
Fabrication of nanofibers with various molecular weights	Oct 2010
Fabrication of nanofibers with frozen conformations	Feb 2011
Characterization of mechanical properties and morphology	May 2011
Analysis of experimental results	Aug 2011
Preparation of PhD thesis	Nov 2011

5. Preliminary results

This section describes the preliminary work accomplished as part of this research, addressing the following research subjects:

- Scaling law correlating elastic moduli to fiber radius and chain length
- Chain conformation between two boundaries
- Random walk simulation tool
- Single chain stretching under electrospinning shear flow
- Network stretching under electrospinning shear flow
- Transversal contraction due to electrospinning stretching.

5.1 Scaling law correlating elastic moduli to fiber radius and chain length

The experimental data presented in Section 2.4 implies the existence of a universal rule linking the elastic modulus to the fiber radius and chain length (expressed by the radius of gyration R_g). The literature review revealed that such a linkage involves complex phenomena and effects, and therefore an empirical scaling law could help in evaluating theoretical models and test results.

We first examine the various **scales** present in a typical nanofiber (Figure 5-1), in search for suitable parameters of the same order of magnitude as the fiber radius R . Relevant parameters are the chain radius of gyration R_g , the correlation length L_{cor} , and the effective Kuhn segment. The other parameters seem too small to be relevant.

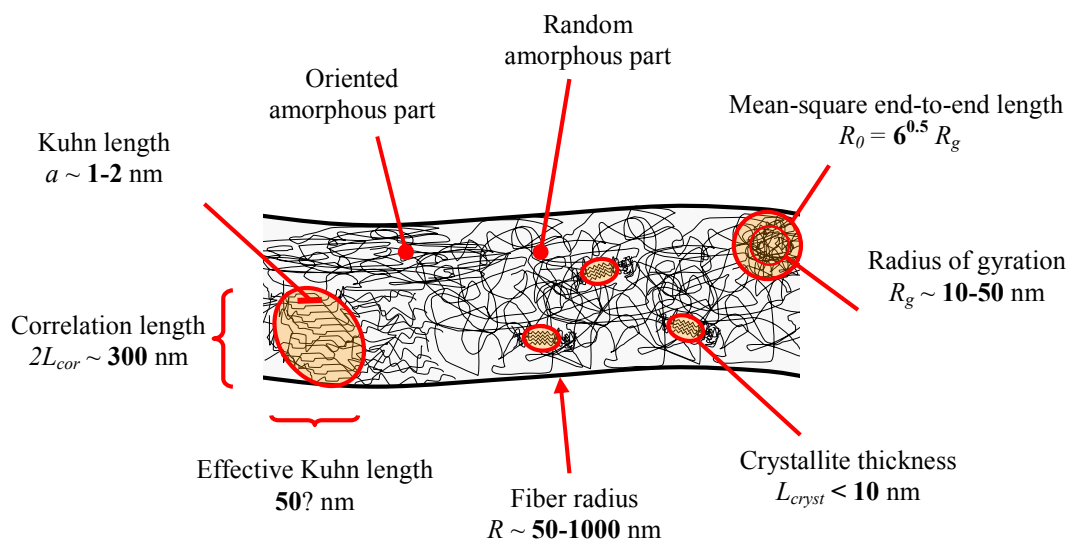


Figure 5-1: Scales in nanofibers. The terms are defined and described in Section 2.

Following the logic of Section 2.5, that surface contacts enhance chain stretching, a simple **scaling law** can be derived for the number fraction P of chains in contact with the fiber surface, as a function of the average coil radius R_g and the fiber radius R (Figure 5-2).

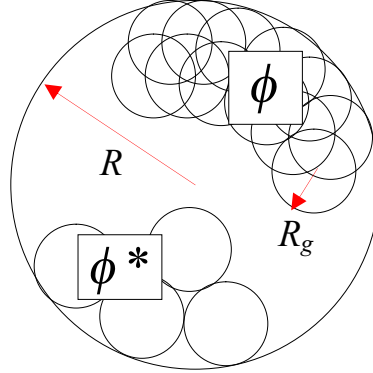


Figure 5-2: Arrangement of coils of gyration radius R_g within the cross-section of a nanofiber of radius R . The crossover volume fraction ϕ^* and the actual volume fraction ϕ are indicated.

At the crossover volume fraction ϕ^* , the number fraction P is given (in three dimensions) by

$$P(\phi^*) = \frac{n_S}{n_V} \cong \frac{2\pi(R - R_g)/4R_g^2}{\pi R^2 / \frac{4}{3}\pi R_g^3} \cong \frac{2\pi}{3} \left(\frac{R}{R_g} \right)^{-1} \quad \text{for } R \gg R_g, \quad (5.1)$$

where n_S is the number of chains in contact with the surface and n_V the total number of chains, per unit length of the fiber. The number of chains n_S and n_V increase as a function of the actual volume fraction ϕ , and their ratio is then corrected by the factor

$$\frac{n_S}{n_V} = \frac{(\phi/\phi^*)^{2/3}}{(\phi/\phi^*)} = \left(\frac{\phi}{\phi^*} \right)^{-1/3}. \quad (5.2)$$

The number fraction P is corrected accordingly to

$$P(\phi) = P(\phi^*) \left(\frac{\phi}{\phi^*} \right)^{-1/3} \cong \frac{2\pi}{3} \left(\frac{R}{R_g} \right)^{-1} \left(\frac{\phi}{\phi^*} \right)^{-1/3} \quad \text{for } R \gg R_g. \quad (5.3)$$

Given N elements of size a in each chain, the ratio ϕ/ϕ^* can be calculated using the crossover mass concentration c^* from Equation (2.1), and the scaling relationship at no free volume $c \sim a^{-3}$

$$\frac{\phi}{\phi^*} = \frac{c}{c^*} \cong \frac{1/a^3}{N^{1-3\nu}/a^3} = N^{3\nu-1} \cong \left(\frac{R_g \sqrt{6}}{a} \right)^{(3\nu-1)/\nu}, \quad (5.4)$$

where N was replaced by R_g and a from Equation (A.8). Substituting Equation (5.4) into Equation (5.3), the final expression for the number fraction of surface contacts is

$$P \cong \frac{2\pi}{3} \left(\frac{\sqrt{6}}{a} \right)^{1/3\nu-1} \frac{R_g^{1/3\nu}}{R} \sim R^{-1} R_g^{1/3\nu} \quad \text{for } R \gg R_g. \quad (5.5)$$

For ideal chains, and real chains in good solvent, this scaling law can be written

$$\begin{aligned} \nu = \frac{1}{2} \quad P_{ideal} &\sim R^{-1} R_g^{2/3} \\ \nu = \frac{3}{5} \quad P_{real} &\sim R^{-1} R_g^{5/9}. \end{aligned} \quad (5.6)$$

Even though this law does not provide information on chain conformation or orientation, it implies a power scaling law of type $R^x R_g^y$, which can be used as a first estimate for the experimental data. Like all scaling laws, this law is valid only within a limited range of parameters, more specifically when $R \gg R_g$. At very small fiber radii R , the number fraction of contacts P should saturate rather than converge to infinity. This is true for the experimental data as well, although it does not show on the plots because the conditions were far from the saturation region.

The experimental data from Ji [43] and Burman [44] was fitted to the scaling law $R^x R_g^y$. The data was first adjusted to suit a power curve by using a relative delta modulus rather than a relative modulus, defined as

$$\frac{\Delta E}{E_0} \equiv \frac{E - E_0}{E_0} \quad \text{and} \quad \frac{\Delta G}{G_0} \equiv \frac{G - G_0}{G_0}, \quad (5.7)$$

where E_0 and G_0 are the bulk tensile and shear moduli respectively. The power dependence of the experimental moduli on R is presented in Figure 5-3, along with the scaling law of Equation (5.5).

Using bivariate curve fitting, the data from Figure 2-20 was fitted to both R and R_g , yielding the following scaling law:

$$\frac{\Delta G}{G_0} \sim R^{-1.31} R_g^{1.60} \quad \text{with SE} \sim \pm 15\%. \quad (5.8)$$

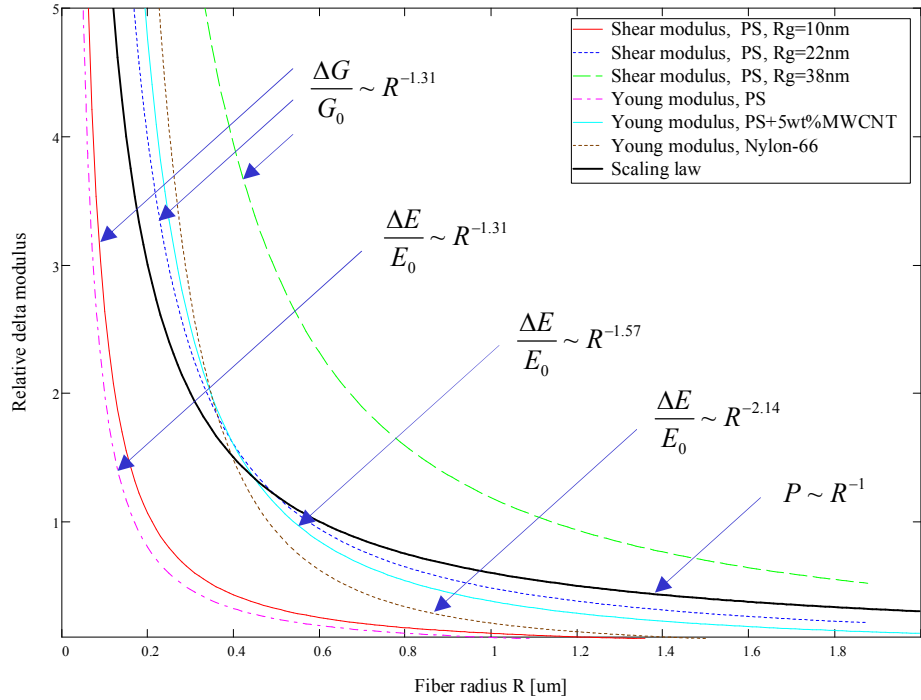


Figure 5-3: Scaling of relative delta moduli to fiber radius R : experimental data from Figure 2-18, Figure 2-20 and Figure 2-22, and scaling law from Equation (5.5). The number fraction of surface contacts P is normalized for plotting purposes. The curve fitting SE is $\sim \pm 15\%$.

The following concluding observations can be noted:

- The tensile modulus E and the shear modulus G behave similarly with respect to their dependence on R .
- The exponent of R for the various experiments varies from -1.31 to -2.14 (SE $\sim \pm 15\%$).
- CNT filler (in PS) and higher crystallinity (in Nylon 66) increase the dependence on R (higher exponent).
- The crossover radius depends strongly on R_g and on material; the crossover is at $R / R_g \sim 25$.
- The theoretical scaling law of Equation (5.5), based on geometry alone, shows weaker dependence (smaller exponents) on R and R_g compared to the experimental results.

The experimental and theoretical scaling laws derived in this section provide a quantitative measure for the dependence of elasticity on fiber radius and chain size. However, without information on chain conformation or orientation these scaling laws do not help us in understanding the physical mechanism behind the size dependence. This is the subject of the next sections.

5.2 Chain conformation between two boundaries

When ideal chains are free to move, their end-to-end distance has a Gaussian distribution, described by Equation (A.5). However, whenever a chain is in contact with a boundary, such as the outer surface of a nanofiber, it will either stick to it or bounce back, depending on whether the boundary is adsorbent or repulsive, and the chain's conformation and orientation will be affected. A theoretical model can be obtained by solving the diffusion equation (A.6) for suitable boundary conditions.

A simple representation of this scenario is a one-dimensional ideal chain model, without external forces (i.e. no flow field). The ideal chain is an acceptable approximation for the semi-dilute solution used in electrospinning, assuming quasi-static conditions (enough time for relaxation / reptation). The one-dimension simplification provides an upper bound, meaning that in higher dimensions the average effect of the boundary is expected to be lower¹⁴.

In one dimension, the boundaries of a nanofiber can be represented by two walls distanced $2R$ apart, and the solution of the diffusion equation, for a chain of N elements of size a , is given by the **chain lengths distribution** $f(x)$

$$f(x, x_0, N) = G(x, -x_0 - 2R, N) + G(x, x_0, N) + G(x, -x_0 + 2R, N), \quad (5.9)$$

$$\text{where } G(x, x_0, N) = \frac{1}{\sqrt{2\pi a^2 N}} \exp\left(-\frac{(x - x_0)^2}{2a^2 N}\right), \quad (5.10)$$

x is the one-dimensional chain end position, and x_0 is the chain starting position. The expression $x - x_0$ is the chain end-to-end distance. The solution is depicted in Figure 5-4, showing “mirroring” of the Gaussian distribution by the walls.

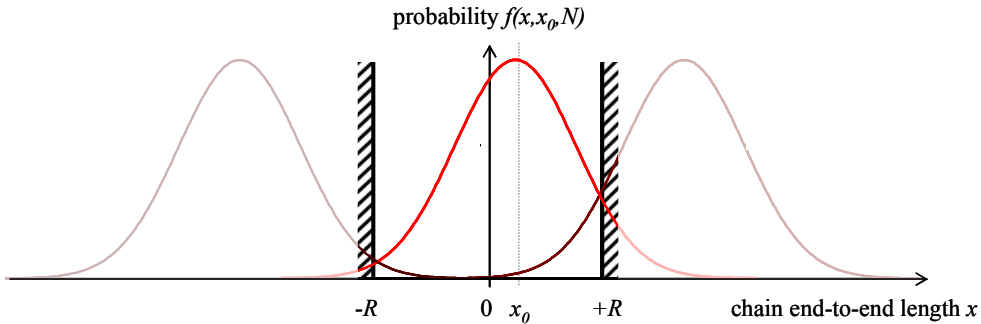


Figure 5-4: Distribution of one-dimensional chain end position x between two boundary walls, for starting point x_0 .

¹⁴ In higher dimensions the closer regions of the boundary have a stronger effect than the farther regions, and therefore the overall average effect is weaker than in one dimension.

Results for several starting points x_0 are presented in Figure 5-5. The chain end position x is normalized by R_g of Equation (A.4)¹⁵, making the graph universal as well as comparable to experimental results. The plot shows that the boundary effect is significant for chains whose starting point is up to $5R_g$ away from the wall.

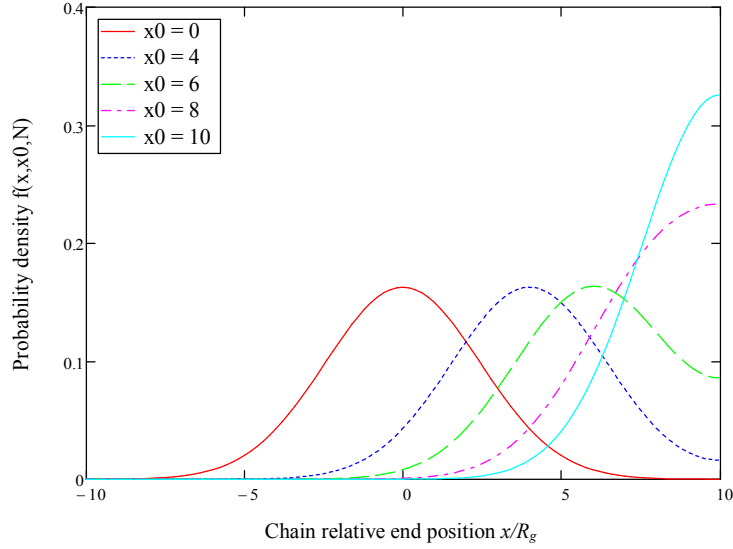


Figure 5-5: Distribution of relative chain end position x/R_g , for several chain relative starting points x_0/R_g . The range of x/R_g (± 10) was selected in relation to the boundary effect size.

The **statistical moments** of the distribution provide a quantitative measure for the size, shape and symmetry of the distribution, and hence for the boundary effect. The central moments Mn of the distribution $f(x)$ are given by

$$M1(x_0) = \int_{-R}^R x f(x, x_0) dx \quad (5.11)$$

$$Mn(x_0, n) = \int_{-R}^R [x - M1(x_0)]^n f(x, x_0) dx,$$

where $M1$ is the mean (first moment) and Mn is the central moment n . These equations become universal by rewriting

$$M1(\lambda_0) = R_g \int_{-R/R_g}^{R/R_g} \lambda f(\lambda, \lambda_0) d\lambda = R_g \Psi(\lambda_0) \quad \text{where} \quad \lambda \equiv \frac{x}{R_g}, \lambda_0 \equiv \frac{x_0}{R_g} \quad (5.12)$$

$$Mn(\lambda_0, n) = R_g^n \int_{-R/R_g}^{R/R_g} [\lambda - R_g \Psi(\lambda_0)]^n f(\lambda, \lambda_0) d\lambda = R_g^n \Psi n(\lambda_0, n),$$

¹⁵ For the purpose of comparing to experimental results, the three-dimensional R_g was used for normalization throughout this analysis.

where λ and λ_0 are dimensionless position variables, and Ψ and Ψ_n are dimensionless functions resulting from the integration. It is then possible to normalize the moments by R_g^n , leaving only the boundary effect dependence on the chain normalized starting point λ_0 . Hence, the model could be run with $R_g = 1$ without losing information.

The first ten moments of the distribution are presented in Figure 5-6, asserting that the boundary effect persists up to a distance of $\sim 5R_g$.

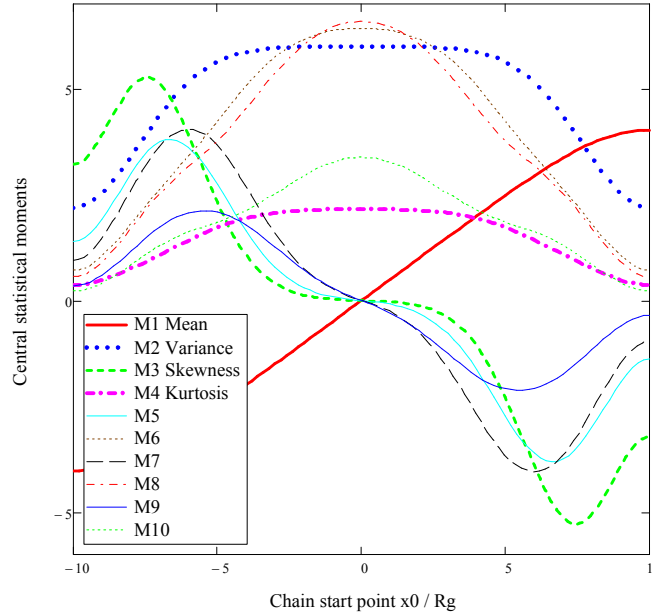


Figure 5-6: First ten central statistical moments of the end-to-end chain lengths distribution, versus the chain relative starting point x_0/R_g .

The distribution of monomers (or chain elements) within the chain is another criterion for the chain's conformation and orientation. The **mass density distribution** Nm of monomers in a chain (i.e. the number of monomers per unit volume) can be obtained by integrating the distribution function $f(x)$ in Equation (5.9) over the variable n_m , where n_m is the number of monomers (or chain elements) ranging from 1 to N

$$Nm(x, x_0, N) = \int_1^N f(x, x_0, n_m) dn_m . \quad (5.13)$$

The corresponding plots of the distribution of monomers mass density and its first three statistical moments are presented in Figure 5-7. The boundary effect persists up to a distance of $4R_g$.

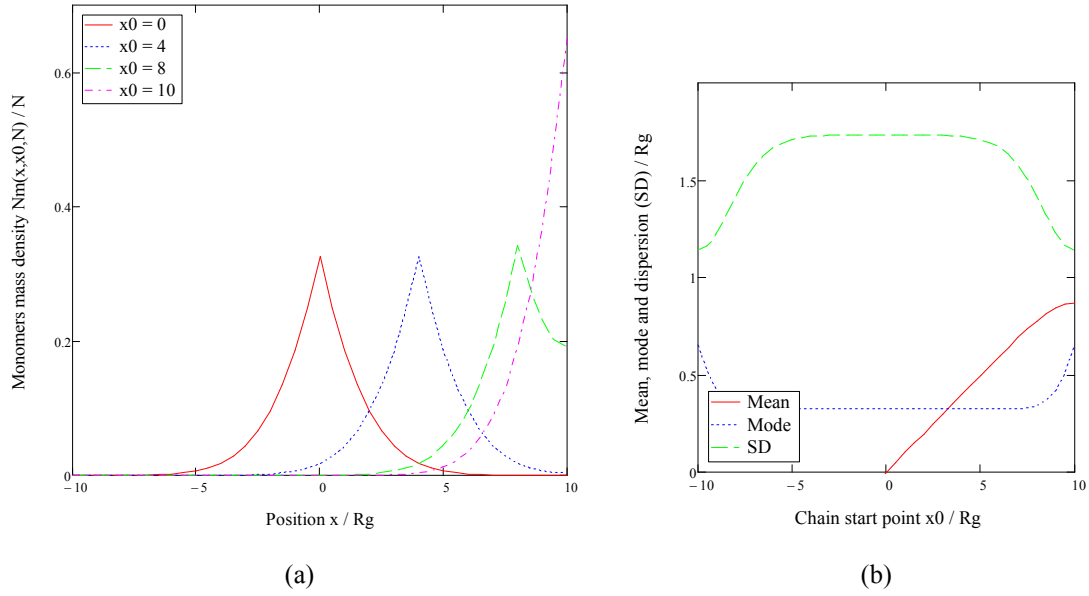


Figure 5-7: Distribution of chain monomers (or chain elements) mass density: (a) for several relative starting points x_0/R_g , and (b) central statistical moments of the distribution, versus the relative starting point x_0/R_g .

It is interesting to note that when the space between the walls is filled with chains of different starting points, and assuming free motion of the chains, the overall monomers mass density remains unaffected by the boundary, as shown by integrating the mass density Nm of Equation (5.13) over all possible chain starting points x_0

$$\int_{-R}^R Nm(x, x_0) dx_0 = 1. \quad (5.14)$$

The monomers mass density distribution can be depicted in two dimensions by assuming independent axes, parallel (Y) and perpendicular (X) to the walls. The chain is unbounded in the Y axis and therefore obeys the Gaussian distribution $G(x)$ from Equation (5.10), while in the X axis it is bounded by the walls and is given by the distribution $f(x)$ from Equation (5.9). The **bivariate distribution** $Nm2D$ of the monomers mass density is then

$$Nm2D(x, x_0, y, y_0, N) = \int_1^N f(x, x_0, n) \cdot G(y, y_0, n) dn_m. \quad (5.15)$$

Figure 5-8 shows a plot of this distribution. The chain is contracted (more condense) in the X direction, but not elongated in the Y direction.

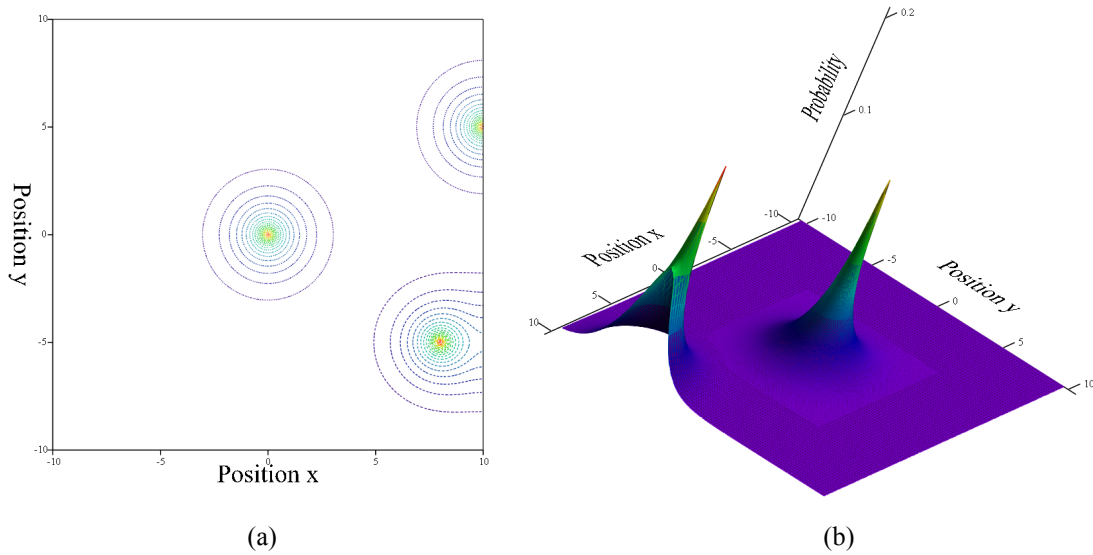


Figure 5-8: Bivariate distribution of the chain monomers mass density, in X (perpendicular to the walls) and Y (parallel to the walls), assuming independent X and Y: for chain relative starting points (a) $x_0/R_g = 0, 8$ and 10 , and (b) $x_0/R_g = 0$ and 9 .

The model developed in this section was expanded to real chains as well, using the asymmetric real chain distribution function of Equation (A.9). The results of the boundary effect are very similar to ideal chains.

To conclude, the boundary imposes folding of the chain back into the fiber, resulting in higher density of monomers and in a contracted chain conformation (in the direction perpendicular to the boundary). This contraction does not change the orientation of individual chain elements, and therefore its impact on elasticity is expected to be small.¹⁶

The boundary effect persists up to a distance of $\sim 5R_g$ from the fiber surface, much less than the value of $\sim 25R_g$ observed by the experiments analyzed in Section 5.1. Thus, the boundary effect does not provide a sufficient explanation, leading us to the analysis of the electrospinning effect on chain extension and orientation. Before that, we introduce in the next section an essential tool for this research – random walk simulation.

¹⁶ Conversely, stretching and compression during electrospinning enhance orientation of chain elements, as will be discussed later.

5.3 Random walk simulation tool

An ideal chain can be described by random walk (Appendix A), where each step represents a single monomer (or chain element). Random walk (RW) simulation can be an effective tool when the theoretical solution is too complex, when visualization of the behavior of a single chain is desired, or when applying complex boundary constraints and potential fields (e.g. a flow field).

RW simulation consists of generating a large enough sample of individual walks, each constructed from N successive unit-steps, and then collecting a distribution of a selected parameter (e.g. end-to-end distance) from the complete sample, and finding the statistical moments and other characteristic features of the distribution.

The **algorithm** developed for this research was implemented on Mathcad in one dimension, using the randomization function for two cases: a boundary effect problem (Figure 5-9(a)), and an extensional flow problem (Figure 5-9(b)). As shown, for the boundary effect problem, the probability of moving in either direction is the same and equal to 0.5. For the extensional flow problem, the probability of moving in either direction depends on the function $Pstep(x, a)$ of the position x and the flow field velocity gradient parameter a ¹⁷. When $Pstep > 0.5$, the probability to step in the negative direction is higher, while when $Pstep < 0.5$, the probability to step in the positive direction is higher.

$$\begin{array}{l} \text{step}(x) := \begin{cases} \text{sign}(\text{rnd}(1) - 0.5) & \text{if } |x| \neq R \\ -1 & \text{if } x = R \\ 1 & \text{if } x = -R \end{cases} \\ x_n \leftarrow x_{n-1} + \text{step}(x_{n-1}) \end{array} \quad \text{(a)}$$

$$\begin{array}{l} \text{step}(x) := \text{sign}(\text{rnd}(1) - Pstep(x, a)) \\ x_n \leftarrow x_{n-1} + \text{step}(x_{n-1}) \end{array} \quad \text{(b)}$$

Figure 5-9: Random walk procedure - chain end-to-end length x_n versus step n : (a) boundary effect problem, and (b) extensional flow problem, $Pstep(x, a)$ is the stepping probability at position x for a given velocity gradient parameter a . After N steps, the chain achieves its final end-to-end length x_N .

The probability distribution is generated by counting the frequency of occurrence of each possible chain length (or another selected parameter), and normalizing by the number of runs I .

¹⁷ Not to be confused with the chain element size a .

Examples of RW runs are provided in the following figures: Figure 5-10 shows two runs of a single chain – one reaches the boundary and the other does not – using a repulsive boundary condition. Figure 5-11 presents a sample of many chains ($I = 1,000$ chains), demonstrating how the chain lengths are bounded mainly by the closer (upper) boundary.

Figure 5-12 compares the chain lengths distribution obtained by RW to the theoretical solution of the diffusion equation from Equation (5.9), with a very good match. The number of RW runs needed to generate a “smooth” distribution is typically very high ($I = 50,000$ chains in this case), because the distribution contains all the pertinent statistical information on the sample, allowing further detailed statistical inference.

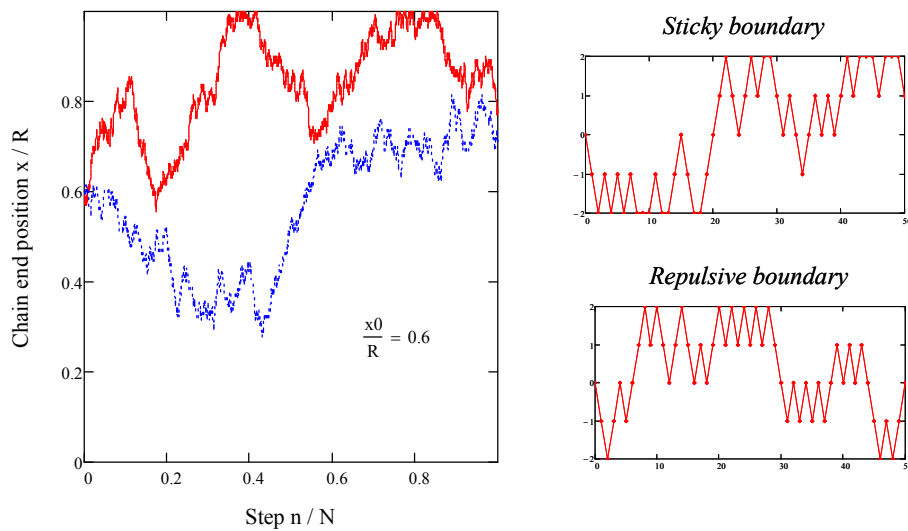


Figure 5-10: Single axis random walk simulation of single ideal chains, between two boundaries located at $x = \pm R$ (R is the fiber radius). The horizontal axis is the step number, and the vertical axis is the relative chain length x_n/R . Repulsive boundary is used.

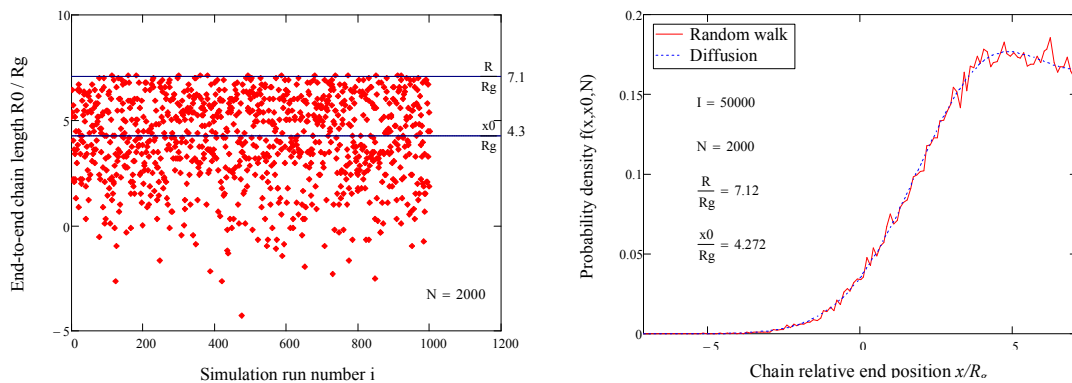


Figure 5-11: Random walk simulation sample of $I = 1,000$ chains: chain relative length R_0/R_g versus the run number i , for chains starting at $x_0/R_g = 4.3$. The chain lengths are bounded at positions $R/R_g = \pm 7.1$. The number of chain elements is $N = 2,000$.

Figure 5-12: Distribution of chain relative end position x/R_g , for chains starting at $x_0/R_g = 4.3$: random walk simulation sample of $I = 50,000$ chains, overlaid on the diffusion theoretical solution. The bounds are at positions $R/R_g = \pm 7.1$. The number of chain elements is $N = 2,000$.

The **applicability** of RW simulation to this research needs further discussion and justification, regarding the questions of chain type, dimensionality, walk type, and connectivity.

The questions of chain type (ideal or real) and dimensionality (one-dimensional or higher) were already addressed in Section 5.2, and the same rational in favor of ideal chain in one dimension applies to RW as well. In most cases relevant to this research, the behavior in different axes can be derived by separation of variables, without increasing the simulation dimensionality (see example in Figure 5-8).

The question of walk type (self-avoiding or not) is related to chain type. A self-avoiding walk results in a real chain (in good solvent), whose conformation is swollen compared to an ideal chain. External effects of the boundary and electrospinning act on the free conformation of the chain, whether swollen or not, and therefore the chain's initial conformation should be of second order. Moreover, as reasoned before, for concentrated solutions such as the solutions used in electrospinning, an ideal chain model is a good estimate.

The question of **connectivity** is somewhat more difficult [51]. In the RW approach used here, each step is completely independent of the preceding and succeeding steps, and therefore can be described as a Brownian motion of a single particle. But this is not the situation in a linear polymer chain, where each monomer (or chain element) is connected to two other monomers that may exert forces on it (Figure 5-13).

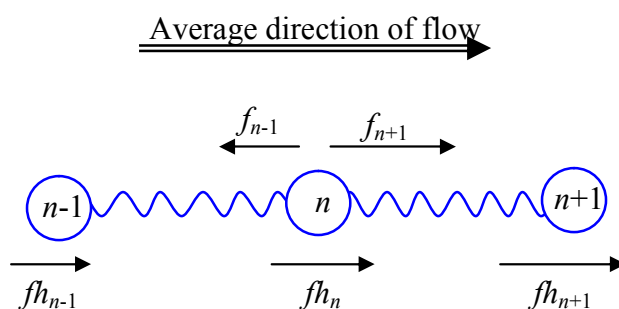


Figure 5-13: Forces acting on monomers $n-1$, n and $n+1$ due to hydrodynamic friction (fh_i) and interaction with adjacent monomers (f_i). This is an average scenario, since there is some (small) probability that monomer $n+1$ will be located upstream rather than downstream, and vice versa for monomer $n-1$.

In an ideal chain without an external potential field, the assumption of monomer independence is correct because the monomers are freely-jointed, and the elastic forces between them are the result of entropy changes (see Equations (2.10) and (2.11)). However, in an external potential field such as the extensional flow field of electrospinning, the hydrodynamic forces acting on the monomer and its neighbors result in additional inter-monomer forces.

Ignoring the elastic entropic forces that are already accounted for in the random walk, the forces acting on monomer n in the direction of the flow are

$$\sum f_n = fh_n + f_{n+1} - f_{n-1}, \quad (5.16)$$

where fh_n is the hydrodynamic force, and f_{n-1} and f_{n+1} are inter-monomers interaction forces. Due to the increasing velocity gradient in the direction of the flow, $fh_{n+1} > fh_n > fh_{n-1}$, and therefore $f_{n+1} > f_{n-1}$, resulting in $\sum f_n > fh_n$. This means that, on the average, the hydrodynamic force fh_n is a lower bound to the sum of forces acting on monomer n , and thus the question of connectivity is not critical for this application.

Similar reasoning applies to a polymer network subject to an extensional flow field (described later), by replacing monomers with subchains in the argument. However, when a nanofiber starts solidifying during electrospinning, the extensional forces gradually decrease, and connectivity becomes significant because the network resists the relaxation of subchains.

5.4 Single chain stretching under electrospinning shear flow

The concentrated solution used in electrospinning forms a polymer network (Sections 2.1 and 2.2). Although a single chain does not represent well a network, modeling it is worthwhile for deductive purposes, as it leads the way to the network model presented in Section 5.5. In this section we present a model and RW simulation for a single ideal chain immersed in solution, exposed to a strong extensional flow.¹⁸

Consider a one-dimensional random walk of step size Δ , subjected to a field potential U (Figure 5-14).

¹⁸ We use the terms shear flow (by de Gennes) and extensional flow to refer to the same type of flow that has a longitudinal velocity gradient.

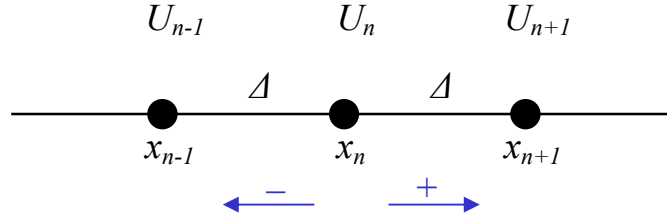


Figure 5-14: One-dimensional random walk: the walk can proceed from position x_n either in the (+) direction or in the (-) direction. The step size is Δ . U is the field potential.

From statistical mechanics it is known that the probability of a system having potential U_n is $(1/Q)e^{-U_n/k_B T}$, where Q is a partition function [52]. Then, the probability $P_+(n)$ to step from position x_n towards x_{n+1} , and the probability $P_-(n)$ to step from position x_n towards x_{n-1} , are given by

$$\begin{aligned} P_+(n) &\equiv P(n \rightarrow n+1) \sim e^{-\beta[U_{n+1}-U_n]} \\ P_-(n) &\equiv P(n \rightarrow n-1) \sim e^{-\beta[U_{n-1}-U_n]} \end{aligned} \quad (5.17)$$

$$\text{where } U_n \equiv U(x_n) \text{ and } \beta \equiv \frac{1}{k_B T}.$$

Using the potential derivative U_x we obtain

$$\frac{P_+(n)}{P_-(n)} = e^{-\beta[U_{n+1}-U_{n-1}]} = e^{-2\beta U_x \Delta} \quad \text{where } U_x \equiv \frac{\partial U_n}{\partial x}, \quad (5.18)$$

and since $P_+(n) + P_-(n) = 1$, we can derive the stepping probabilities $P_+(n)$ and $P_-(n)$

$$P_+(n) = \frac{1}{1 + e^{2\beta U_x \Delta}} \quad \text{and} \quad P_-(n) = \frac{e^{2\beta U_x \Delta}}{1 + e^{2\beta U_x \Delta}}. \quad (5.19)$$

We now define **global** and **local** coordinate systems with respect to the electrospinning jet (Figure 5-15). The global system X is of order ~ 1 cm, while the local system x is of order ~ 10 nm, an enormous ratio of 10^6 . Both X and x are positive downward and negative upward. The chain force center is defined as the location where the solvent velocity $V(X)$ equals the chain global velocity. The local velocity $v(x)$ is positive downward and negative upward, and therefore the friction forces $f_{hyd}(x)$ applied by the solvent on the chain, extend it so that about half of it is extended upward and half downward.

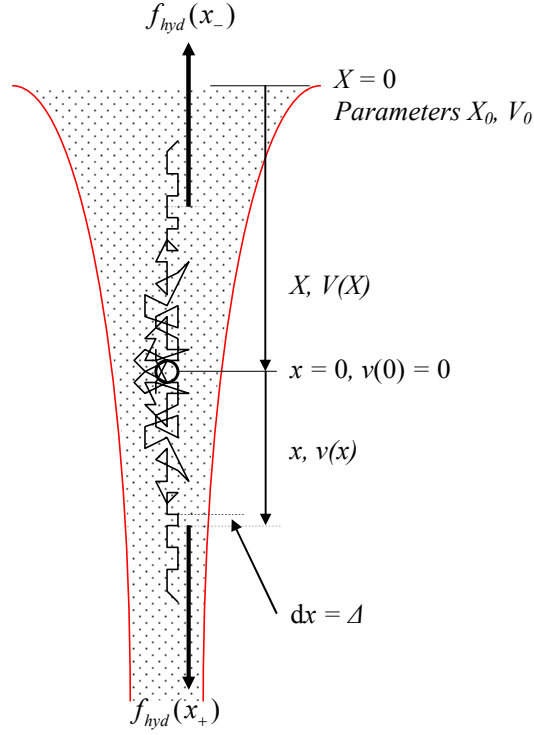


Figure 5-15: Global and local coordinate systems in the electrospinning jet: a single ideal chain immersed in solution and exposed to shear flow field. X is the global position of the chain force center. x is the local position of monomers with respect to the force center. $V(X)$ and $v(x)$ are global and local velocities respectively. $f_{hyd}(x)$ are hydrodynamic forces.

The local velocity $v(x)$ is derived from Equation (2.7)¹⁹

$$\begin{aligned}
 v(x) &= V(X+x) - V(X) \\
 &\cong V_0 \left(1 + \frac{X+x}{X_0} \right)^2 - V_0 \left(1 + \frac{X}{X_0} \right)^2 \cong V_0 \frac{x}{X_0} \left(2 + \frac{2X+x}{X_0} \right) \\
 &\cong \left[2 \frac{V_0}{X_0} \left(1 + \frac{X}{X_0} \right) \right] x \left\{ 1 + \left[2X_0 \left(1 + \frac{X}{X_0} \right) \right]^{-1} x \right\} = s_1 x + s_2 x^2,
 \end{aligned} \tag{5.20}$$

a quadratic function of the local position x , where s_1 is the linear velocity gradient, and s_2 is the quadratic velocity gradient. It means that monomers more distant from the chain force center experience higher friction forces, while at the center the force is zero. According to this equation, the local velocity is larger downward (larger X) than upward (smaller X), leading to $f_{hyd}(x_+) > f_{hyd}(x_-)$. For the same distance x from the force center, the difference between these two forces is very small, and therefore the chain force center is very close to the chain geometric center, confirming the assumption of symmetry.

¹⁹ Global velocity saturation is not included in this model.

The derivative U_x of the field potential is equal (with opposite sign) to the hydrodynamic force $f_{hyd}(x)$ acting on a monomer at local position x

$$U_x = -f_{hyd}(x) = -k\eta v(x)\Delta, \quad (5.21)$$

where η is the viscosity²⁰ and k a constant dimensionless factor. Substituting into Equation (5.19) and using $v(x)$ from Equation (5.20), a final expression for the **stepping probability** $P_+(x)$ is obtained after rearranging

$$P_+(x) = P_+(n) = \frac{1}{1 + e^{2\beta U_x \Delta}} = \frac{1}{1 + e^{-ax(1+bx)}}, \quad (5.22)$$

where the parameters a and b are given by

$$a = a(X) = 2\beta\Delta^2 k\eta s_1 = 4\beta\Delta^2 k\eta \frac{V_0}{X_0} \left(1 + \frac{X}{X_0}\right) \cong 4\beta\Delta^2 k\eta \frac{V_0 X}{X_0^2} \quad (5.23)$$

$$b = b(X) = \frac{s_2}{s_1} = \left[2X_0 \left(1 + \frac{X}{X_0}\right)\right]^{-1} \cong \frac{1}{2X} \quad \text{for } X \gg X_0.$$

The parameter a represents the velocity gradient s_1 multiplied by a constant; it is proportional to the global position X , and is fairly constant locally (in x system). The parameter b represents anisotropy between the upper part of the chain and the lower part. The term bx in Equation (5.22) is $bx = x/2X \ll 1$, and therefore can be ignored as soon as the jet exits the capillary. Thus, the chain force center closely coincides with the geometric center.

Using the relaxation time τ from Equation (2.3), the dimensionless expression ax in Equation (5.22) can be written by rearranging in the following way

$$ax = \frac{2ks_1\tau\lambda}{N} \sim s_1\tau \frac{\lambda}{N}, \quad (5.24)$$

where the relative elongation $\lambda = x/R_0 = x/(N^{1/2}\Delta)$ (ideal chain), and the scaling expression $s_1\tau$ is analogous to the expression $s\tau$ defined in Equation (2.4).

²⁰ Newtonian flow is assumed as an approximation, thereby the viscosity is constant.

We can use the values for X_0 and V_0 calculated in Section 2.2 for the experimental data reported by Han, in order to estimate the order of magnitude of s_1 , a and b . Taking $k = 10$ (assumption), $\eta = 1$ Pa·s (Figure 2-6), $\Delta = 1$ nm (a Kuhn segment), $\beta = 2.4 \cdot 10^{20} \text{ J}^{-1}$ ($T = 300\text{K}$), $X_0 = 0.18$ mm, $V_0 = 1$ mm/s, and $X = 100$ mm (a location on the jet): $\underline{s_1 = 6 \cdot 10^3 \text{ s}^{-1}}$, $\underline{a = 3 \cdot 10^7 \text{ m}^{-1}}$, $\underline{b = 5 \text{ m}^{-1}}$. Similarly for Bellan's data: $\underline{s_1 = 4 \cdot 10^4 \text{ s}^{-1}}$, $\underline{a = 2 \cdot 10^8 \text{ m}^{-1}}$, $\underline{b = 5 \text{ m}^{-1}}$. It is emphasized that these values are only a rough order of magnitude, and should be improved in the future. The values of the velocity gradient s_1 are of the same order of magnitude as the measurements by Reneker et al. [20-21] presented in Section 2.2.

In the language of the RW simulation, the values of the gradient parameters a and b should be converted to units of steps. Since one step was taken as $\Delta = 10^{-9}$ m, the rough order of magnitude values of a and b are

$$a \sim 10^{-1} \text{ to } 10^{-2} \text{ step}^{-1} \quad \text{and} \quad b \sim 10^{-8} \text{ to } 10^{-9} \text{ step}^{-1}. \quad (5.25)$$

Figure 5-16 illustrates the global effect on chain conformation: the chain is gradually stretched, until a phase transition (coil-stretch transition) occurs, leading to a new equilibrium where the chain is approaching full extension. This behavior was verified by the random walk simulation, to follow. In the transversal (radial) direction the chain contracts, as will be described in Section 5.6.

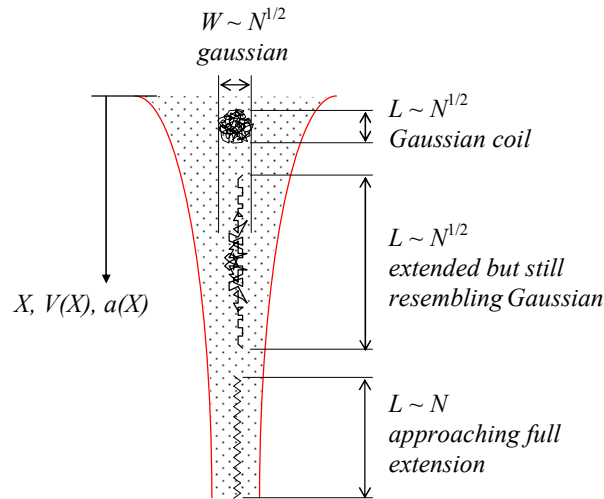


Figure 5-16: Illustration of the effect of the jet global coordinate X on chain conformation.

It is convenient to work with dimensionless variables in the simulation, by rewriting Equation (5.22) using the dimensionless relative position x/N (N the number of chain elements), and the dimensionless flow parameters $a \cdot N$ and $b \cdot N$

$$P_+\left(\frac{x}{N}\right) = \frac{1}{1 + e^{-aN\frac{x}{N}\left(1+bN\frac{x}{N}\right)}} \quad P_-\left(\frac{x}{N}\right) = 1 - P_+\left(\frac{x}{N}\right). \quad (5.26)$$

This equation is plotted in Figure 5-17 for the full range of the normalized position x/N , from -1 to +1, and is compared to the isotropic case ($b = 0$). The value of $a \cdot N$ was selected for a chain of $N = 300$ elements. A very high value of $b \cdot N$ was selected in order to demonstrate anisotropy; however, in view of Equation (5.25), this value is unrealistically high, confirming the assumption of isotropy.

Figure 5-18 shows two typical runs of a single chain – the walk ‘spends time’ around the starting point where the shear forces are small, and then gradually starts running off under increasing shear forces, achieving a substantial elongation of about half the full linear extension. The chain can randomly develop upstream (in the local system) or downstream. Figure 5-17 clarifies why this is happening – if the walk moves slightly downstream ($+x$), the probability of continuing downstream rises sharply; if the walk moves upstream, the stepping down probability decreases sharply while the stepping up probability rises sharply.

Only half of the chain is simulated (N is half the total number of chain elements), assuming, as reasoned before, that the other half balances the forces in the opposite direction. This assumption is correct since, except for the effect of anisotropy that is negligible, the chain has almost the same likelihood to develop up or down.

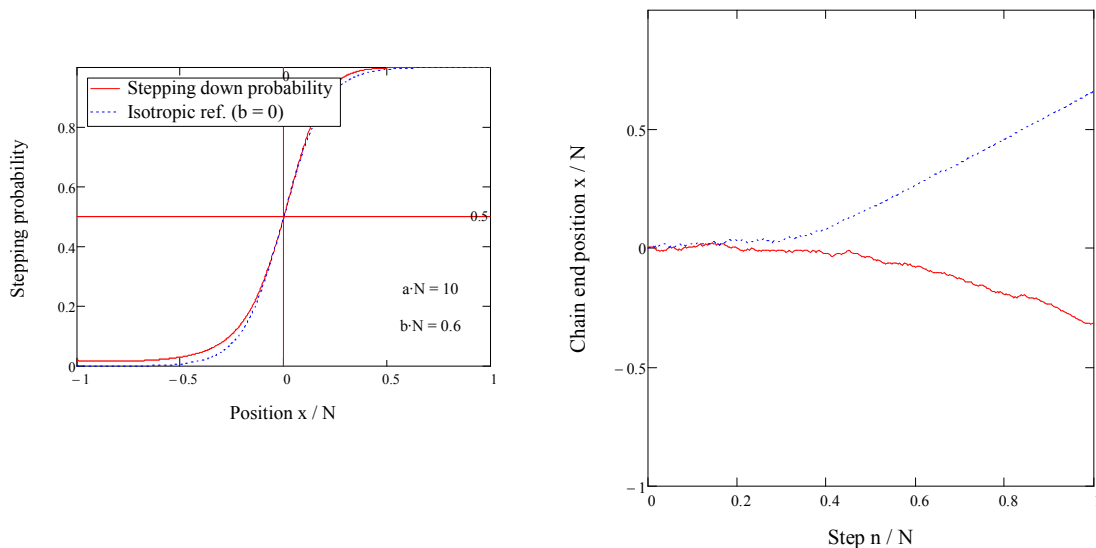


Figure 5-17: Probability to step downstream P_+ versus the relative local position x/N . $a \cdot N = 10$ step^{-1} and $b \cdot N = 0.6$ step^{-1} . Compared to the isotropic case ($b = 0$).

Figure 5-18: Two RW runs of a single chain in a flow field: chain relative local end position x/N is depicted versus the relative step number n/N . $a \cdot N = 10$ step^{-1} and $b \cdot N = 0.6$ step^{-1} .

By running the RW simulation for many chains ($I = 20,000$), a chain lengths (end-to-end) distribution was created (Figure 5-19(a)) for three different values of the normalized velocity gradient parameter $a \cdot N$. The distribution starts as Gaussian at zero velocity gradient ($a \cdot N = 0$), widens with increasing gradient ($a \cdot N = 5$), and finally separates into two groups (modes) at high gradient ($a \cdot N = 10$). The transition from a unimodal distribution to a bimodal distribution (i.e. from Gaussian-like coil to an almost fully-stretched chain) resembles a **phase transition**, similar to the coil-stretch transition described by de Gennes (Section 2.1) for a chain in a constant-gradient shear flow.

The coil-stretch transition occurrence relies on the magnitude of the velocity gradient, whose order of magnitude, according to the estimate in Equation (5.25), seems to be realistic for electrospinning. However, this estimate is quite rough, and further analytical and experimental work is required in order to validate this prediction.

The monomers (or chain elements) mass density distribution was generated by counting monomers occurrences of each chain, in each possible position, and then collating the results for all chains in the sample (Figure 5-19(b)). The results are normalized by the number of monomers N and the number of runs I . The monomers density distribution widens with increasing gradient, and tends to uniform distribution at large gradients.

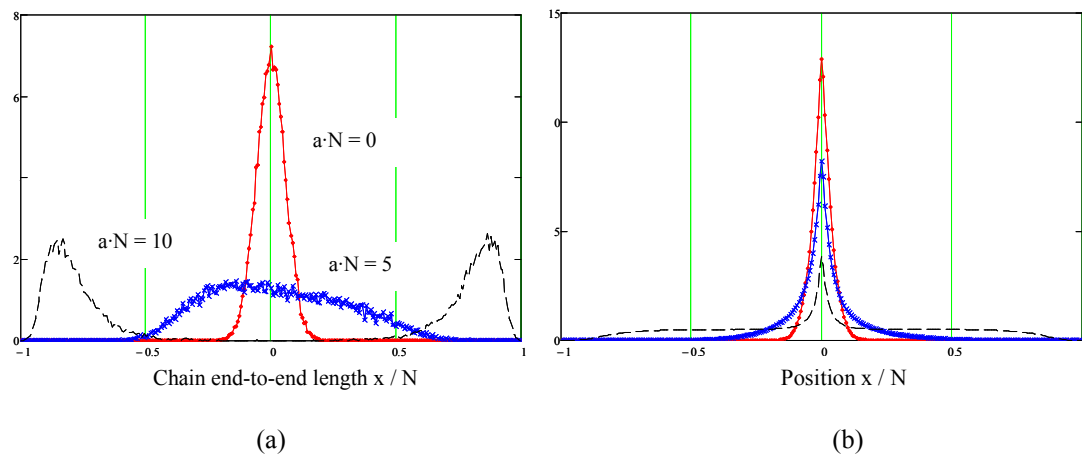


Figure 5-19: RW simulation of $I = 20,000$ chains: (a) Distribution of relative chain lengths x/N , and (b) average distribution of monomers (or chain elements) mass density, versus the relative local position x/N . $a = 0$ (Gaussian), 5 and 10 step^{-1} and $b = 0.6 \text{ step}^{-1}$; $N = 300$ chain elements.

A good “sensor” for detecting the onset of coil-stretch transition is the bimodal distance – the distance between the two separate peaks of the chain lengths distribution. This parameter was calculated from the distribution, along with the first five statistical moments, as a function of the normalized gradient parameter $a \cdot N$ (Figure 5-20). The bimodal distance clearly shows a sharp increase around the value of $a \cdot N = 5$, indicating a coil-stretch transition.

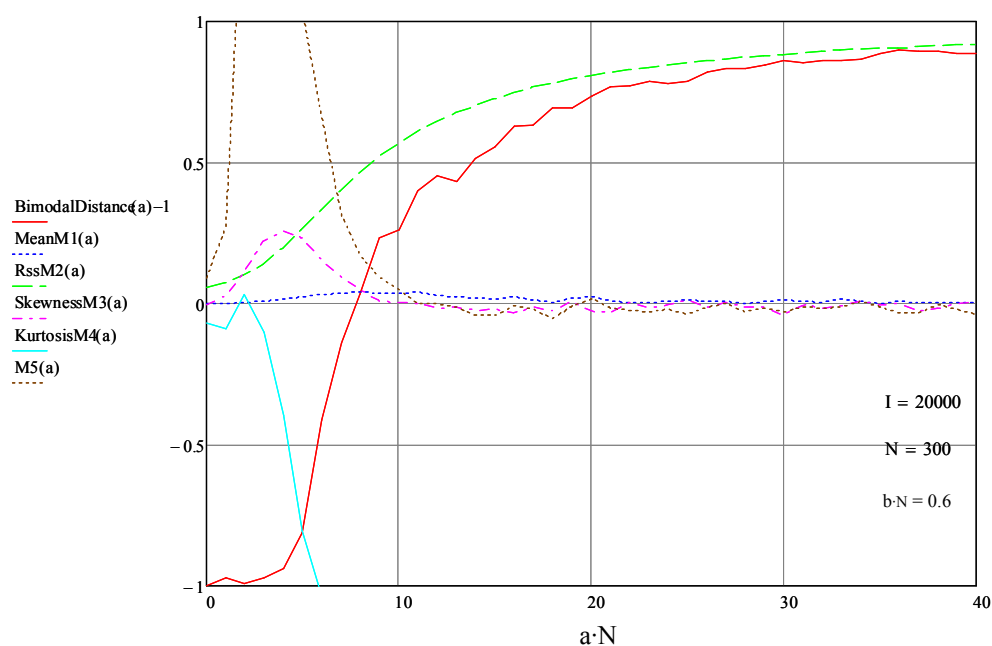


Figure 5-20: RW simulation of $I = 20,000$ chains - chain end-to-end lengths distribution: bimodal distance and the first five statistical moments, versus the flow normalized velocity gradient parameter $a \cdot N$. $N = 300$ chain elements.

The calculations of Figure 5-20 were repeated for five different values of the number of chain elements N , and the values of the gradient parameter a where coil-stretch transition occurred were recorded and plotted in Figure 5-21, demonstrating that phase transition for longer chains occurs at a lower gradient. In simulation terms, longer chains have more time (i.e. steps) to run away from the Gaussian-like conformation; in physical terms, longer chains are larger and more flexible (see Equation (2.11)), leading to higher forces on monomers distant from the force center.

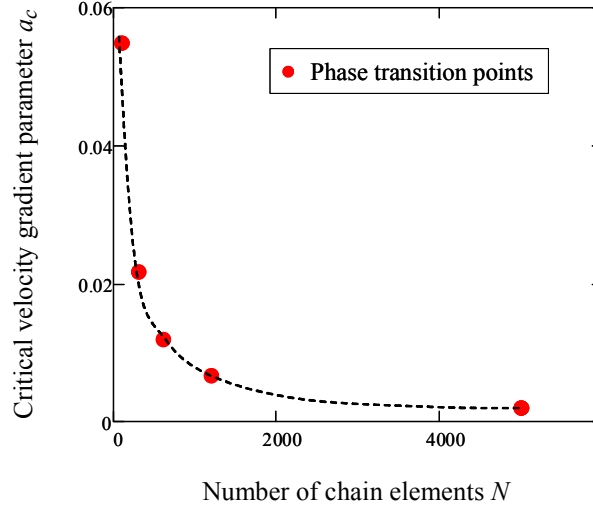


Figure 5-21: Phase transition of chain lengths (coil-stretch transition), expressed in terms of the flow critical velocity gradient parameter a_c , versus the number of chain elements N .

A power **scaling law**, correlating the critical velocity gradient parameter a_c to the number of chain elements N , can be derived from this plot by curve fitting:

$$a_c \cong 2.7 \cdot N^{-0.85}_{\text{step}^{-1}} \cong 2.7 \cdot 10^9 N^{-0.85}_{\text{m}^{-1}} \sim N^{-0.85}. \quad (5.27)$$

This scaling law is universal since it depends only on N , and does not depend on the process parameters k , η , X , X_0 and V_0 . Using Equation (5.23), the critical isotropic velocity gradient can be calculated by $s_{1c} = a_c / (2\beta A^2 k \eta) \sim N^{-0.85}$.

Remembering that the gradient parameter a is proportional to the global position X along the jet (Equation (5.23)), the plot in Figure 5-21 enables calculation of the critical global position X_c , where, for a given N , the coil-stretch transition occurs:

$$X_c = \frac{s_{1c} X_0^2}{2V_0} \sim N^{-0.85}. \quad (5.28)$$

This relation can be useful for planning a future experiment to detect coil-stretch transition in electrospinning. Assuming a viscosity of $\eta = 1$ Pa·s, the critical gradient $s_{1c} = 5.6 \cdot 10^6 N^{-0.85} \text{ s}^{-1}$. The critical global position can be estimated by using the values of X_0 and V_0 derived from experimental data: $X_c = 91 \cdot N^{-0.85} \text{ m}$ (Han's data); $X_c = 13 \cdot N^{-0.85} \text{ m}$ (Bellan's data). For sufficiently long chains, these numerical results

lead to X_c of order below 10 cm that is within the practical size range of electrospinning²¹.

An interesting relationship between the chain elongation, jet radius and chain size, can be obtain by realizing that the jet radius r_j can be written in terms of $a(X)$, using Equations (2.8) and (5.23):

$$r_j = \frac{r_0}{1 + X/X_0} = \frac{4\beta\Delta^2 k\eta \frac{V_0}{X_0} r_0}{a(X)} = \frac{const}{a(X)}. \quad (5.29)$$

The simulation was run as a function of r_j (i.e. of the gradient parameter a), for several values of number of chain elements N , and the mean-square values of the chain end-to-end length L and mass density Nm were obtained (Figure 5-22). Using bivariate power fitting in the region far enough from saturation, and converting N to $\sim R_g^2$, the following scaling law is obtained (in relative delta values),

$$\frac{\Delta L}{L_0} \equiv \frac{L - L_0}{L_0} \sim r_j^{-1.40} R_g^{0.62} \quad (5.30)$$

$$\frac{\Delta Nm}{Nm_0} \equiv \frac{Nm - Nm_0}{Nm_0} \sim r_j^{-1.48} R_g^{0.52},$$

reminiscent of the scaling laws developed in Section 5.1 (Equations (5.6) and (5.8)). L_0 and Nm_0 are the mean-square values of the chain length and mass density at zero gradient (Gaussian coil). Obviously, this law does not mean that the jet radius is the cause for chain elongation, for the true cause in this model is the flow velocity gradient, but rather it indicates that after fiber solidification there should be a quantitative relationship between fiber radius and chain conformation. This is an important distinction, because it implies that the relationship between nanofiber radius and elastic modulus, observed in experiments, may be circumstantial rather than causal, and that other common factors (e.g. velocity gradient) influence coincidentally both chain conformation and fiber radius.

²¹ It should be noted that for a polymer network (Section 5.5), the relevant variable is the number of elements N_s in a subchain, rather than the number of elements N in a chain, and since $N_s \ll N$ the critical global position X_c occurs further downstream (ignoring effects of connectivity between subchains).

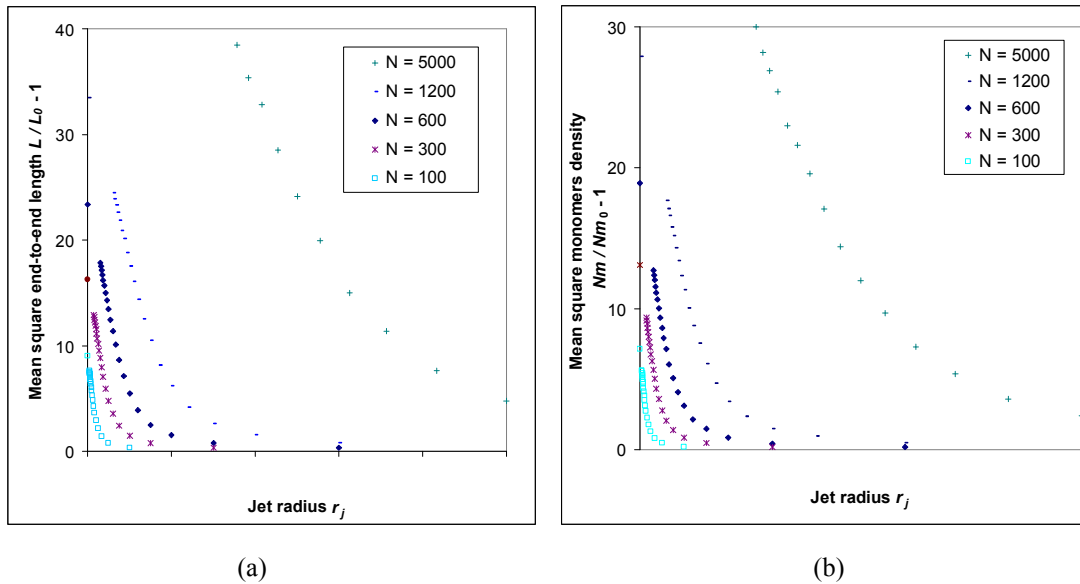


Figure 5-22: Mean-square chain values versus jet radius r_j , for several values of number of chain elements N : (a) relative delta chain lengths $\Delta L/L_0$, and (b) relative delta mass density $\Delta Nm/Nm_0$. RW simulation; each point on the plots represents a separate sample of many runs.

To summarize, a model and simulation were developed for single chain stretching under an extensional flow. The single chain model is not directly applicable to electrospinning; however it is instructive and useful as a starting point for the model of network stretching presented in Section 5.5.

The simulation clearly demonstrates substantial chain stretching that depends on the flow velocity gradient (growing with the global position along the jet), and that is more pronounced for longer chains. The chain stretching is not a linear process – above certain gradients it goes through a phase transition (coil-stretch transition), resulting in a sharp change in chain conformation from a Gaussian-like coil to an almost fully-stretched chain. This prediction relies on rough estimates of the velocity gradient, and therefore should be validated by further analytical and experimental work.

5.5 Network stretching under electrospinning shear flow

A polymer network is a mix of entangled chains in a semi-dilute solution, where the entanglement nodes are topological links between pairs of chains (Figure 2-12(a)), effectively dividing each chain into subchains. The average distance ξ between two topological links (mesh size), given by Equation (2.2), depends on the solution concentration. In solution, a subchain between two neighboring links has no interaction with other chains, and therefore its end-to-end length R_c conforms to $\Delta \cdot N^{\nu}$ (Δ is the step size or the chain element size). Equating this value with the mesh size we can calculate the number of elements N_s in a subchain:

$$\begin{aligned} N_s &= \left(\frac{\xi}{\Delta} \right)^{1/\nu} = \varphi^{1/(1-3\nu)} \\ &= N \left(\frac{c}{c^*} \right)^{1/(1-3\nu)} \quad \begin{array}{l} \text{ideal: } N \left(\frac{c}{c^*} \right)^{-2} \\ \text{real: } N \left(\frac{c}{c^*} \right)^{-5/4} \end{array} \end{aligned} \quad (5.31)$$

We can visualize the polymer network in an electrospinning jet as a continuous network flowing downstream, getting an endless feed of new subchains from the jet source (Figure 5-23). Each subchain is stretched individually, so that subchains farther downstream are more strongly elongated due to the higher flow velocity gradient. At the same time the subchains contract radially due to the combined effect of the extension in the longitudinal direction and the radial hydrodynamic forces.

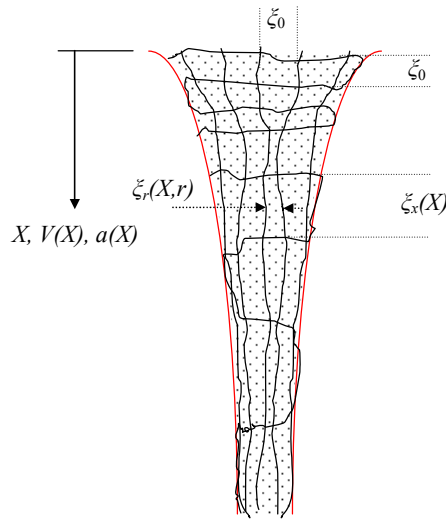


Figure 5-23: Polymer network immersed in a solution in a shear flow, extended longitudinally and contracted radially. ξ_0 is the initial subchain length (mesh size); $\xi_x(X)$ is the subchain global longitudinal length, $\xi_r(X,r)$ is the subchain global radial length. $a(X)$ is the flow velocity gradient.

For the purpose of the RW (random walk) simulation, we run each subchain individually as a single free chain in solution as done in Section 5.4, and in addition we account for the following factors:

- The initial elongation of the subchain, equal to the mesh size ξ , which, for a single free chain, was zero.
- The change in the velocity gradient parameter $a = a(X)$ along the jet, so that each subchain is exposed to the gradient corresponding to its global position X , while the gradient remains constant locally in the subchain.
- The slip of chains due to shifting of topological links under strong extensional forces, causing a dynamic increase in the number of elements N_s in a subchain.
- The saturation of the velocity upon solidification, resulting in the gradual disappearance of the gradient. At this stage the elastic forces tend to coil back the subchains not yet solidified, but the connectivity between the subchains, previously ignored (Section 5.3), becomes important.

The procedure used in the RW simulation is described in Figure 5-24. The calculation of the new factors in the simulation will now be detailed. We start with calculating the new term w (Figure 5-24 - box *a*). Assuming that the subchain is ideal (e.g. in a θ -solvent), and using Equation (2.11) realizing that $\xi_0 = R_0$, the elastic component $U_{x-elastic}$ of the potential derivative is given by

$$\begin{aligned}
 U_{x-elastic} = -f_{elastic} &= -\left(\frac{k_B T}{R_0^2}\right)\xi_0 = -\frac{1}{\beta\xi_0} \\
 &= -\frac{1}{\beta N_s^{1/2} \Delta} \quad \text{where} \quad \xi_0 = R_0 = N_s^{1/2} \Delta,
 \end{aligned}
 \tag{5.32}$$

and therefore the stepping probability downstream $P_+(x)$ of Equation (5.22) can be updated to

$$\begin{aligned}
 P_+(x) &= \frac{1}{1 + e^{2\beta U_x \Delta}} = \frac{1}{1 + e^{-w - ax(1+bx)}} \\
 \text{where } w &= -2\beta U_{x-elastic} \cdot \Delta = \frac{2}{N_s^{1/2}}.
 \end{aligned}
 \tag{5.33}$$

Next, the velocity gradient parameter a of Equation (5.23) is augmented by Δa (Figure 5-24 - box d), as a function of the global position X

$$\Delta a = \Delta a(X) = a(X + \xi(X)) - a(X) = K_a \xi(X) \quad (5.34)$$

where $K_a \equiv 4\beta\Delta^2 k\eta \frac{V_0}{X_0^2}$ is constant.

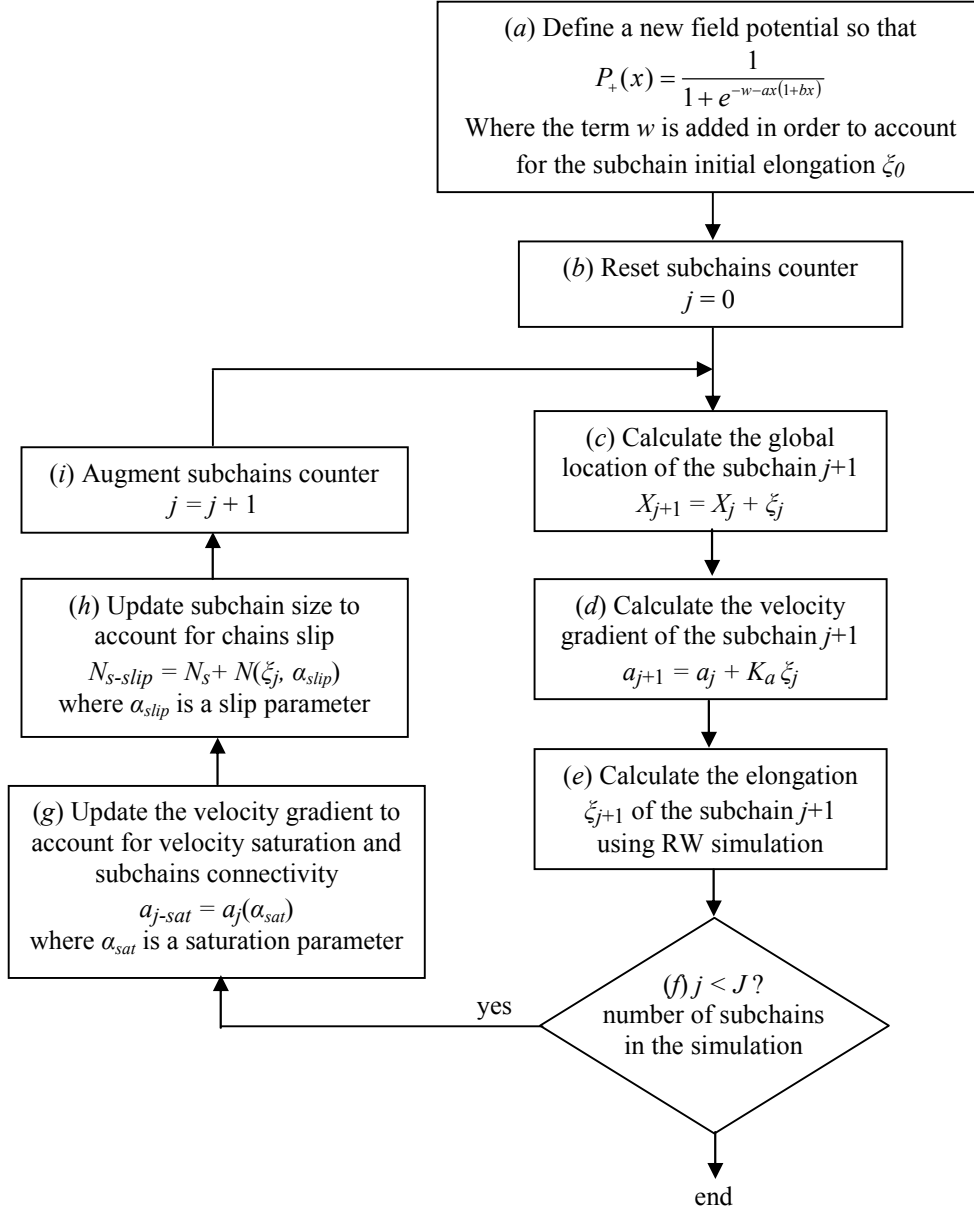


Figure 5-24: Procedure for RW simulation of a polymer network in a shear flow.

The value of the coefficient K_a can be estimated as a rough order of magnitude, using the same data as in Section 5.4 and Equation (5.25): $K_a = 3 \cdot 10^8 \text{ m}^{-2}$ (for Han's data), and a $K_a = 2 \cdot 10^9 \text{ m}^{-2}$ (for Bellan's), or, in the language of the RW simulation:

$$K_a \sim 10^{-9} \text{ to } 10^{-10} \text{ step}^{-2}. \quad (5.35)$$

Since a full representation of the complete jet should entail a huge number of subchains in the X direction, of order $100_{\text{mm}} / 1_{\text{nm/step}} / 10_{\text{steps/subchain}} \sim 10^7$ subchains, while we typically simulate only $\sim 10^3$ subchains, we accelerate the simulation by using a value of K_a that is 4 orders of magnitude higher, $K_{a\text{-accel}} \sim 10^{-5} \text{ to } 10^{-6} \text{ step}^{-2}$.

The anisotropy parameter b also changes along X , but it can be neglected due to its small value.

The value of the subchain elongation $\xi_j = \xi(X_j)$ is taken as the statistical mode (peak) of the end-to-end subchain lengths distribution (Figure 5-24 - box e).

The effect of velocity saturation on the velocity gradient parameter a (Figure 5-24 - box g) can be formulated by using a saturation parameter α_{sat}

$$a_{sat} = \frac{a}{\left[1 + \alpha_{sat} \cdot a^2\right]^2}, \quad (5.36)$$

and chain slipping (Figure 5-24 - box h) can be formulated as a function of relative chain elongation $\xi(X) / \xi_0$, by using a slip parameter α_{slip}

$$N_{s\text{-slip}} = N_s + \alpha_{slip} \cdot \left(\frac{\xi(X)}{\xi_0} - 1 \right) \quad \text{where} \quad \xi_0 = \sqrt{N_s}; \quad (5.37)$$

however, these are just examples, and the work on these effects is still in progress.

The simulation was run assuming concentration ratio $c / c^* = 4$, a typical value for electrospinning (Figure 2-7), leading to number of elements $N_s = N / 16$ in a subchain from Equation (5.31). Once N_s is calculated, the original N is no longer a relevant parameter in the simulation²². The results are presented in Figure 5-25, demonstrating the familiar phenomenon of **coil-stretch transition**, from relaxed subchains to almost fully stretched subchains. It is seen, especially in global coordinate, that the subchains reach strong elongation very rapidly.

²² The chain size N is still a relevant parameter physically, since it affects the solution rheological properties.

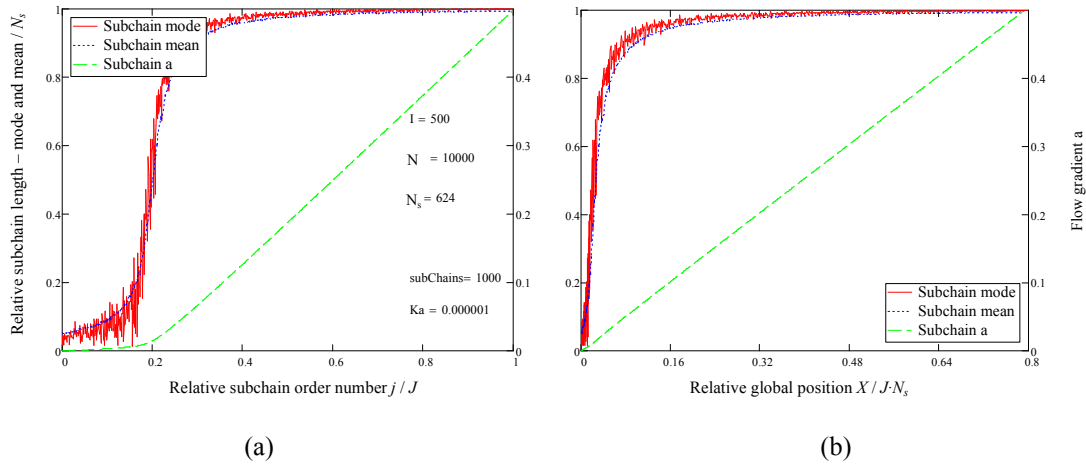


Figure 5-25: RW simulation of polymer network stretching in shear flow: subchain end-to-end lengths distribution - mode and mean normalized by the number of elements $N_s = 624$ in a subchain, versus (a) subchain order number j normalized by number of subchains $J = 1000$, and (b) global position X normalized by $J \cdot N_s$. Gradient parameter a is also plotted. The number of runs per subchain is $I = 500$.

The calculations of Figure 5-25 were repeated for several values of the number of elements N_s in a subchain and the coefficient K_a (i.e. $K_{a-accel}$), and the order numbers of subchains where coil-stretch transition first occurred were recorded (Figure 5-26). As expected, phase transition for longer subchains occurs earlier.

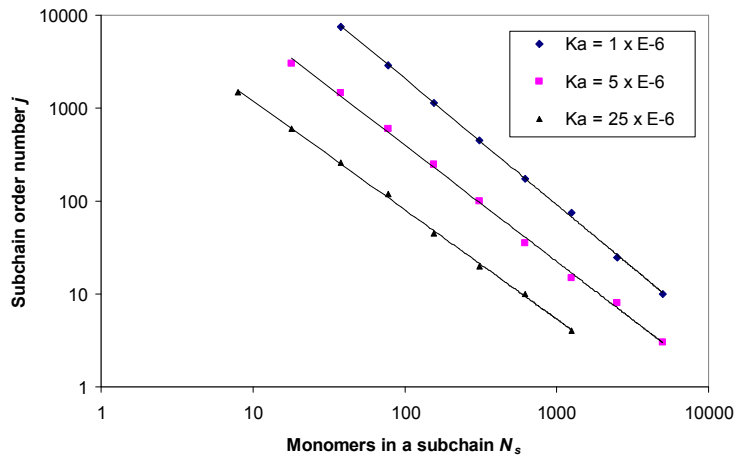


Figure 5-26: Phase transition of subchain length (coil-stretch transition), first occurring at subchain number j , versus the number of monomers (or chain elements) N_s in the subchain.

Bivariate power fitting of this plot yields an interesting scaling law for the first subchain to experience coil-stretch transition, j_{trans} :

$$j_{trans} = \frac{0.998}{K_a^{0.96} N_s^{1.26}} \cong \frac{1}{K_a N_s^{5/4}}. \quad (5.38)$$

The effects of velocity saturation and chains slipping are illustrated in Figure 5-27. Velocity saturation, when ignoring connectivity between subchains, causes

partial coiling back of the network. The peak subchain length in Figure 5-27(a) may be attributed to the nanofiber skin, which solidifies rapidly, while the decrease of the subchain length at farther subchains downstream (larger j) may be attributed to subchains inside the nanofiber core, which are still in solution state and have enough time to relax (at least partially). Chain slipping increases the subchain ultimate length, as shown in Figure 5-27(b).

To avoid coiling back, the simulation can take into consideration connectivity between subchains by augmenting the parameter w of Equation (5.33) as a function of the subchain elongation $\xi(X)$, thereby retaining the elongation and avoiding relaxation.

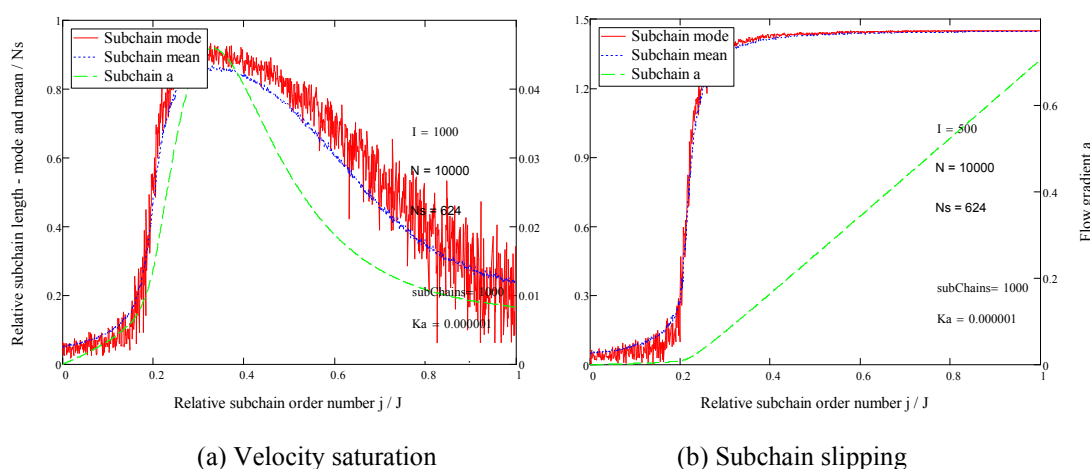


Figure 5-27: RW simulation of polymer network stretching in shear flow: (a) effect of velocity saturation, without connectivity, $\alpha_{sat} = 50$; and (b) effect of subchain slipping, $\alpha_{slip} = 8$.

To summarize, a model and simulation were developed for network stretching under an extensional flow. Similar phenomenon of coil-stretch transition, as in the single chain model, was observed. The dependence on the number of elements in a subchain and on the flow velocity gradient was also observed. The effects of subchains slipping and of velocity saturation need further research.

5.6 Transversal contraction due to electrospinning stretching

Another effect related to electrospinning is the radial contraction of chains that, together with axial stretching, change the orientation of chain links (chain elements). Chain contraction is caused by two different mechanisms: hydrodynamic forces due to a radial velocity gradient, compressing the chain towards the fiber center; and stretching in the longitudinal direction, leading to contraction in the radial direction. Unlike stretching, the potential field in the radial direction due to hydrodynamic forces must take into account the monomer excluded volume (Equation (A.7)), which,

when penetrated, exerts very high repulsion forces not considered in an entropic chain.

We begin with rewriting the one-dimensional Equations (5.17), (5.18) and (5.19) for the multi-dimensional case. Given a unit direction vector \vec{q} , the stepping probability $P_{\vec{q}}$ in the direction of \vec{q} , as a function of the derivative of the potential U , is

$$P_{\vec{q}} = \frac{e^{-\beta\vec{q}\frac{\partial U}{\partial\vec{q}}}}{\sum_{\vec{q}} e^{-\beta\vec{q}\frac{\partial U}{\partial\vec{q}}}} \quad \text{where} \quad \sum_{\vec{q}} P_{\vec{q}} = 1. \quad (5.39)$$

In two axes, x (axial) and r (radial), we have

$$P_{\pm x} = e^{\mp\beta U_x \Delta} / Q \quad \text{and} \quad P_{\pm r} = e^{\mp\beta U_r \Delta} / Q$$

where $Q = 2[\cosh(\beta U_x \Delta) + \cosh(\beta U_r \Delta)]$ (5.40)

$$U_x \equiv \frac{\partial U}{\partial x} \quad \text{and} \quad U_r \equiv \frac{\partial U}{\partial r}.$$

Applying a similar technique as before, and assuming the same factor k in direction r as in x , the derivative U_r of the potential is obtained by using Equation (2.7) (note the positive sign)

$$U_r = -f_{hyd}(r) = -k\eta v(r)\Delta \cong k\eta\Delta \frac{V_0}{X_0} \left(1 + \frac{X}{X_0}\right) r, \quad (5.41)$$

where r is the local radial direction, referenced to the chain's force center. This equation holds as long as the excluded volume is not penetrated.

We now rewrite Equation (5.40) in the following form (the negligible anisotropy factor bx is ignored). Note that with the assumption that the factor k is the same in both directions, the same velocity gradient parameter a from Equation (5.23) is applicable to both the axial and radial components but with a different pre-factor:

$$P_{\pm x} = e^{\pm\frac{1}{2}ax} / Q \quad \text{and} \quad P_{\pm r} = e^{\mp\frac{1}{4}ar} / Q$$

where $Q \equiv 2[\cosh(\frac{1}{2}ax) + \cosh(\frac{1}{4}ar)]$. (5.42)

In the case of $U_r = 0$ the radial hydrodynamic forces are ignored, and we isolate the effect of radial contraction due to axial stretching. Equation (5.40) then simplifies to

$$P_{\pm x} = e^{\pm \frac{1}{2}ax} / Q \quad \text{and} \quad P_r \equiv P_{\pm r} = 1/Q \quad (5.43)$$

where $Q \equiv 4 \cosh^2(\frac{1}{4}ax)$.

This equation allows separation of variables in that P_r is not dependent on the potential derivative in the r direction. At any local position x along the chain, P_r is constant and equal in both directions of r . Up to a certain contraction ratio the chain is still Gaussian-like in the radial direction, and the mean-square radial size $R_r(x)$ of the chain is approximately proportional to the stepping probability (normal distribution). Thus, we can calculate the contraction ratio CR as

$$CR \cong \frac{R_r(x=0)}{R_r(x)} = \frac{P_r(x=0)}{P_r(x)} = \frac{1/4}{1/Q} = \cosh^2(\frac{1}{4}ax). \quad (5.44)$$

The result is plotted in Figure 5-28, showing rapid contraction for large x and a .

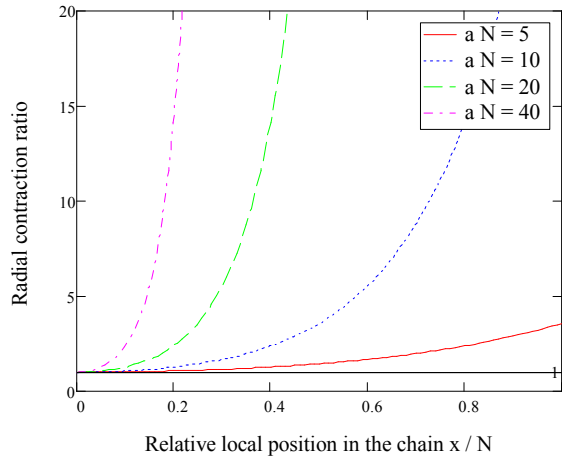


Figure 5-28: Radial contraction ratio CR due to axial stretching, versus the local position along the chain x/N , for several values of the flow normalized velocity gradient parameter $a \cdot N$. Applies to Gaussian-like contraction.

A more complete contraction analysis can be achieved by running the RW simulation in the r axis using Equation (5.43), remembering to skip steps that are related to the x direction. This task requires further simulation work. A preliminary view of the influencing factors can be obtained by plotting the ratio of P_{-r} from Equation (5.43) to P_{-r} from Equation (5.42), providing the normalized contribution of axial stretching to radial contraction (Figure 5-29). The smaller the coordinates ratio

x/r and the higher the velocity gradient term $a \cdot x$, the more dominant the hydrodynamic compression is in contracting the chain; otherwise, the stretching radial effect becomes dominant.

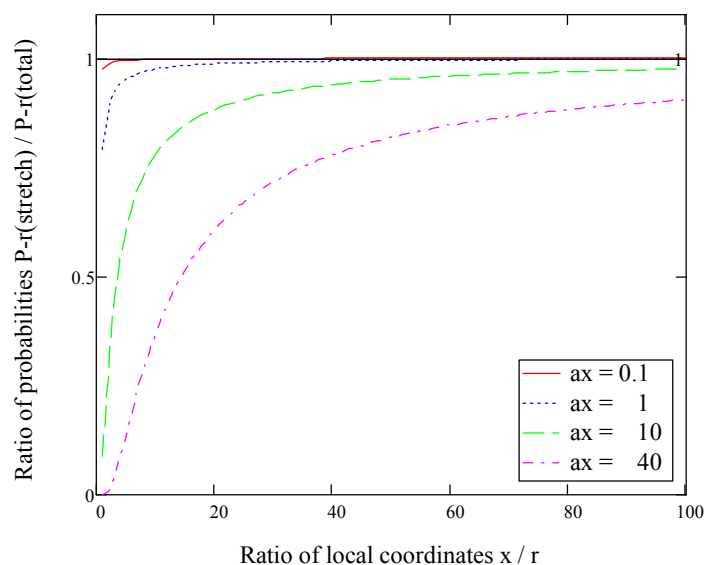


Figure 5-29: Probability P_{-r} to step radially towards the chain center: ratio of stretching effect $P_{-r}(\text{stretch})$ to total effect $P_{-r}(\text{total})$, versus the ratio of local coordinates x/r .

The stretching-contraction model of Equation (5.43) can be used to estimate the probability distribution of the **orientation** of individual links (elements) of the chain, an important parameter affecting elasticity. The RW model uses a Cartesian lattice, and thereby the links are either horizontal (radial) or vertical (axial). We therefore need to define a continuous probability density function $P(\varphi_o)$ for intermediate angles φ_o (with respect to the jet axis), such as the approximation given by

$$P(\varphi_o) \cong \frac{e^{\frac{1}{2}ax \cdot \sin \varphi_o}}{Q} \quad \text{where} \quad Q \equiv \int_{-\pi/2}^{\pi/2} e^{\frac{1}{2}ax \cdot \sin \varphi_o} d\varphi_o . \quad (5.45)$$

Note that the term $4 \cosh^2(\frac{1}{4}ax)$ from Equation (5.43) appears in both the numerator and denominator, and was therefore eliminated. The additional term $\sin \varphi_o$ ensures that the numerator shall converge proportionally to $\sim P_{\pm x}$ and $\sim P_r$ of Equation (5.43) at $\varphi_o = \pm 90^\circ$ and $\varphi_o = 0^\circ$ respectively. This definition provides an approximate probability distribution function $P(\varphi_o)$ of chain link orientation angles, as a function of the flow velocity gradient parameter a and the local axial position x along the chain.

The distribution is plotted in Figure 5-30 for several values of $a \cdot x$, demonstrating the significant influence of axial stretching on the orientation of individual chain links. At higher a and x , the chain links have higher probability to be

aligned with the longitudinal axis (i.e. the jet direction), or, in other words, the degree of orientation is higher. This effect saturates at high values of $a \cdot x$, converging to a full longitudinal orientation.

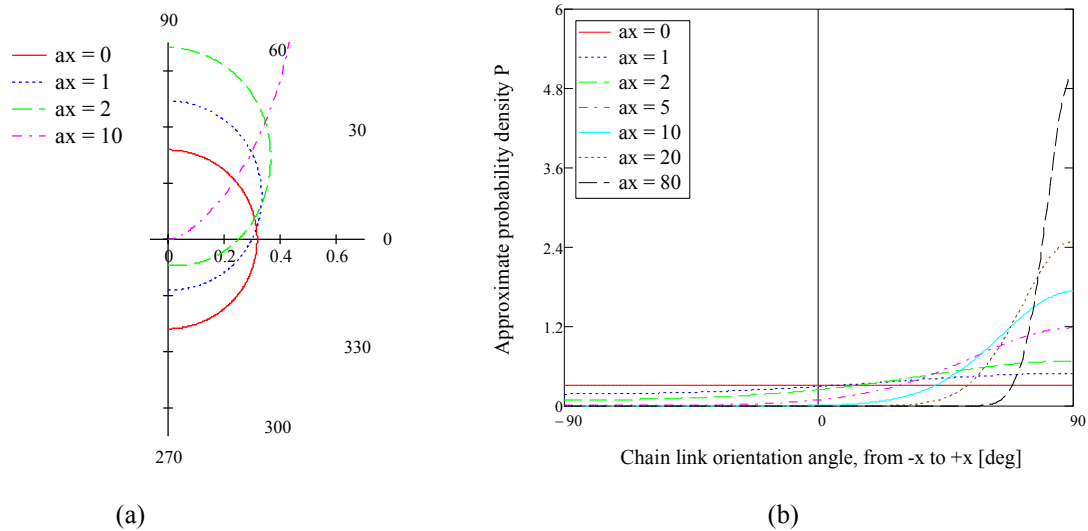


Figure 5-30: Approximate probability density function $P(\varphi_o)$ versus the orientation angle φ_o of the chain link, for several values of $a \cdot x$ (a velocity gradient, x local axial position): (a) polar coordinates ($P(\varphi_o)$ is the radius), and (b) Cartesian coordinates.

The mean orientation angle φ_o is depicted as a function of $(a \cdot x)^{-1}$ in Figure 5-31, remembering from Equation (5.29) that r_j is inversely proportional to the gradient parameter a . This result predicts that there is a crossover radius, below which the degree of orientation should increase sharply, approaching full orientation at 90° . The experiments of Figure 2-23 show only moderate dependence of the orientation on the fiber radius, suggesting that they may have not reached the crossover radius.

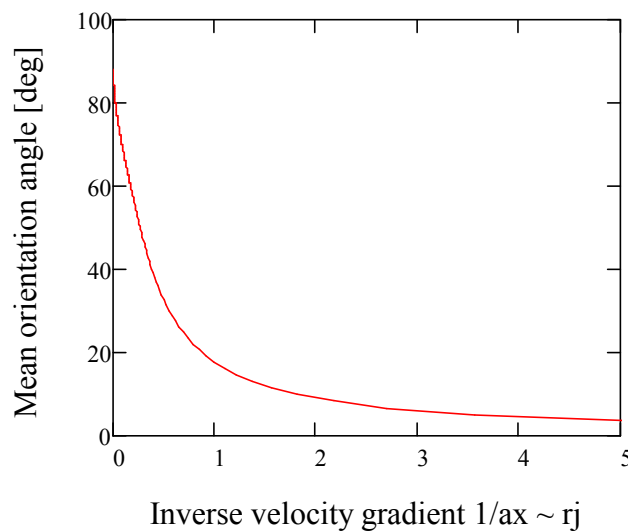


Figure 5-31: Mean orientation angle φ_o versus the inverse velocity gradient term $a \cdot x$ (proportional to the jet radius r_j).

To summarize, radial chain contraction is caused by radial hydrodynamic forces and by the transversal effect of stretching. The preliminary model provides an estimate for chain contraction and the degree of orientation due to stretching, showing a distinct crossover at a certain velocity gradient. Similar behavior is expected for a polymer network as well. The contraction model should be expanded to account for the effect of monomers excluded volume.

5.7 Preliminary conclusions

The preliminary study focused on theoretical evaluation of the changes in chain conformation and orientation due to the nanofiber boundary effect and the stretching during electrospinning.

Theoretical and empirical power scaling laws were formulated, correlating the elastic moduli to fiber radius and polymer molecular weight (chain size, expressed as gyration radius R_g). The available data shows a distinct crossover at fiber radius of $\sim 25R_g$, below which the elastic moduli rise sharply.

A theoretical model for the nanofiber boundary effect on chain conformation has shown that chains closer than $\sim 5R_g$ to the boundary are contracted transversely, but their individual elements are not changing orientation. The boundary effect is not sufficient to justify the experimental results, turning our focus to the stretching and transversal contraction effects of electrospinning.

A one-dimensional random walk simulation tool was developed and validated. The applicability of random walk to this research, regarding the questions of chain type, dimensionality, walk type, and connectivity, was analyzed and justified.

Single chain and polymer network stretching during electrospinning were simulated, including preliminary incorporation of the effects of evaporation and relaxation. The magnitude of stretching increases gradually with the jet velocity gradient and the number of chain elements, to a point where a phase transition (coil-stretch transition) to an almost fully-stretched chain occurs.

A theoretical model for the transversal (radial) chain contraction due to both axial stretching and radial hydrodynamic forces has shown that the degree of chain orientation rises sharply above a certain velocity gradient.

The theoretical work will be expanded during this research, and more attention will be given to correlating chain orientation to the nanofiber elasticity, and to experimental validation.

Appendix A. Polymer physics – single chain static conformations

The physics of polymers deals with the static and dynamic conformation of polymer molecules in various states, and is described in books by notable researchers: Flory *Polymer Chemistry* [36], De Gennes *Scaling concepts in polymer physics* [1], Rubinstein *Polymer physics* [34], and Grosberg *Statistical physics of macromolecules* [35]. The following review provides the basic concepts of polymer physics and is based mainly on these references.

A **polymer** is a very large molecule or macromolecule, consisting of many repeating units (monomers) joined by covalent chemical bonds (Figure A-1). A polymer molecule may have branches of various formations, or can be a long linear chain. For simplicity, the following review deals with linear chains.

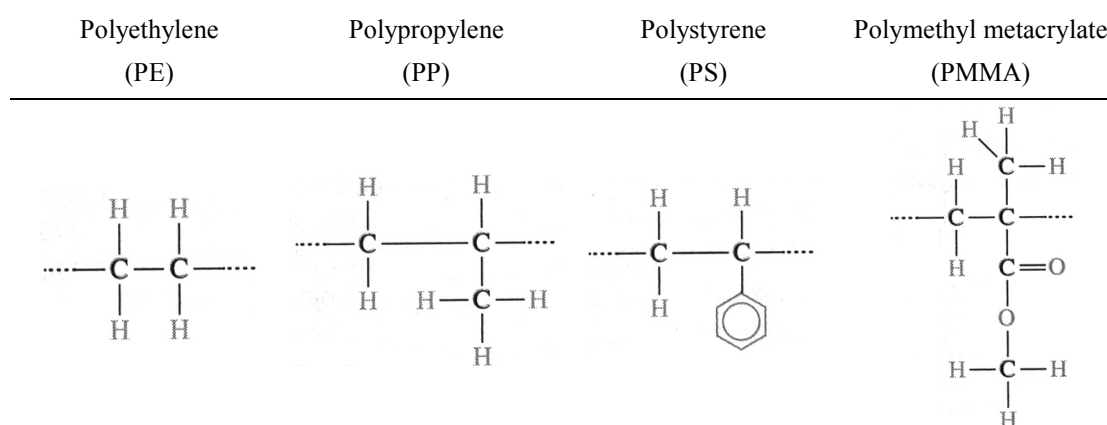


Figure A-1: Examples of synthetic polymers and their repeating units (monomers). Based on [53].

The number of monomers N in a single macromolecule, called the polymer degree of polymerization, can reach the order of 10^5 , with molecular weights ranging from 10^4 to 10^6 g/mol. A monomer may consist of several backbone atoms (usually carbon), with two hydrogen atoms bonded to each carbon atom. Some of the hydrogen atoms are replaced by side groups, such as the CH_3 group (methyl) in PP and the Benzene ring in PS (Figure A-1), affecting the polymer properties. The number of backbone atoms in a single macromolecule is designated as n .

Polymer chains are flexible, and therefore can adopt varied conformations of statistical nature, occupying a volume much larger than the volume of their constituents. **Flexibility** is due to the variation in the torsion (rotation) angle φ of the carbon-to-carbon (C-C) covalent bonds (Figure A-2). While the bond tetrahedral angle θ is almost constant at 68° , the torsion angle may be in one of three different states – *Gauche*₋, *Gauche*₊, and *Trans* (rigid), depending on the energy difference $\Delta\varepsilon$

between these states, the energy barrier ΔE between them, and the thermal energy $k_B T$ (k_B - Boltzmann constant, T - temperature). $\Delta \varepsilon$ determines the static flexibility, while ΔE the dynamic flexibility, or the characteristic time for transition between the states.

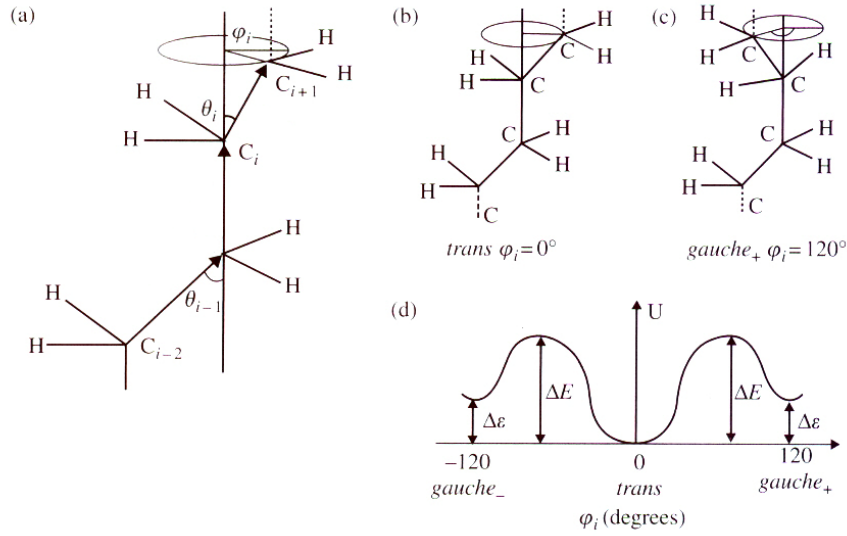


Figure A-2: Bond flexibility due to variation in torsion angles: (a) Tetrahedral angle θ and torsion angle φ for a sequence of three backbone bonds, (b) Trans state, (c) Gauche₊ state, and (d) torsion angle energies [34].

At a small scale, segments of the chain may be rigid, with a characteristic length l_p , the persistence length, of

$$l_p = l e^{\Delta \varepsilon / k_B T}, \quad (\text{A.1})$$

where l is the length of the C-C bond, equal to 1.54 Å [1]. Assuming the conditions for flexibility exist, the persistence length may be assumed as the monomer size. At a larger scale than l_p , the chain may still be considered as flexible. Thus, even though the chain depends locally on its chemical properties, globally it depends on physical observable properties such as chain length and concentration.

A polymer chain often possesses the property of self-similarity, or **scale invariance**, up to a certain degree of magnification (Figure A-3). This property enables universal scaling laws, such as the power dependence of the chain average coil size on the number of monomers, as shown in Equations (A.4) and (A.8).

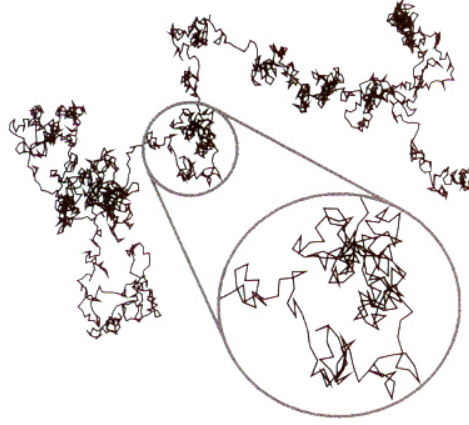


Figure A-3: Computer simulation of a polymer chain, showing the self-similarity or scale invariance of the chain [34].

When the interactions between distant monomers in a chain are ignored (or balanced), the polymer chain is called an **ideal chain**. The mean-square end-to-end distance R_0 of a linear ideal chain is

$$\langle R_0^2 \rangle \cong C_\infty n l^2 = N_k l_k^2 \equiv N a^2, \quad \text{and therefore} \quad R_0 = a N^{1/2}, \quad (\text{A.2})$$

where n is the number backbone bonds, l the bond length, and C_∞ Flory's characteristic ratio for long chains, which accounts for the fact that adjacent atoms are not freely jointed but are rather bound to the possible states of the bond angles [34]. The values of the dimensionless factor C_∞ range from 5 to 10 for typical long chains.

The length l_k is defined as the **Kuhn segment** (also called Kuhn length or Kuhn monomer), and the number of Kuhn segments in the chain is N_k , thus rendering the chain as freely jointed with the same end-to-end distance. The size of a Kuhn segment is from 0.8 to 1.8 nm for typical polymers. The Kuhn segment approach takes into account the details of the local restricted bond angles and the steric hindrance (restrictive effect of polymer side groups), and is therefore more accurate and measurable than the persistence length approach [35].

For simplicity, as shown in the rightmost expression of Equation (A.2), we define a as the length of a reference rigid element, and N as the number of such elements in the chain [34]

$$a \equiv l_k = \frac{\langle R_0^2 \rangle}{R_{\max}} = \frac{C_\infty l}{\cos(\theta/2)} \cong 1.17 C_\infty \cdot l \quad (\text{A.3})$$

$$N \equiv N_k = \frac{R_{\max}^2}{\langle R_0^2 \rangle} = \frac{n \cos^2(\theta/2)}{C_\infty} \cong \frac{0.69}{C_\infty} n,$$

where $R_{\max} = nl \cos(\theta/2)$ is the fully extended length of the chain. We shall use different names for a – chain element, **Kuhn segment**, Kuhn monomer, or just monomer – but they all designate the smallest rigid element of the chain, and similarly for N .

The mean-square radius of gyration R_g of a linear ideal chain is defined as the averaged square distance from all monomers to the polymer center of mass, and is a convenient measure for the polymer occupying size

$$\langle R_g^2 \rangle = Na^2 / 6, \quad \text{and therefore} \quad R_g = \frac{a}{\sqrt{6}} N^{1/2}. \quad (\text{A.4})$$

As an example, for a polystyrene chain of $n = 40,000$ backbone C-C bonds, with $C_\infty = 9.5$, $l = 1.54 \text{ \AA}$, and $\theta = 68^\circ$ [34], we obtain: $a = 1.76 \text{ nm}$, $N = 2894$, $R_0 = 94.7 \text{ nm}$ and $R_g = 38.7 \text{ nm}$. In comparison, $R_{\max} = 6160 \text{ nm}$, much larger than R_0 , and, if we ignore the correction factor C_∞ , $R_0(C_\infty=1) = 30.8 \text{ nm}$, much smaller than R_0 . Thus, the chain resembles a coil rather than a linear line. The relative sizes are illustrated in Figure A-4, where \vec{R} is the end-to-end distance.

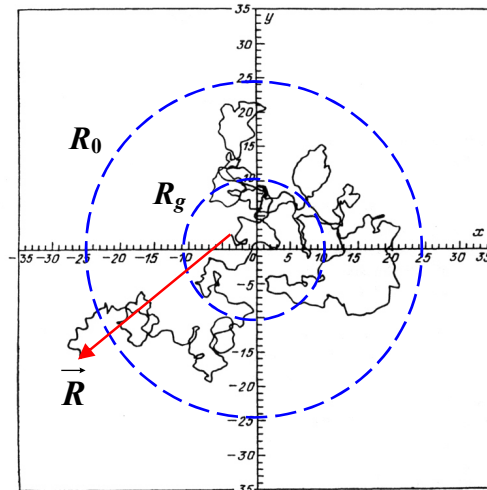


Figure A-4: Computer simulation of coil conformation of a single ideal chain of 626 freely jointed segments of unit length. Adapted from [35].

The statistical distribution of end-to-end distances r (in three dimensions) of a linear ideal chain, can be obtained by N steps of **random walk** (RW) of fixed step length a , where each step is independent and of the same probability in all directions. Random walk on a Cartesian lattice can describe each possible chain conformation of a freely jointed chain, and therefore its statistics applies to long ideal chains. The result is a Gaussian distribution $P(r, N)$ of the three-dimensional end-to-end distance [34]:

$$P(r, N) = \left(\frac{3}{2\pi R_0^2} \right)^{3/2} \exp\left(-\frac{3r^2}{2R_0^2} \right) \quad \text{where } R_0^2 = Na^2. \quad (\text{A.5})$$

Equation (A.5) can also be obtained by solving the diffusion equation (or Schrödinger equation) (references [1, 35])

$$\frac{\partial P}{\partial N} = \frac{a^2}{6} \frac{\partial^2 P}{\partial r^2} - \frac{U(r)}{k_B T} P, \quad (\text{A.6})$$

where the time t is replaced by the step number N , and the field potential $U(r)$ is nullified. Equation (A.6) has the benefit of providing an analytical solution for solvable boundary conditions and for a known (or estimated) mean field potential. In other cases, random walk simulations are useful, and were extensively used in the preliminary work of this research.

A **real chain** in a solution²³ has interactions between distant monomers, expressed as repulsion between monomers, leading to swelling of the coil. At the same time, the elastic entropic forces of Equation (2.10) tend to draw the coil back to its Gaussian conformation. Additionally, monomer-solvent interaction forces are effective. When the attraction forces balance the effect of repulsion, the chain is nearly ideal, and the solvent is termed θ -solvent. A similar situation happens for chains in a polymer melt (a concentrated solution), where the repulsion forces due to interactions within the chain are balanced by the repulsion forces due to interactions with other chains in the melt.

If the repulsion is stronger than the attraction (good solvent), the chain tends to swell, while if it is weaker (poor solvent), the chain tends to contract. The Flory theory [54] for good solvent is based on equating the attractive and repulsive forces, yielding the Flory radius R_F (mean-square end-to-end distance) of

²³ A polymer solution is a mixture of polymer and solvent.

$$R_F \approx a \left(\frac{v}{a^3} \right)^{2\nu-1} \cdot N^\nu \approx a \left(\frac{v}{a^3} \right)^{1/5} N^{3/5}, \quad (\text{A.7})$$

where v is called the excluded volume parameter and ν the Flory exponent.

If the attraction forces of monomer-monomer and monomer-solvent balance, leaving just the repulsive forces, the solvent is termed athermal solvent, $v/a^3 \approx 1$, and the chain is a self-avoiding random walk (SAW)²⁴ with radius

$$R_F \approx aN^\nu \approx aN^{3/5}, \quad \text{and} \quad R_g \approx \frac{a}{\sqrt{6}} N^\nu. \quad (\text{A.8})$$

Using the same example as before, for a polystyrene chain of $n = 40,000$ C-C bonds, with $C_\infty = 9.5$, $l = 1.54 \text{ \AA}$, and $\theta = 68^\circ$ [34], we obtain: $R_F = 210 \text{ nm}$, compared to $R_0 = 94.7 \text{ nm}$, a considerable swelling.

The statistical distribution $P(r, N)$ of end-to-end distances r of a long linear real chain is given by [34]:

$$\begin{aligned} P(r, N) &\sim \left(\frac{r}{R_F} \right)^g \exp \left[-\alpha \left(\frac{r}{R_F} \right)^\delta \right] \\ &\cong 0.278 \left(\frac{r}{R_F} \right)^{0.28} \exp \left[-1.206 \left(\frac{r}{R_F} \right)^{2.43} \right] \quad \text{where} \quad R_F \approx aN^{3/5}, \end{aligned} \quad (\text{A.9})$$

and is compared (Figure A-5) to the Gaussian distribution of an ideal chain from Equation (A.5). There is a distinct difference between the distributions – while in ideal chains the most probable end-to-end distance is zero, in real chains it is seldom zero because of swelling.

²⁴ A self-avoiding random walk (SAW) is a random walk on a lattice, which never visits the same site more than once.

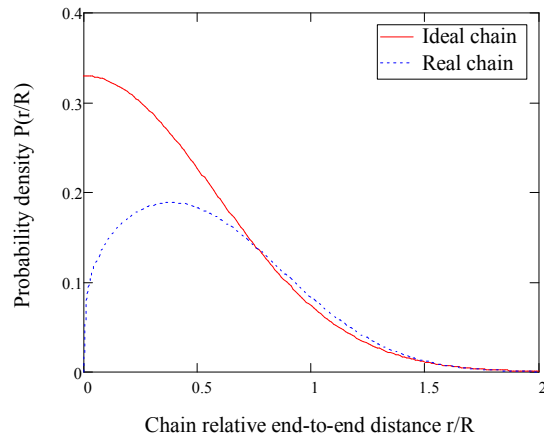


Figure A-5: Distribution of three-dimensional relative end-to-end distances r/R_o and r/R_F of ideal and real long chains respectively.

The R_g Equations (A.4) and (A.8) for ideal and real chains were validated by various scattering experiments (light, small-angle X-ray, and neutron), such as Kirste et al.'s small-angle neutron scattering measurement of ideal chains in a melt of predeuterated PMMA [55], and Flory's light scattering measurement of real chains in a dilute solution [36].

Equations (A.2) and (A.8) provide a good example of a **scaling law**, where the exponent ν is a universal parameter that depends only on the type of polymer solution, and is the same for all coils. The parameter ν varies between $1/3$ (poor solvent) and $3/5$ (good solvent), and equals $1/2$ (θ -solvent) for an ideal chain. The constant pre-factor of these equations is not universal, and depends on the detailed structure of the solution.

Notations

\sim	proportional
\approx	approximate value
\cong	approximate up to a constant
A	chain estimated cross-section [m^2]
a	size of a monomer or chain element [m]
$a, a(X)$	isotropic velocity gradient parameter versus the global position X [m^{-1}] or [step^{-1}] – proportional to the linear (isotropic) velocity gradient s_l
Δa	increase in gradient parameter a when moving to the next subchain [m^{-1}]
a_c	critical isotropic velocity gradient that causes coil-stretch transition [m^{-1}] or [step^{-1}]
b	anisotropic velocity gradient parameter [m^{-1}] or [step^{-1}]
CR	transversal (radial) contraction ratio [dimensionless]
C_∞	Flory's characteristic ratio for long chains [dimensionless]
c	mass concentration of a polymer solution [kg/m^3]
c^*	crossover mass concentration of a polymer solution [kg/m^3]
D	size of the ordered region in a nanofiber [m]
D_s	solvent diffusion coefficient (through the fiber skin) [m^2/s]
D_w	skin thickness of a core-shell nanofiber [m]
d	nanofiber diameter [m]
E	Young's modulus (tensile elastic modulus) [Pa]
E_0	bulk material Young's modulus [Pa]
ΔE	delta tensile modulus ($E - E_0$) [Pa]
ΔE	energy barrier between trans and gauche states [J]
F	Helmholtz free energy [J]
f	extension force [N]
$f_{hyd}(x)$	hydrodynamic force applied on a chain at local position x in direction x [N]
$f_{hyd}(r)$	hydrodynamic force applied on a chain at position r in direction r [N]
f_{h_n}	hydrodynamic force acting on monomer n [N]
f_N	normalized extensional force in a Langevin function [dimensionless]
f_{n+1}	force exerted by monomer $n+1$ on monomer n [N] (excluding the elastic entropic forces)
$f(x)$	end-to-end chain lengths distribution [dimensionless]
G	shear modulus [Pa]
G_0	bulk material shear modulus [Pa]
ΔG	delta shear modulus ($G - G_0$) [Pa]
G_{ibbs}	Gibbs free energy [J]
$G(x)$	Gaussian distribution of variable x [dimensionless]
I_E	electrical current carried by the jet [A]
I	number of runs in a random walk simulation [dimensionless]
i	run order number in a random walk simulation [dimensionless]
J	number of subchains in a random walk simulation [dimensionless]

j	subchain order number in a random walk simulation [dimensionless]
j_{trans}	first subchain to experience coil-stretch transition [dimensionless]
K_a	gradient constant [m^{-2}]
$K_{a-accel}$	accelerated gradient constant $\sim 10^4 \cdot K_a$ [m^{-2}]
k	constant geometry factor of the flow [dimensionless]
k_B	Boltzmann constant [= $1.38 \cdot 10^{-23}$ J/K]
k_l	tensile force constant of a covalent bond [N/m]
k_θ	angular force constant of a covalent bond [N·m/rad]
L	mean-square value of a chain end-to-end distance in a velocity gradient (length) [m]
L_0	mean-square value of chain end-to-end length at zero velocity gradient [m]
ΔL	deviation of chain end-to-end length from the zero gradient mean-square value ($L - L_0$) [m]
L_f	fiber length [m]
ΔL_f	change in fiber length due to surface tension [m]
L_s	length of an extended chain segment [m]
δL_s	longitudinal deflection of an extended chain segment [m]
L_{cor}	correlation length within the amorphous polymer portion [m]
L_{cryst}	Crystallite thickness [m]
l	covalent bond length [m]
l_k	Kuhn segment length (or Kuhn length) [m]
l_p	persistence length [m]
$M1(x)$	first statistical moment (mean) of variable x [x]
$Mn(x)$	central statistical moment n of variable x [x^n]
M_{sc}	molecular mass of a subchain [kg/mol]
Mw	average molecular mass (weight) of a polymer chain [kg/mol]
m	exponent [dimensionless]
N	number of monomers or chain elements in a polymer chain (degree of polymerization of a linear chain) [dimensionless]
N_k	number of Kuhn segments in a chain [dimensionless]
$Nm(x)$	monomers mass density distribution [dimensionless]
Nm	mean-square value of monomers mass density [dimensionless]
Nm_0	mean-square value of monomers mass density at zero velocity gradient [dimensionless]
ΔNm	deviation of monomers mass density from the zero-gradient mean-square value ($Nm - Nm_0$) [m]
$Nm2D$	monomers mass density bivariate distribution [dimensionless]
N_s	number of elements (e.g. monomers) in a subchain [dimensionless]
N_{sc}	number of subchains per unit volume [$1/\text{m}^3$]
n	number backbone bonds in a polymer chain [dimensionless]
n	monomer order position in a chain [dimensionless]
n	order of statistical moment [dimensionless]
n_k	number of backbone bonds in a Kuhn segment [dimensionless]

n_m	integration variable - number of monomers or chain elements ranging from 1 to N [dimensionless]
n_S	number of chains in contact with the fiber surface per fiber unit length [dimensionless]
n_V	total number of chains per fiber unit length [dimensionless]
$P, P(\phi)$	number fraction of chains in contact with the fiber surface [dimensionless]
$P(r)$	Gaussian distribution of a three-dimensional chain end-to-end distance r [dimensionless]
$P_{\pm}(n)$	probability to step from position x_n towards $x_{n\pm 1}$ (in a random walk) [dimensionless]
$P_{\vec{q}}$	stepping probability in direction \vec{q} (in a random walk) [dimensionless]
$P_{\pm r}, P_r$	stepping probability in direction $\pm r$ (in a random walk) [dimensionless]
$P_{\pm x}, P_{\pm}(x)$	stepping probability in direction $\pm x$ (in a random walk) [dimensionless]
P_{step}	Function determining the stepping direction (in a random walk) [dimensionless]
$P(\varphi_o)$	probability density function of chain-element orientation angles φ_o [dimensionless]
Q	renormalization / partition functions (various) [dimensionless]
Q_F	jet volumetric flow rate [m^3/s]
\vec{q}	unit direction vector [dimensionless]
R	fiber radius [m]
\vec{R}	end-to-end distance (radius, length) of a polymer chain [m]
R_c	root-mean-square end-to-end distance (radius, length) of a polymer chain [m]
R_0	root-mean-square end-to-end distance (radius, length) of an ideal chain [m]
R_{cap}	internal core radius of a core-shell nanofiber [m]
R_F	root-mean-square end-to-end distance (radius, length) of a real chain [m]
R_g	radius of gyration of a polymer chain [m]
R_{gas}	gas constant [= 8.31 J/mol/K]
R_{max}	fully extended length of a polymer chain [m]
R_r	root-mean-square end-to-end radial distance of a polymer chain [m]
r	chain elongation or three-dimensional end-to-end distance [m]
r	radial position with respect to a jet central axis [m]
r_0	initial jet radius [m]
r_j	jet radius [m]
S	entropy [J/K]
S_f	fiber surface area [m^2]
ΔS_f	change in fiber surface area due to surface tension [m^2]
s	velocity gradient [1/s]
s_1	linear (isotropic) velocity gradient [s^{-1}]
s_2	quadratic (anisotropic) velocity gradient [$\text{m}^{-1}\text{s}^{-1}$]
s_{1c}	critical linear (isotropic) velocity gradient that causes coil-stretch transition [s^{-1}]

s_c	critical velocity gradient [1/s]
T	temperature [K]
T_g	glass transition temperature [K]
T_m	melting temperature [K]
t	time [s]
U	chain internal energy (independent of conformation) [J]
$U, U(r)$	field potential, potential at a three-dimensional location r [J]
U_n	flow field potential at position x_n [J]
U_{st}	surface tension energy density [N/m ²]
U_x	flow field potential derivative in direction x [J/m]
U_r	flow field potential derivative in direction r [J/m]
U_ε	network strain energy per unit volume [J/m ³]
V_0	initial jet velocity [m/s]
V_f	fiber volume [m ³]
ΔV_f	change in fiber volume due to surface tension [m ³]
V_r	jet global radial velocity [m/s]
$V_x, V(X)$	jet global longitudinal velocity with respect to jet exit [m/s]
v	excluded volume parameter [m ³]
$v(x)$	local velocity with respect to chain force center [m/s]
w	subchain stretch constant term [dimensionless]
X	global position along the jet [m]
X_0	initial jet distance from the zero-velocity position [m]
X_c	critical position along the jet where coil-stretch transition occurs [m]
x	local coordinate system with respect to chain force center [m]
x	chain end position with respect to the center between two boundaries [m] or [step]
x_0	chain starting position with respect to the center between two boundaries [m] or [step]
x_n	chain running end position with respect to chain start (in random walk) [m] or [step]
y	chain end position parallel to the boundaries [m] or [step]
y_0	chain starting position parallel to the boundaries [m] or [step]
α_{sat}	velocity gradient saturation parameter [m ²] or [step ²]
α_{slip}	subchain slip parameter [dimensionless]
β	coefficient $1/k_B T$ [1/J]
γ	surface tension [N/m]
Δ	step size in a random walk simulation (equivalent to chain element size a) [m] or [1-step]
δ	bending deflection of a nanofiber [m]
ε	dielectric constant of a polymer solution [dimensionless]
ε	strain or relative elongation r/R_0 [dimensionless]
$\Delta\varepsilon$	energy difference between trans and gauche states [J]
η	jet viscosity [Pa·s]

η_0	zero shear rate viscosity of a polymer solution [Pa·s]
η_s	polymer solution viscosity [Pa·s]
θ	covalent bond tetrahedral angle [rad]
λ	relative elongation [dimensionless]
ν	Flory scaling exponent [dimensionless]
ν	Poisson ratio [dimensionless]
ζ	average mesh size of a polymer network in a semi-dilute solution [m]
ζ_0	initial subchain length (mesh size) [m]
ζ_j	elongation of subchain j in a random walk simulation [m]
$\zeta(X)$	subchain elongation at a global position X [m]
$\zeta_x(X)$	subchain elongation in direction x , at a global position X [m]
$\zeta_r(X,r)$	subchain elongation in direction r , at a global position X , r [m]
ρ	material density [kg/m ³]
ρ	polymer solution density [kg/m ³]
σ	stress or force per unit area [Pa]
τ	single chain relaxation time [s]
τ_e	evaporation time [s]
ϑ	relative free volume between chains [%]
φ	covalent bond torsion (rotation) angle [rad]
φ_o	chain-element orientation angle with respect to the jet axis [rad]
ϕ	volume concentration of a polymer solution [dimensionless]
ϕ^*	crossover (overlap) volume concentration of a solution [dimensionless]
χ	ratio of the initial jet length to the nozzle diameter [dimensionless]
Ψ, Ψ_n	Normalized statistical moments of the relative end-to-end chain distance [dimensionless]
Ω	number of possible coil configurations for a given extension [dimensionless]

References

1. de Gennes, P.G., *Scaling concepts in polymer physics*. 1979, Ithaca, N.Y.: Cornell University Press. 324 p.
2. de gennes, P.G., *Coil-Stretch Transition of Dilute Flexible Polymers under Ultrahigh Velocity-Gradients*. *Journal of Chemical Physics*, 1974. **60**(12): p. 5030-5042.
3. Crowley, D.G., et al., *Localized Flow Birefringence of Polyethylene Oxide Solutions in a 4 Roll Mill*. *Journal of Polymer Science Part B-Polymer Physics*, 1976. **14**(6): p. 1111-1119.
4. Feng, J. and L.G. Leal, *Numerical simulations of the flow of dilute polymer solutions in a four-roll mill*. *Journal of Non-Newtonian Fluid Mechanics*, 1997. **72**(2-3): p. 187-218.
5. Feng, J. and L.G. Leal, *Transient extension and relaxation of a dilute polymer solution in a four-roll mill*. *Journal of Non-Newtonian Fluid Mechanics*, 2000. **90**(1): p. 117-123.
6. Huang, Z.M., et al., *A review on polymer nanofibers by electrospinning and their applications in nanocomposites*. *Composites Science and Technology*, 2003. **63**(15): p. 2223-2253.
7. Taylor, G., *Electrically Driven Jets*. *Proceedings of the Royal Society of London Series a-Mathematical and Physical Sciences*, 1969. **313**(1515): p. 453.
8. Andrady, A.L., *Science and technology of polymer nanofibers*. 2008, Hoboken, N.J.: Wiley. xix, 403 p.
9. Stanger, J., N. Tucker, and M. Staiger, *Electrospinning*, in *Rapra Review Reports*. 2005.
10. Gogotsi, I.U.G., *Nanotubes and nanofibers*. *Advanced materials series*. 2006, Boca Raton, FL: CRC Taylor & Francis. 248 p.
11. Gatford, J., *A diagram of the electrospinning process showing the onset of instability*. 2008, The New Zealand Institute for Plant and Food Research Ltd.
12. Landcuo. *A diagram of electrospinning process for polymer production*. 2006.
13. Demir, M.M., et al., *Electrospinning of polyurethane fibers*. *Polymer*, 2002. **43**(11): p. 3303-3309.
14. Hsu, C.M. and S. Shivkumar, *Nano-sized beads and porous fiber constructs of poly(epsilon-caprolactone) produced by electrospinning*. *Journal of Materials Science*, 2004. **39**(9): p. 3003-3013.
15. Rutledge, G. and S. Fridrikh, 2002.
16. Gupta, P., et al., *Electrospinning of linear homopolymers of poly(methyl methacrylate): exploring relationships between fiber formation, viscosity, molecular weight and concentration in a good solvent*. *Polymer*, 2005. **46**(13): p. 4799-4810.
17. Colby, R.H., et al., *Effects of Concentration and Thermodynamic Interaction on the Viscoelastic Properties of Polymer-Solutions*. *Macromolecules*, 1991. **24**(13): p. 3873-3882.
18. Han, T., A.L. Yarin, and D.H. Reneker, *Viscoelastic electrospun jets: Initial stresses and elongational rheometry*. *Polymer*, 2008. **49**(6): p. 1651-1658.
19. Bellan, L.M., H.G. Craighead, and J.P. Hinstroza, *Direct measurement of fluid velocity in an electrospinning jet using particle image velocimetry*. *Journal of Applied Physics*, 2007. **102**(9).

20. Reneker, D.H., et al., *Bending instability of electrically charged liquid jets of polymer solutions in electrospinning*. Journal of Applied Physics, 2000. **87**(9): p. 4531-4547.
21. Reneker, D.H., et al., *Electrospinning of nanofibers from polymer solutions and melts*. Advances in Applied Mechanics, Vol 41, 2007. **41**: p. 43-195.
22. Reznik, S.N. and E. Zussman, *Stationary uniform and compound viscous jets of leaky dielectrics in a strong electric fields*. 2007, Technion, internal report EM10338.
23. Guenther, A.J., et al., *Dynamics of hollow nanofiber formation during solidification subjected to solvent evaporation*. Macromolecular Theory and Simulations, 2006. **15**(1): p. 87-93.
24. Arinstein, A. and E. Zussman, *Postprocesses in tubular electrospun nanofibers*. Physical Review E, 2007. **76**(5).
25. Arridge, R.G.C., *Mechanics of polymers*. 1975, Oxford [Eng.]: Clarendon Press. ix, 246 p.
26. Nielsen, L.E. and R.F. Landel, *Mechanical properties of polymers and composites*. 2nd ed. Mechanical engineering. 1994, New York: M. Dekker. xiii, 557 p.
27. Ward, I.M. and J. Sweeney, *An introduction to the mechanical properties of solid polymers*. 2nd ed. 2004, Chichester, West Sussex, England: Wiley. x, 382 p.
28. Mallick, P.K., *Fiber-reinforced composites : materials, manufacturing, and design*. 3rd ed. 2008, Boca Raton, FL: CRC Press. xvii, 619 p.
29. Daniel, I.M. and O. Ishai, *Engineering mechanics of composite materials*. 2nd ed. 2006, New York: Oxford University Press. xviii, 411 p.
30. Landau, L.D., et al., *Theory of elasticity*. 3rd English ed. Course of theoretical physics. 1986, Oxford [Oxfordshire] ; New York: Pergamon Press. viii, 187 p.
31. Timoshenko, S. and J.N. Goodier, *Theory of elasticity*. 3d ed. Engineering societies monographs. 1969, New York,: McGraw-Hill. xxiv, 567 p.
32. Gillis, J. *A schematical sketch of a spherulite semi-crystalline region in a linear polymer*. 2007.
33. Arinstein, A., et al., *Effect of supramolecular structure on polymer nanofibre elasticity*. Nature Nanotechnology, 2007. **2**(1): p. 59-62.
34. Rubinstein, M. and R.H. Colby, *Polymer physics*. 2003, Oxford ; New York: Oxford University Press. xi, 440 p.
35. Grosberg, A.I.U. and A.R. Khokhlov, *Statistical physics of macromolecules*. AIP series in polymers and complex materials. 1994, New York: AIP Press. xxvii, 350 p.
36. Flory, P.J., *Statistical mechanics of chain molecules*. 1969, New York,: Interscience Publishers. xix, 432 p.
37. Treloar, L.R.G., *Calculations of elastic moduli of polymer crystals: I. Polyethylene and Nylon 66*. Polymer, 1960. **1**(1): p. 95-103.
38. Rappé, A.K. and C.J. Casewit, *Molecular mechanics across chemistry*. 1997, Sausalito, Calif.: University Science Books. xii, 444 p.
39. Blond, D., et al., *Strong, tough, electrospun polymer-nanotube composite membranes with extremely low density*. Advanced Functional Materials, 2008. **18**(17): p. 2618-2624.
40. Bokobza, L., *Multiwall carbon nanotube elastomeric composites: A review*. Polymer, 2007. **48**(17): p. 4907-4920.
41. Coleman, J.N., et al., *High-performance nanotube-reinforced plastics: Understanding the mechanism of strength increase*. Advanced Functional Materials, 2004. **14**(8): p. 791-798.

42. Jordan, J., et al., *Experimental trends in polymer nanocomposites - a review*. Materials Science and Engineering a-Structural Materials Properties Microstructure and Processing, 2005. **393**(1-2): p. 1-11.
43. Ji, Y., et al., *Confinement-induced super strong PS/MWNT composite nanofibers*. Epl, 2008. **84**(5).
44. Burman, M., A. Arinstein, and E. Zussman, *Free flight of an oscillated string pendulum as a tool for the mechanical characterization of an individual polymer nanofiber*. Applied Physics Letters, 2008. **93**(19).
45. Cuenot, S., S. Demoustier-Champagne, and B. Nysten, *Elastic modulus of polypyrrole nanotubes*. Physical Review Letters, 2000. **85**(8): p. 1690-1693.
46. Cuenot, S., et al., *Surface tension effect on the mechanical properties of nanomaterials measured by atomic force microscopy*. Physical Review B, 2004. **69**(16).
47. Park, H.S., et al., *Mechanics of crystalline nanowires*. Mrs Bulletin, 2009. **34**(4): p. 232-232.
48. de Gennes, P.G., *Glass transitions in thin polymer films*. European Physical Journal E, 2000. **2**(3): p. 201-203.
49. Dingreville, R., J.M. Qu, and M. Cherkaoui, *Surface free energy and its effect on the elastic behavior of nano-sized particles, wires and films*. Journal of the Mechanics and Physics of Solids, 2005. **53**(8): p. 1827-1854.
50. Sharma, P., S. Ganti, and N. Bhate, *Effect of surfaces on the size-dependent elastic state of nano-inhomogeneities*. Applied Physics Letters, 2003. **82**(4): p. 535-537.
51. Gersappe, D., *Discussion at the Technion*. 2009.
52. Feynman, R.P., *Statistical mechanics; a set of lectures*. Frontiers in physics. 1972, Reading, Mass.: W. A. Benjamin. xii, 354 p.
53. Askeland, D.R. and P.P. Phulé, *The science and engineering of materials*. 5th ed. 2006, Toronto, Ont.: Thomson. xx, 863 p.
54. Flory, P.J., *Polymer Chemistry*. Abstracts of Papers of the American Chemical Society, 1983. **186**(Aug): p. 4-Acsc.
55. Kirste, R.G., W.A. Kruse, and K. Ibel, *Determination of Conformation of Polymers in Amorphous Solid-State and in Concentrated Solution by Neutron-Diffraction*. Polymer, 1975. **16**(2): p. 120-124.